Accessibility to Nanocapsule Loadings

Dissertation
zur Erlangung des Grades
Doktor der Naturwissenschaften
im Promotionsfach Chemie

am Fachbereich Chemie, Pharmazie und Geowissenschaften
der Johannes Gutenberg-Universität Mainz

Isabel Schlegel

geboren in Nürnberg
Mainz, 2017

1. Gutachterin:

2. Gutachter:

Tag der mündlichen Prüfung: 03.11.2017

Die vorliegende Arbeit wurde am Max-Planck-Institut für Polymerforschung in Mainz unter der Betreuung von .... von Mai 2014 bis September 2017 angefertigt.

Ich versichere, die vorliegende Arbeit selbstständig angefertigt zu haben. Alle verwendeten Hilfsmittel und Quellen habe ich eindeutig als solche kenntlich gemacht.

„Die Neugier

steht immer an erster Stelle eines Problems,

das gelöst werden will"

Galileo Galilei

Table of Contents

1. Introduction

Cancer is a worldwide leading cause of death.[1] Research is now focusing on improving cancer diagnosis and treatments. As a result, the number of cancer survivors slowly increases due to advances in early detection and treatment.[2] Most diagnostic techniques require contrast agents. Contrast agents for clinical imaging such as magnetic resonance imaging (MRI) or computed tomography (CT) still suffer from drawbacks such as high osmotic pressure and high viscosity of the contrast agent infusion solutions, which cause pain in the veins of the patients. The time window for the imaging process is limited because most contrast agents are excreted through the kidneys within minutes.[3-5] A distribution of the contrast agent over the whole body yields an unnecessary exposure of the rest of the body that is not in the focus of interest. Additionally, the contrast agent is diluted over the whole body resulting in a lower contrast enhancing effect that has to be counterbalanced by applying higher amounts of contrast agents.

Nanomedicine is a promising area in cancer research as it offers benefits that are not otherwise available. By entrapment into nanocarriers, a cargo, for instance a drug, is shielded from its environment. This feature allows for the transport of sensitive molecules such as siRNA.[6] The toxicity of harmful substances is reduced because the nanocarriers matrix is shielding entrapped drugs from the environment. Molecules with poor water solubility are available for biomedical applications in form of nanoparticles dispersed in water. Selective drug transport using passive or active targeting further reduces the dose of drug needed for a sufficient therapy. Osmotic pressure and viscosity are reduced as several molecules are bundled into one nanocarrier.[7] Circulation times can be enhanced by the use of stealth materials,[8] extending the time window for the imaging process. The efficacy of MRI contrast agents can be boosted by their encapsulation into nanocapsules.[9] The non-invasive detection of clinically occult metastases was possible with iron oxide-based nanoparticles *via* MRI.[10]

The miniemulsion process is a well-known method for the synthesis of nanocarriers. Droplets in the nanometer range are obtained by high energy input such as sonication or high pressure homogenization. The droplets act as independent reaction vessels. Hydrophobic or hydrophilic compounds can be entrapped into nanoparticles or nanocapsules dispersed in water. Whereas for hydrophobic compounds the direct miniemulsion is a suitable synthesis route, hydrophilic compounds require a two-step route. The synthesis is carried out in a water-in-oil dispersion. After the synthesis, the nanoparticles can be transferred into water, making the nanocarriers suitable for biomedical applications.

Upon higher loadings, leakage is limiting the encapsulation capacity of nanocapsules. The local contrast agent concentration and hence, the contrast enhancing effect are restricted by leakage from the nanocarriers. To enable a higher loading capacity of nanocapsules, the issue of leakage has to be addressed. One possibility to reduce diffusion is the incorporation of crystalline domains into the nanocapsules shell. Crystalline domains act as obstacles and elongate therefore the diffusion pathway. Nanocapsules are synthesized using a semi-crystalline polymer. The shell of the nanocapsules is creating a confinement for the crystallization process. Moreover, crystallization in confinement is known to differ from bulk. The degree of crystallinity can be varied by the shell thickness and by the choice of monomers. The impact of the degree of crystallinity on the diffusion is monitored.

Gadobutrol is a commercial MRI contrast agent. In a previous work it was observed that encapsulation into nanocapsules can boost the efficacy of MRI contrast agents.[9] The encapsulation was so far limited because leakage occurred due to osmotic pressure. The use of a semi-crystalline shell enables the encapsulation of higher amounts of contrast agent by maintaining a sufficient water exchange crucial for MRI contrast agents.

CT requires even higher amounts of contrast agents than MRI.[11] Aiming at higher loadings, nanoparticles are presented here as CT contrast agents.

It is suitable to combine diagnostic and therapy. If the medical imaging is revealing the need for a treatment, it is of interest that nanocarriers target the area of interest. To enable controlled release at the target site, a protein is included as trigger.

The thesis is subdivided as follows. After this introductory chapter, the theoretical background of this thesis is presented in Chapter 2. Short introductions about the most important techniques relevant for this thesis are given in Chapter 3. Chapter 4 is subdivided into four sections according to the above mentioned topics. Each section in Chapter 4 is summarized by an abstract at their beginning, followed by an introduction, which is giving a short overview over the state of the art of the respective topic and highlighting the motivation for the project, by the materials and methods part, and by the results and discussion part.

2. Theoretical Background

First of all, the terms "nanoparticles" and "nanocapsules" are defined in Section 2.1. As diffusion is of major importance for the encapsulation of a cargo into nanocarriers, diffusion and the role of the crystallinity of the matrix are explained. Section 2.3 deals with crystallization in confinement, as it is the case for crystallization in nanocapsules. Semi-crystalline nanocapsules are shown to be suitable for encapsulation of magnetic resonance imaging (MRI) contrast agents. Thus, the underlying physics of MRI and MRI contrast agents are introduced in Section 2.4. Furthermore, nanoscale contrast agents for computed tomography (CT) are presented in this thesis. In Section 2.5, the basic principles of computed tomography are presented. Since triggered release is an important aspect of drug delivery, different stimuli and release mechanisms are presented in Section 2.6. In Chapter 4 the state of the art for each topic is given in the respective introductory section.

2.1. Nanoparticles and Nanocapsules

IUPAC (International Union of Pure and Applied Chemistry) is defining nanoparticles as particles of any shape in the nanometer size range. A nanocapsule is defined by IUPAC as a "hollow nanoparticle composed of a solid shell that surrounds a core-forming space available to entrap substances."[12] Thus, the term "nanoparticle" includes nanoparticles with a solid core as well as nanocapsules. If the term "nanoparticle" is used in contrast to nanocapsules, it is often referring to solid particles consisting of one single phase (Figure 1).

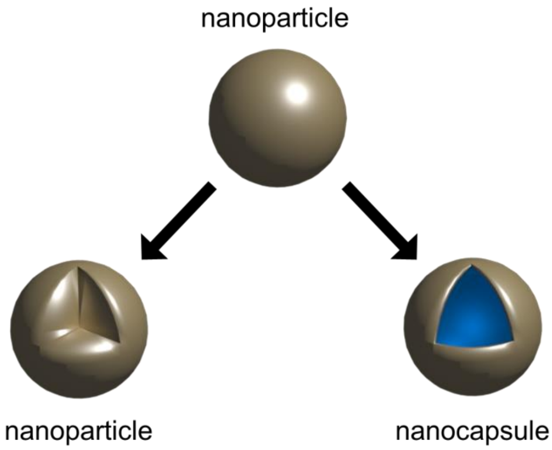

Figure 1: Nomenclature of nanoparticles and nanocapsules. The term "nanoparticle" summarizes all kinds of solid particles in the nanometer size range. Depending on the context, the term "nanoparticle" can also refer to solid core nanoparticles consisting of one phase in contrast to nanocapsules that are exhibiting a core-shell structure.

In this thesis, polymeric nanoparticles with a solid core and nanocapsules with a liquid core are presented. The synthesis was performed *via* the miniemulsion process that will be introduced in Section 4.1.4.1. The miniemulsion process is a novel method to encapsulate a cargo into nanoparticles. For the encapsulation of a cargo into nanoparticles, the permeability of the nanoparticle matrix for the encapsulated cargo and the resulting diffusion processes play a major role.

2.2. Permeability and Diffusion

Permeability through polymer films is a very important property in some applications such as food packaging[13] or membrane filtration.[14] Permeability can be described as the product of sorption and diffusion (eq. 1):[15]

$$P = D \cdot S \qquad (1)$$

Pappenheimer *et al.* were the first to report the pore theory to describe exchange mechanism by diffusion in biological membranes.[14] Renkin extended the work of Pappenheimer *et al.* from biological to artificial membranes and verified the validity of prediction of diffusion calculations.[16]

The nature of the permeant is crucial to predict diffusion. The aggregation state (gas, liquid, solid), the size, the polarity, the osmotic pressure (which is depending on the local concentration of the permeant), and the partition coefficient of the permeant play a key role in the diffusion process.

The matrix is also important in the diffusion process. Indeed, the nature of the matrix, the thickness (the length of the diffusion pathway),[9] and the solubility of the permeant in the matrix influence the diffusion. The crystallinity of the matrix also influences the diffusion for two reasons. Firstly, the sorption of the permeant to the matrix is proportional to the amorphous, *i.e.* non-crystalline part of the material. Secondly, the crystalline domains are impermeable obstacles. Therefore, diffusion takes place through amorphous parts around the crystalline domains, resulting in an elongated diffusion pathway (Figure 2).[13]

Figure 2: Crystalline domains (green) act as impermeable obstacles. Thus, the diffusion of a permeant (orange) has to go around the crystalline domains through the amorphous parts, resulting in a longer diffusion pathway.

In thin membranes, diffusion might take place very fast due to the short diffusion pathway. A major drawback of nanocapsules in comparison with microcapsules is the thinner shell, which can result in leakage of encapsulated payloads. One way to reduce diffusion is to use a semi-crystalline material as the shell in nanocapsules.[17-19]

In polymeric nanocapsules, the crystallites in the shell experience a strong confinement. Crystallization in confinement is known to differ strongly from crystallization in bulk. Chapter 2.3 will focus on the confinement effect on the crystallization behavior.

2.3. Crystallization in Confinement

Whereas in bulk heterogeneous nucleation is the preferred nucleation mechanism, in confinement homogeneous nucleation can take place. The absence of heterogeneous nucleation is observed as a decrease in the crystallization temperature.[20]

There are different reported approaches to isolate samples in small volumes to observe the effect of confinement. The most popular phenomenon, which can be observed in nature, is the crystallization of water droplets in clouds. The crystallization temperature of water in clouds is decreased from 0 °C to near -40 °C.[21,22] Molecular dynamic simulations of Johnston *et al.* show that the melting temperature in small water droplets is decreasing with decreasing water droplet size from 4.7 to 1 nm radius.[23]

Another method is the entrapment of a crystallizable material in pores[24] or encapsulation in micro- or nanocapsules.[25] In polymeric nanocapsules with a semi-crystalline shell, crystallites can only grow inside a thin nanocapsules shell that is sandwiched between the inner and the outer liquid phase. The growth of the crystallites is limited by the thickness of the nanocapsules shell as well as by the curvature of the nanocapsule (Figure 3).

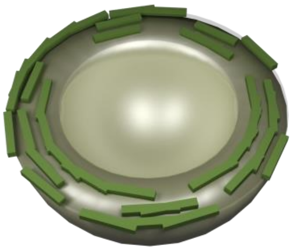

Figure 3: Scheme of possible distribution of crystalline domains (green) in a semi-crystalline nanocapsules shell.

Schneider *et al.* calculated the energy of crystalline domains of different shapes on a spherical surface such as colloidal crystals on emulsion droplets and studied the impact of curvature on the shape of crystalline domains using continuum elasticity theory and simulations. They suggest that defects in the crystalline domains allow for curved shapes to fit the curved surface.[26]

In this thesis, the focus is on the crystallization of a semi-crystalline polymer in the nanocapsule shell. In Chapter 4.1, more detailed information on the crystallization behavior of semi-crystalline polymers in confinements such as nanocapsule shells will be given.

2.4. MRI Contrast Agents and Possibilities to Increase Relaxivity

In this thesis, nanocontainers with the ability to increase the efficacy of a commercial MRI contrast agent will be presented. To understand the factors defining the resulting contrast of an MRI, the basic principles of MRI will be explained.

2.4.1. Basic Principles of NMR, MRI, and Relaxation Times

In a magnetic field, nuclear energy levels split up due to Zeeman splitting and the nuclear spins align parallel to the magnetic field, resulting in a nuclear magnetization (Figure 4).[27] In terms of classical physics, this nuclear magnetization is rotating at the Larmor frequency around the direction of the magnetic field (z-axis) due to its angular momentum and its magnetic moment. In 1946, Edwards Mills Purcell was the first to demonstrate the absorption of a radio frequency (RF) pulse at the Larmor frequency by the nuclear spin system, leading to an excitation of the spin system to a higher energy level.[28] In the same year, Felix Bloch observed the spontaneous emission of RF after excitation.[29] These observations were the beginning of nuclear magnetic resonance (NMR) spectroscopy and were awarded with a Nobel Prize in 1952. [30]

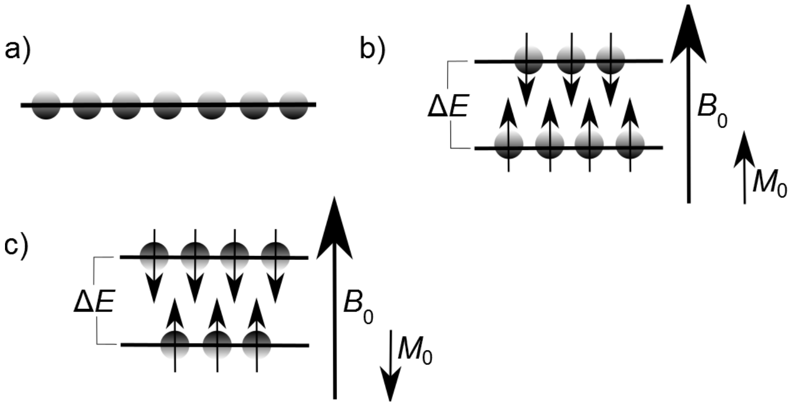

Figure 4: The nuclear spin system: a) Without magnetic field B_0, all spins have a random orientation. b) In a magnetic field, the energy levels split up and the spins are aligning parallel to the magnetic field. The difference between the energy levels is ΔE. A nuclear magnetization M_0 is observable. c) The nuclear spin system after excitation by absorption of an RF pulse. The resulting nuclear magnetization is now antiparallel to the magnetic field.

To be absorbed, the applied RF pulse has to fit the difference between the energy levels ΔE, which can be calculated from the Larmor frequency v and the Planck's constant h (eq. 2):

$$\Delta E = hv \tag{2}$$

The term 'magnetic resonance' (MR) is referring to the absorption process of the resonant RF pulse. To detect an NMR signal, the nuclear magnetization is turned by 90°, inducing a signal in a nearby coil due to its precession.

The transition from the excited state into the ground state is described by two processes: the longitudinal and the transversal relaxation. The longitudinal relaxation process is affecting the total energy of the spin system. The transversal relaxation is describing the loss of the polarization transversal to the applied magnetic field. To characterize the relaxation processes, Bloch introduced the relaxation times T_1 and T_2.[31] Magnetic resonance imaging (MRI) is mapping the distribution of the different relaxation times. In soft tissue, different water mobilities and therefore different T_1 and T_2 times of the water proton nuclei are present. In a T_1 time weighted MRI tissue with a high water mobility is appearing dark as it exhibits a long T_1 time (*e.g.,* cerebrospinal fluid in the brain T_1 = 3 s at 1.5 T). In tissue where the diffusion of water molecules is restricted, the T_1 time is shorter (*e.g.,* for gray matter in the brain, T_1 = 921 ms at 1.5 T) and the tissue is appearing brighter.[32]

MRI contrast agents are used to enhance the contrast in MRI images. The magnetic moment of a paramagnetic compound interacts with the magnetization of the hydrogen nuclei, allowing a faster relaxation process and shorting therefore the T_1 time. The most paramagnetic and stable metal ion is Gd^{3+} with seven unpaired electrons, exhibiting a large magnetic moment and a long electron spin relaxation time. As free Gd^{3+} is highly toxic (intravenous LD_{50} in mice: 0.2 mmol kg^{-1}),[33] stable chelates of gadolinium are used as MRI contrast agents. By applying a paramagnetic contrast agent, the tissue appears brighter than before.[34]

2.4.2. General Factors Affecting Relaxivity

Relaxivity is giving the efficiency of MRI contrast agents to enhance the contrast by shortening the relaxation time.[34] By increasing the efficiency of contrast agents, their doses and the side effects for the patients can be reduced. Thus, understanding how contrast agents are influencing the relaxation time of water is crucial for engineering more efficient contrast agents.

The relaxation of aqueous protons in the presence of paramagnetic ions is dominated by the interaction between electronic spins of the paramagnetic ions and the nuclear spins of the water protons. In 1946, Bloch, Hansen, and Packard were the first to report the influence of paramagnetic ions on the proton relaxation time.[29] In 1948, Bloembergen, Purcell, and Pound screened different paramagnetic ions for their impact on the water proton relaxation times T_1 and T_2.[35] Solomon reported in 1955 the proton–electron spin dipole-dipole interaction[36] and Bloembergen *et al.* showed in 1957 and 1961 the isotropic proton electron spin exchange.[37,38] The ion tumbling time, which can be controlled by the temperature, is influencing the interaction between protons and electrons.[39]

Gd^{3+}chelates are able to bind water molecules in their coordination sphere, which are chemically exchanged with water molecules from the surrounding bulk water. The surrounding water protons, which are not directly bond to the metal ion, are also experiencing the paramagnetic effect. Thus, the interactions between contrast agent and water protons can be described by an inner and an outer sphere contribution.

The relaxivity of current contrast agents is mainly limited by the rotation of the contrast agent molecule and by the water exchange.[34] By slowing down the rotation of the contrast agent (*e.g.,* by increasing its molecular weight), the relaxivity is increased.[40] The water exchange rate is influenced by the choice of the chelating agents.[5] The diffusion of the surrounding water molecules is also influencing the relaxivity (Figure 5).[41]

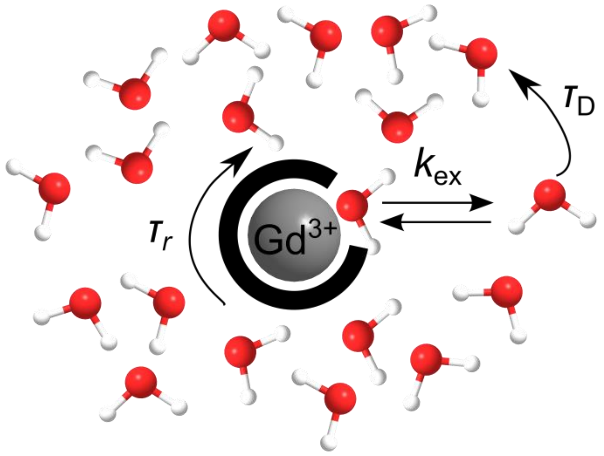

Figure 5: Factors influencing relaxivity: The coordinated water molecule can be exchanged with molecules from the bulk at the exchange rate k_{ex}. The correlation time τ_{r} is describing the rotation of the whole Gd^{3+} complex and τ_{D} the diffusion of the surrounding solvent molecules. The coordination sphere, surrounding the Gd^{3+} ion, is depicted in black.

The mobility of the contrast agent can also be reduced by attachment of the contrast agent molecules to a nanoparticle surface[42] or by confining the space through encapsulation into nanocontainers while maintaining a high exchange of water molecules through the confining matrix.[43,44] By chemically binding or physically entrapping the contrast agent molecules in nanocarriers, the dilution of the contrast agents in blood is prevented. Targeting allows the nanocapsules for accumulating at the respective region of interest which results in high local contrast agent concentrations. Active targeting can be achieved by binding targeting moieties on the nanocapsule surface. Passive targeting is describing the cell uptake by macrophages that recognize any foreign material in the blood stream. Macrophages transport nanoparticles to the liver and the spleen.[45] Furthermore, the osmotic pressure in the blood stream, which correlates with the number of injected molecules, is reduced, as several contrast agent molecules are bundled to form one nanocarrier. This is favorable, as all clinically used gadolinium chelate formulations are hypertonic.[46,47]

Local high contrast agent concentrations are not the only requirements to ensure a high contrast. In combination with targeting moieties on the surface of the nanocarriers, the region of interest can be directly addressed and the amount of needed contrast agent further reduced. A sustainable water exchange is crucial for a high relaxivity. Thus, bundling Gd^{3+} ions into nanoparticles is not automatically yielding high relaxivities. A $NaYF_4$:Tm,Yb shell of 4 nm grafted on $NaYF_4$:Er,Yb,Gd particles is enough to decrease the relaxivity of Gd^{3+} containing nanoparticles to nearly zero.[48,49]

Most nanoparticle systems are reporting high relaxivities but low local Gd concentrations.[44] In Chapter 4.2, we will show how high concentrations and high relaxivities can be combined by the use of nanocapsules with a semi-crystalline polymer.

2.5. Computed Tomography (CT)

In 1895, Röntgen discovered an electromagnetic radiation with a wavelength in the range of 0.01 to 10 nm and called it X-rays.[50] Soon after the discovery of X-rays, the idea came up to use X-ray tomography (Greek: *tomos* = slice, *graphein* = draw) as diagnostic tool in medicine. CT is still one of the most used clinical diagnostic tools, as it is less expensive, less time consuming, and readily available compared to other non-invasive imaging techniques.[7]

Although MRI is not using ionizing radiation and requires fewer amounts of contrast agents, it is not a suitable method for every patient. Metal-based foreign matter (*e.g.,* implants, bullets or shrapnel) can cause severe damage to the patient when brought into a strong magnetic field as it is required for MRI.[51] Even non-ferromagnetic metal-based implants, which are considered as MRI-safe, can cause artifacts during the MRI process.[52] Thus, CT is an important alternative imaging technique to MRI.

In clinical CT scanners, X-rays are generated when electrons are accelerated from a cathode to colloid with a metal anode at high voltage (80–150 kVp (kVp = peak kilovoltage)) in a vacuum tube. CT scanners image the absorption of X-rays. The absorption is more effective when the density or the atomic number of a material is high. Thus, bones are absorbing X-rays better than soft tissue. The absorption of X-rays further increases when the radiation is matching the ionization energy of the material and an electron of the *k*-edge of an atom is released. X-rays belong hence to the ionizing radiation.[3,53]

For visualization of soft tissue by CT, contrast agents are needed. Suitable CT contrast agents are atoms with a high atomic number, as iodine, barium or gold. Additionally, the X-ray energy can be adjusted to match the ionization energy of the applied contrast agent to increase further the absorption. To reach an effective contrast enhancement, high doses (mM concentrations) of contrast agent are required, which is an immense disadvantage of CT in comparison with other non-invasive imaging techniques such as MRI (µM), positron emission tomography (PET) (µM) or optical imaging (nM).[7,11]

High doses of contrast agent are unfavourable especially in terms of osmotic pressure, viscosity, and toxicity. Consequently, the reduction of the required dose of CT contrast agents is an ongoing task.[7]

2.6. Triggered Release

The transport of a drug is considered successful if the drug is set free once the target of interest is reached. Triggered release is a very important topic regarding drug transport. Beside the degradation of the whole nanocarrier, release can be realized through pores generated by the degradation of predetermined breaking points in the nanocarriers' matrix. Mesoporous silica nanoparticles are presented as a model system for the later. Entrapment is achieved by capping the pores, which have a diameter of a few nanometers. Release is achieved by removing the caps. In literature, a broad variety of stimuli-responsive gating systems is reported.[54] The stimuli can be a change of pH value, redox state, or temperature, photoirradiation or enzymatic degradation.

Although this thesis is not dealing with mesoporous silica nanoparticles (MSN), the release mechanisms presented in this chapter can be transferred to polymeric nanocapsules.

2.6.1. pH-Responsive Release

Different structures can be triggered by a change of the pH value. Polyelectrolytes are charged polymers with extended conformation due to ionic repulsion. By changing the pH value, the charges can vanish, *e.g.,* by protonation of carboxylic acid, and therefore, the electrostatic repulsion disappears. The gates consisting of polyelectrolytes can open and the cargo is released.[55,56] The ion–dipole interaction between bisammonium stalks grafted in MSN surface and cucurbit[6]uril, serving as a supramolecular cap works in a similar way. At pH 10, the bisammonium groups become deprotonated and the cap is released together with the cargo.[57] Park *et al.* presented a polypseudorotaxane-based gating system, which releases the cargo upon protonation of a poly(ethylene-imine) at pH 5.5.[58]

Another approach is the use of materials that become soluble at a certain pH, *e.g.,* ZnO, which is stable at pH 7.4 but rapidly dissolves at pH < 5.5.[59] Acid-labile linkers, such as esters,[60] acetal groups,[61,62] or boronate esters,[63] are reported as gating systems. At acidic pH, the chemical bonds break up and the gates open.

2.6.2. Temperature-Responsive Release

By increasing the temperature, chemical bonds such as in azogroups,[64] peroxides,[65] or loosely arranged complexes[66] can decompose. Another phenomenon observed under heating of a material is melting, *e.g.,* of paraffin caps.[67] Some polymers exhibit a lower critical solution temperature (LCST) and become soluble under heating, releasing their embedded cargo.[68]

For applications in the body, the temperature for the trigger should be in the physiological range. When higher temperatures are required, only part of some tissue can be heated locally. Thus, the temperature has to be raised locally. A method to induce local heating is the use of magnetic nanocrystals. Magnetic nanocrystals react to magnetic actuation and can heat up their local environment. By targeting or by the use of a magnet, the magnetic nanoparticles can be accumulated in the region of interest (*e.g.,* a tumor).[64,66,68] The photothermal effect of metallic nanoparticles can also be used to generate local heat (*e.g.,* gold nanoparticles are able to absorb laser light and to heat their surrounding medium).[63]

2.6.3. Light-Responsive Release

Photo-irradiation can trigger the switch of *trans* to *cis* conformation in molecules and *vice versa*.[69] As presented in Chapter 2.6.2, the induction of local heating by irradiation of metallic nanoparticles (plasmons) converts irradiation into heat.[63] Mal *et al.* reported photo-responsive coumarin derivatives grafted onto pores. Upon irradiation, a reversible intermolecular dimerization of the coumarin derivatives took place, forming a cyclobutane dimer. Release was achieved by photocleavage of these dimers.[70]

2.6.4. Redox-Responsive Release

Disulfide groups are an often reported example of redox-responsive units. Disulfide bonds can be found in proteins, defining their supramolecular structure. The reduction of disulfide bonds to thiol groups is taking place in the body at many places and a lot of enzymes are able to perform the reduction. [71-73]

Another example are pseudorotaxanes formed of 1,5-dioxynaphthalene derivatives as gateposts and cyclobis(paraquat-p-phenylene), a tetracation, as gate. On reduction of the gate to bisradical dications the gates and the content is released.[74]

2.6.5. Enzyme-Responsive Release

Enzymes are able to disrupt disulfide bonds. Proteins can also be digested by enzymes. In gating systems based on protein caps[75] or whole nanocontainers based on proteins,[76] the release is achieved by enzymatic degradation. As degrading enzyme, trypsin is often presented as model system.[75,76] Other enzymes presented in literature are, for instance, amidase and urease.[77]

In this thesis, proteins are presented as predetermined breaking points. As enzymes are readily available at the region of interest (cell uptake), the release of the cargo should start as soon as the nanocontainers have reached their goal. Thus, no additional action such as irradiation is needed.

3. Characterization Methods

The characterization methods of major importance for this thesis are presented and explained in the following chapter. The experimental details for the characterization methods can be found in Chapter 4.2.

3.1. Inductively-Coupled Plasma Optical Emission Spectrometry (ICP-OES)

Within this thesis, elemental quantification of gadolinium and iodine was performed using ICP-OES. Since its invention in the 1960s, ICP-OES has become an important technique for elemental analysis.[78] In plasma environment the sample is showing characteristic emission, which is used for characterization and quantification of the elements therein.[79] The plasma, an ionized gas at high temperatures (4000–8000 K), is formed out of charged particles (Ar^+ and e^-) that are moving independently in an alternating electromagnetic field, generated by an induction coil connected to a radiofrequency generator.[80] The setup of an ICP-OES is schematically shown in Figure 6.

Due to the high temperatures, most samples become completely atomized in the plasma.[81] Upon collision with charged particles, neutral particles become charged and are excited to emit electromagnetic radiation in discrete lines, which are utilized for elemental identification. The intensity of the emitted light at a certain wavelength is proportional to the concentration with a constant linear relationship over 4–6 orders of magnitude. As some parameters in this function are still unknown, a calibration curve has to be recorded for every element prior to analysis. Matrix effects have also to be considered. Thus, the emission line should not overlap with other emission lines from the matrix and the calibration solutions should be dissolved in the same matrix as the sample.

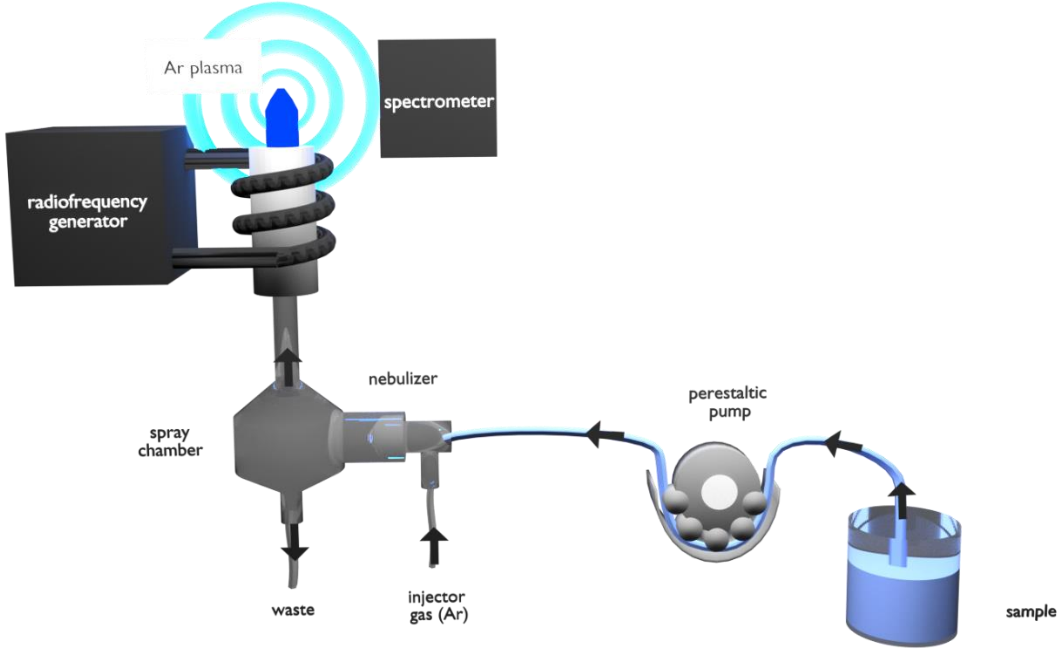

Figure 6: Schematic setup of an ICP-OES: The sample as solution or dispersion is transferred to the nebulizer by a peristaltic pump. The nebulizer forms an aerosol out of the sample and the carrier gas (argon) and sprays it into the spray chamber. Afterwards, the aerosol in introduced into the plasma where it starts to show characteristic emission. The emission is analyzed by a spectrometer. A radiofrequency generator is connected to the induction coil wrapped around the torch to form the plasma *via* electromagnetic induction.

The benefits of ICP are the high sensitivity down to the ppb scale[80] and a broad concentration range. As all atoms and ions are emitting light in the plasma environment, ICP is a multi-element technique, *i.e.* it allows a quick analysis of several elements simultaneously, in contrary to element-orientated techniques like AAS.[82]

3.2. Relaxivity

MRI contrast agents enhance the contrast during MRI measurements by shortening the relaxation times. The relaxivity is the key property of an MRI contrast agent, describing the contrast enhancing effect per contrast agent molecule. The overall relaxation rate R is determined by the relaxivity r, the concentration of contrast agent c as well as the relaxation rate without any contrast agent, which is called diamagnetic contribution R_{dia} (eq. 3):

$$R = r \cdot c + R_{dia} \tag{3}$$

The relaxation rate R is the inverse of the relaxation time T (eq. 4):

$$R = \frac{1}{T} \tag{4}$$

To determine the relaxivity of a contrast agent, the relaxation time is measured for different contrast agent concentrations. The relaxation rate is plotted against the concentration of the contrast agent and the relaxivity is obtained by a linear fit.

The relaxivity of the encapsulated contrast agent has been determined for T_1 and T_2 relaxation times. T_1 is the longitudinal relaxation time, T_2 the spin–spin relaxation time, which has been introduced in Chapter 2.4.

3.2.1. Saturation Recovery

Saturation recovery is a favorable method to measure the transversal relaxation time T_1. To perform saturation recovery measurements, first a 90° RF pulse is applied, turning the magnetization from the z-axis (direction of the magnetic field) to the xy-plane. During the saturation delay τ, the nuclear spins evolve parallel to B_0 and the magnetization increases exponentially. After the time τ, another 90° RF pulse is applied in the same direction as the first pulse to detect the magnetization. For not measuring the RF pulse itself, the data acquisition is starting after a dead time (Figure 7). The measurement is repeated at different saturation delays τ.

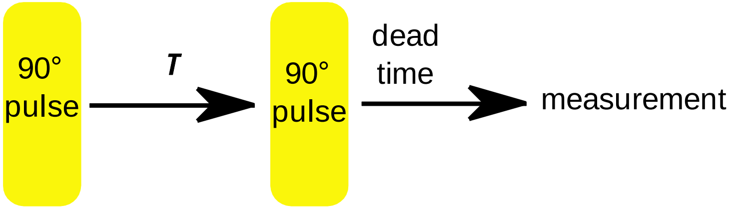

Figure 7: Pulse sequence for saturation recovery measurement. First a 90° pulse is applied, which is disturbing the system. The spins are then allowed to evolve and after a certain time τ, another 90° pulse is applied. Then, after the dead time, the measurement is started.

The relaxation time can be calculated by mono-exponential fitting from the decay curve of the intensity y plotted against the different saturation delays τ (eq. 5):[83]

$$y = y_0 \cdot (1 - e^{-\frac{\tau}{T_1}}) \tag{5}$$

The equal distribution of spins is also called “saturated spins”. Therefore, this method is referred to as “saturation recovery”.

Another method often used for measuring transversal relaxation times is the inversion recovery, which is more accurate. To perform inversion recovery measurements, the expected T_1 time needs to be known prior to the measurement to ensure that the spin system is relaxed before the next measurement starts.[84] As the relaxation time is strongly influenced by several factors such as encapsulation, saturation recovery was chosen to determine T_1 relaxation times. To measure the T_2 relaxation rate, a different pulse sequence is necessary.

3.2.2. CPMG Method

The T_2 relaxation time was measured using the Carr–Purcell–Meiboom–Gill spin echo method (CPMG method). This method is named after its inventors' names.[31]

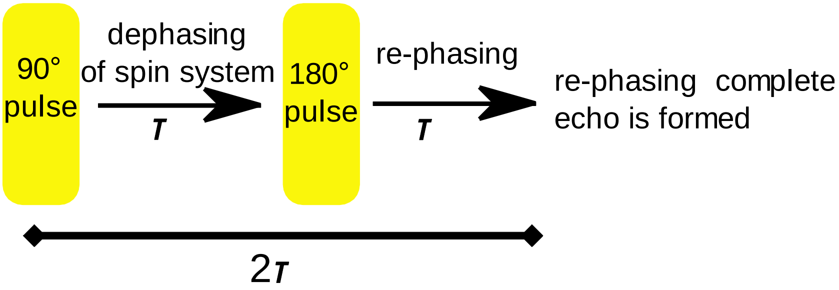

Figure 8: Pulse sequence of CPMG measurement. First a 90° pulse is applied. The spins are then allowed to evolve and after a certain time τ, a 180° pulse is inversing the direction of the spin vectors. During the re-phasing, the spins are moving back to meet after exactly 2τ in total, forming an echo.

First, a 90° excitation pulse is applied. During a waiting time τ the spins evolve. A 180° pulse (shifted by 90° in the xy-plane relative to the 90° pulse) reverses the direction of the evolving vectors. The spin vectors are now moving in the opposite direction and meet exactly after another time τ, causing an echo that is then detected (Figure 8).[85]

The measurement is repeated for N times (for one τ) and for different waiting times τ. The intensity y is plotted against the time τ. A mono-exponential fit gives the T_2 time (eq. 6):[83]

$$y = y_0 \cdot e^{-\frac{\tau}{T_2}} \tag{6}$$

3.3. Dynamic Light Scattering (DLS)

The size of nanoparticles correlates with the shell thickness and therefore with the degree of crystallinity and the permeability, affecting the water exchange and the release profiles. Also, cells interact differently with nanoparticles of different sizes, expressed for instance by different uptake mechanisms.[86] Thus, it is of uttermost importance to know the nanocapsules size distribution.

Dynamic light scattering (DLS) is a powerful technique to determine the average hydrodynamic size and the size distribution of colloids. Therefore, the change in scattering intensity is measured over time at a given scattering angle (Figure 9).[87]

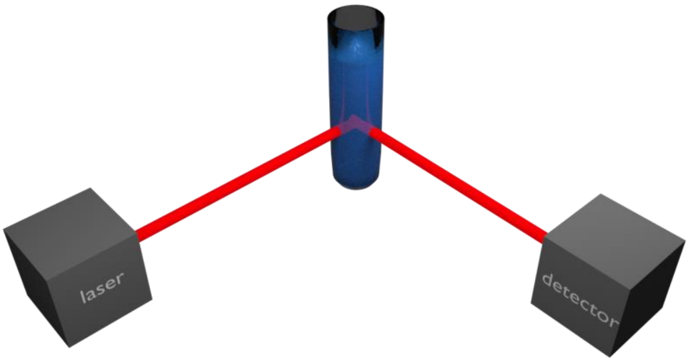

Figure 9: Setup of a dynamic light scattering experiment. The laser beam is irradiating a cuvette containing the sample. The scattered laser light is measured by the detector at a scattering angle of 90°.

Since the scattering particles are moving in solution, the intensity of the scattered light is changing with time and is directly reflecting the Brownian particle motion. This intensity fluctuation can then be converted into a diffusion coefficient of the scattering particle *via* an autocorrelation function. The self-diffusion coefficient D_S of this motion is related to the hydrodynamic radius R_H by the Stokes–Einstein equation (eq. 7):[88]

$$D_s = \frac{k_B T}{6\pi\eta R_h} \tag{7}$$

If the temperature T and the solvent viscosity η are known, the hydrodynamic radius of the scattering particles can be calculated from the self-diffusion coefficient measured by DLS.

DLS is well suited for colloids ranging from 2 nm up to several microns.[89] Smaller particles show a poor scattering intensity, larger particles are too slow in their motion.[90] If the sample is too turbid, multiple scattering might be an issue. Fluorescent samples might disturb the detection of the scattered light.

The average size and the size distribution of the colloids presented in this thesis were characterized by DLS measurements, giving intensity weighted values. Additionally, SEM and TEM were used to obtain a comprehensive particle characterization.

4. Results and Discussion

4.1. Crystallinity Tunes Permeability of Polymer Nanocapsules[1]

In nanocapsules, the thin shell surrounding the liquid core is the only obstacle for diffusion processes. Upon higher loadings, osmotic pressure is promoting leakage from nanocarriers. To enable a higher loading capacity of nanocapsules, and therefore to allow a higher local concentration for a higher contrast the issue of leakage has to be first addressed. By enhancing the barrier properties of the nanocapsules shell, the efficacy of MRI contrast agents can be enhanced.

4.1.1. Abstract

Permeability is the key property of nanocapsules because it dictates the release rate of encapsulated payloads. Herein, we engineer the crystallinity of polymers confined in the shell of nanocapsules. Nanocapsules with crystalline shells are formed from polyurea and polyphosphoester (Figure 10). The thermal properties, such as crystallization temperature and degree of crystallinity, are different from the bulk. The degree of crystallinity is used to control the shell permeability and, therefore, the release of encapsulated payloads, such as fluorescent dyes, typically used as model components for biomedical applications.

---

[1] This section is based on the publication “Schlegel, I.; Muñoz-Espí, R.; Renz, P.; Lieberwirth, I.; Floudas, G.; Suzuki, Y.; Crespy, D.; Landfester, K. Crystallinity Tunes Permeability of Polymer Nanocapsules. *Macromolecules* **2017**, 50, 4725–4732." Reprinted with permission. Copyright 2017 American Chemical Society.

Figure 10: Degree of crystallinity is affected by shell thickness of nanocapsules. By increasing the amount of monomer used during the nanocapsules synthesis, nanocapsules with a higher degree of crystallinity are obtained.

4.1.2. Introduction

Nanocapsules (*i.e.,* core–shell nanoparticles with a liquid core) are of outmost importance in the development of drug-delivery nanocarriers.[91-93] Nanocapsules with an aqueous core are particularly interesting for therapy and diagnostics, as well as for the combination of therapy and diagnostics named theranostics,[94,95] because they allow for the encapsulation of drugs, peptides, proteins,[96-98] enzymes,[99] nucleotides,[100,101] or contrast agents for medical imaging.[102-105] The shell of nanocapsules is playing a key role in such applications because it protects the payload and dictates the permeability and, therefore, the release rate of the payload to the biological environment.[106] In the case of nanocapsules with contrast agents for magnetic resonance imaging (MRI), the shell is even more important because it is also dictating the rate at which water molecules or protons are exchanged between the core and the biological milieu. A previous work demonstrated that precise tuning of the chemistry of the nanocapsules polymer shell could yield a better performance for contrast agents expressed, in this case, by an increase in their relaxivity.[9]

Nanocapsule shells are basically curved nanosheets, sandwiched between a liquid core and the liquid continuous phase, creating a confined environment for polymer chains. It is now well-known that polymer chains in a confined environment exhibit properties that differ from their bulk properties,[107,108] such as enhanced mobility[109] and crystallization kinetics,[110] nucleation mechanism,[111] and crystal orientation.[112] For example, although in the bulk the majority of polymers crystallize *via* a mechanism known as heterogeneous nucleation, poly(ethylene oxide) confined in ~100 nm droplets crystallizes in loosely layered lamellae *via* homogeneous nucleation.[113] In addition, recent studies of polymer crystallization within nanometer size pores demonstrated that by confining polymers to small isolated volumes one can nearly completely suppress heterogeneous nucleation in favor of homogeneous nucleation. In a simple view, this finding implies that heterogeneities are impurities extrinsic to the polymer that are effectively excluded in isolated nanometer size volumes.[20] The degree of crystallinity of different polymers confined in nanoparticles (*e.g.*, poly(L-lactide), syndiotactic or isotactic polystyrene) was found to decrease by decreasing the nanoparticle size.[114] Furthermore, the permeability of polyurea microparticles was also found to depend on the degree of crystallinity of the polymer shell.[115]

The expectation born from these studies is that the physical properties of the polymer shell forming the nanocapsule must be significantly different from the bulk. This is particularly interesting because orientation and arrangement of polymer chains play a key role in the permeability of polymer materials. Torino *et al.* controlled the degree of crystallinity and shell thickness of poly(L-lactide) nanocapsules with sizes lower than 500 nm produced by thermally induced phase separation.[116] These physical properties induced a change in the hydrophilic drug entrapment, corresponding to the encapsulation efficiency, which was, however, below 25%. The authors hypothesized that the reduction in conformational entropy due to confinement induced more interactions between the polymer chains and the nanodroplet surface. The release rate was also found to be dependent on degree of crystallinity and shell thickness, both factors being not decoupled in the experiments proposed by the authors.

On the other hand, the miniemulsion process is a suitable method to fabricate nanocapsules with hydrophilic core and high encapsulation efficiency.[117] It has been notably used for encapsulating contrast agents for magnetic resonance imaging (MRI).[9,118] Wang *et al.* prepared nanosized poly(L-lactic acid) single crystals *via* directed polymer crystallization of nanocapsules shells, the latter prepared by the miniemulsion process.[119] As expected, the degree of crystallinity decreased with nanocapsules size. Furthermore, the mechanical properties of the crystalline nanocapsules, such as the bending modulus, determined by atomic force microscopy (AFM), were found to be advantageous from typical polymersomes.

Here, we aim at controlling the entrapment and permeability of payloads by designing nanocapsules with a semi-crystalline polymer shell. For this study, we selected two families of semi-crystalline polymers, namely polyurea and polyphosphonate. We prepared the nanocapsules by (i) interfacial polyaddition in inverse miniemulsion[117] and (ii) using the miniemulsion-solvent evaporation process already employed with homopolymers,[120] copolymers,[121] and triblock copolymers.[122] Both methods lead to the formation of nanocapsules with a continuous shell, different from other types of nanoobjects derived from micelles and vesicles.

4.1.3. Materials and Methods

Materials

Chemicals were purchased as follows: 1,4-diaminobutane (DAB, 98+%, Thermo Fisher (Kandel) GmbH), 2-methylpropane-1,3-diamine (98+%, ABCR GmbH), sodium dodecyl sulfate (SDS, 99%, Alfa Aesar and Fluka), trimethylsiloxane terminated polydimethylsiloxane (PDMS, M_w = 28,000 g/mol, Alfa Aesar), chloroform (99+%, Thermo Fisher Scientific Inc.), hexamethylene-1,6-diisocyanate (HMDI, ≥99.0%, Sigma Aldrich), cyclohexane (HPLC grade, Sigma Aldrich), tetrahydrofuran (THF, HPLC grade, Sigma Aldrich), Dulbecco's phosphate buffered saline (PBS, no calcium, no magnesium, Thermo Fisher Scientific Inc. and Sigma Aldrich), sulfo-cyanine-5-carboxilic acid (Cy5, Lumiprobe GmbH). The surfactant polyisobutylene-succinimide pentamine was obtained from Lubrizol, France. Phenoxy-polyphosphoester (M_n = 7,500 g/mol, PDI = 2.32) was synthesized by Hisaschi Tee as described in the literature before.[123] All chemicals were used as received. Milli-Q water (18 MΩ cm) was used in all experiments unless otherwise mentioned.

Synthesis of Polyurea Nanocapsules with Different Shell Thicknesses

The shell thickness of the resulting nanocapsules was adjusted by the amount of monomers used during the synthesis. Pre-emulsions were prepared in excess to compensate for washing cycles prior to the homogenization process. A respective amount of diamine (1.5 mmol, 3.0 mmol or 4.5 mmol, 1 equiv) was dissolved in PBS (4.2 g). The solution was added to the continuous phase consisting of cyclohexane (22.5 g) and polyisobutylene-succinimide pentamine (300 mg). The mixture was pre-emulsified using an IKA Ultra-Turrax equipped with a dispersing element S18N-10G for 1 min at 20,000 rpm. The emulsion was injected into a low volume microfluidizer LV1, Microfluidics Corp., equipped with a ceramic interaction chamber F20y-75µ. The emulsification was performed at a pressure of ~1,400 bar under cooling with a water bath at 4 °C. The first stroke was discarded to reduce dilution of the sample. The emulsification process was repeated three times. HMDI (0.75, 1.5 or 3.0 mmol; 1.5 equiv) was diluted in cyclohexane (2.5 g) and added dropwise under stirring (900 rpm) to the emulsion (9.1 g). The monomers were allowed to react for 24 h at room temperature under stirring (900 rpm) in a closed glass vial. The nanocapsule dispersions in cyclohexane were purified by centrifugation at 5000 rpm for 1 h. The supernatant was removed and the nanocapsules were dispersed in THF. Afterward, the centrifugation step was repeated. Nanocapsules were dispersed in cyclohexane and freeze-dried.

Synthesis of Polyurea Nanocapsules Containing Cy5

2-Methylpropane-1,3-diamine (1 mmol) was added to a solution of Cy5 (83 nmol) in PBS (1.4 mL). The aqueous phase was added to the organic phase consisting of cyclohexane (7.5 g) and polyisobutylene-succinimide pentamine (100 mg). The mixture was placed in an ultrasonic bath for 10 min to obtain a pre-emulsion. The pre-emulsion was sonicated under ice-water cooling for 3 min at 90% amplitude with a pulse/pause regime of 20/10 s, using a Branson W450-D sonifier equipped with a 1/2 in. tip. Afterward, HMDI (1.5 mmol) was dissolved in cyclohexane (2.5 g) and added dropwise to the miniemulsion under stirring (900 rpm). The monomers were allowed to react for 24 h under stirring (900 rpm) at room temperature in a closed glass vial.

The nanocapsule dispersion (1 g) was added dropwise to a SDS solution (5 g, 0.3 wt% SDS in water) during sonication in an ultrasonic bath. Afterward, the mixture was stirred at 900 rpm for 24 h at room temperature in a glass vial with an open lid to slowly evaporate the cyclohexane.

Release of Cy5 from the Nanocapsules

The aqueous nanocapsule dispersion was filtrated over Kimwipe tissues to remove agglomerates formed during the transfer from cyclohexane into water. To calculate the loss after filtration, the solid content of the filtrated sample was determined and compared to the theoretical solid content. The aqueous nanocapsule dispersion (4 g) was filled into a dialysis membrane (MWCO 14 kDa, regenerated cellulose, Carl Roth) and dialyzed against water (246 g). At certain time intervals aliquots were withdrawn from the dialysate and the Cy5 concentration was assessed by fluorescence spectroscopy.

Synthesis of PPE Nanocapsules

PhPPE (30 mg) was dissolved in chloroform (2 g) and PDMS (100 mg) was added to the solution. The organic phase was added to SDS solution (5 g, 0.2 wt% SDS in water). The emulsification was performed by sonication as described before (see polyurea nanocapsules containing Cy5). The miniemulsion was stirred overnight at 30 °C with an open lid to slowly evaporate chloroform. Purification of the nanocapsule dispersion was achieved by dialysis for 24 h against demineralized water. Without PDMS, nanoparticles were obtained.

Analytical Tools

The hydrodynamic radius and size distribution of the nanocapsule dispersions were determined by dynamic light scattering (DLS) performed with a PSS Nicomp Particle Sizer 380 at a scattering angle of 90°. For DLS measurements, the nanocapsule dispersions were diluted with cyclohexane or water. Scanning electron microscopy (SEM) images were recorded using a LEO (Zeiss) 1530 Gemini field emission microscope at an extractor voltage of 0.2 kV. Transmission electron microscopy (TEM) images were measured on a JEOL JEM-1400 electron microscope operating at an acceleration voltage of 120 kV. The samples for SEM and TEM were diluted to a solid content of about 0.01 wt% and drop-casted onto a silicon wafer or a carbon-coated copper grid, respectively. The shell thickness was assessed from TEM images and averaged over 100 measurements. The solid content was assessed gravimetrically by weighing 100 µL of sample before and after freeze-drying. Thermogravimetric analysis (TGA) was carried out using a Mettler Toledo ThermoSTAR TGA. The experiments were run in a nitrogen atmosphere heating from 25 to 800 °C with a heating rate of 10 °C /min. Differential scanning calorimetry (DSC) was performed using a Mettler Toledo DSC 3+ calorimeter. The sample was filled in a 100 µL aluminum crucible and subjected to heating, cooling, and again heating cycles in a N_2 atmosphere (30 mL/min) with a rate of 10 °C/min. DSC of the PhPPE nanocapsules was carried out in dispersion to keep the nanocapsules confinement intact after melting. The enthalpy of melting was evaluated as the area under the endothermic signal of the first heating curve. Integration was performed with automatic baseline correction using the software STAR^e 14.00 provided by Mettler Toledo. X-ray diffraction (XRD) measurements were performed by Michael Steiert using a Philips PW 1820 diffractometer with monochromatic Cu Kα radiation ($\lambda = 1.54$ Å) at 30 kV (5 s, $\Delta\theta = 0.02°$). The degree of crystallinity was evaluated as the ratio of the integrated intensity of the crystalline reflections to the total area under the XRD pattern. Prior to integration the XRD patterns were corrected for background scattering. The size of the crystallites L was calculated using the Scherrer equation (eq. 8).

$$L = \frac{K\lambda}{b_{1/2}\cos\theta} \tag{8}$$

where K is a shape factor ($K = 0.9$), λ the wavelength of Cu Kα radiation ($\lambda = 1.54$ Å), $b_{1/2}$ the full width at half maximum of the reflection, and θ the scattering angle.[124]

The concentration of Cy5 was assessed by fluorescence intensity measurements performed with a Tecan Infinite M1000 plate reader. The fluorescence intensity was recorded at an excitation wavelength of $\lambda_{ex} = 646$ nm and an emission wavelength of $\lambda_{em} = 662$ nm, was averaged over 3 measurements and divided by the solid content of the sample.

Dielectric spectroscopy measurements were performed with a Novocontrol Alpha frequency analyzer as a function of temperature by the group of Prof. George Floudas at the University of Ioannina, Greece. Dielectric spectroscopy measurements were recorded at different temperatures in the range from 223 to 433 K in steps of 5 K for frequencies in the range from 10^{-2} to 10^{7} Hz. The nanocapsule dispersion was dried by solvent evaporation prior to dielectric spectroscopy measurements. The complex dielectric permittivity $\varepsilon^* = \varepsilon' - i\varepsilon''$, where ε' is the real and ε'' is the imaginary part, was obtained as a function of frequency ω and temperature T, *i.e.,*

$\varepsilon^*(T,\ \omega)$. The analysis of the T-dependent experiments was made by using the empirical equation of Havriliak and Negami (HN) (eq. 9).

$$\varepsilon^*_{HN}(\omega,T) = \varepsilon_\infty(T) + \frac{\Delta\varepsilon(T)}{\left[1+\left(i\omega\cdot\tau_{HN}(T)\right)^m\right]^n} + \frac{\sigma_0(T)}{i\varepsilon_f\omega} \tag{9}$$

where $\varepsilon_\infty(T)$ is the high-frequency permittivity, $\tau_{HN}(T)$ is the characteristic relaxation time in this equation, $\Delta\varepsilon(T) = \varepsilon_0(T) - \varepsilon_\infty(T)$ is the relaxation strength, m, n (with limits $0 < m, n \leq 1$) describe, respectively, the symmetrical and asymmetrical broadening of the distribution of relaxation times, σ_0 is the dc conductivity, and ε_f is the permittivity of free space. From τ_{HN}, the relaxation time at maximum loss, $\tau_{\max}$, is obtained analytically following eq. 10.

$$\tau_{\max} = \tau_{HN}\cdot\sin^{-1/m}\left(\frac{\pi m}{2(1+n)}\right)\cdot\sin^{1/m}\left(\frac{\pi mn}{2(1+n)}\right) \tag{10}$$

In addition to the measured ε'' spectra, the derivative of ε' ($d\varepsilon'/d\ln\omega \sim -(2/\pi)\varepsilon''$) was used in the analysis of the dynamic behavior. The characteristic time of ion mobility is obtained from the crossing of the real and imaginary parts of ε^* or, equivalently, of the modulus (M^*) representation ($\varepsilon^* = 1\ /\ M^*$).

4.1.4. Results and Discussion

The preparation of nanocapsules is achieved either by inverse or by direct miniemulsion technique. The degree of crystallinity is varied by the shell thickness and by the choice of monomer. The impact of the degree of crystallinity in the nanocapsule shell on the diffusion behavior is investigated using a fluorescent dye as model component. As alternative to *in situ* polymerization, a preformed polymer is used to obtain semicrystalline nanocapsules.

4.1.4.1. Preparation of the Nanocapsules

To tailor encapsulation *and* release behavior of nanocarriers, the nature of nanocapsules shell is of outmost importance. Crystalline domains are known to hinder diffusion because the solubility and diffusion of the molecule that is permeating is hindered in crystalline domains.[115] Therefore, engineering crystalline domains in nanocapsules shells can increase barrier properties. In this work, we have synthesized semi-crystalline nanocapsules with an adjustable degree of crystallinity.

The latter was varied either by controlling the shell thickness at a constant nanocapsules size or by introducing side groups[125] in the chemical structure of the polymer to change the crystallinity. Two types of polymers were studied: an aliphatic polyurea formed *in situ* during the nanocapsules synthesis (Figure 11a) and a pre-synthesized polyphosphoester that was subsequently emulsified (Figure 11b). These nanocapsules have hydrophilic/hydrophobic cores to enable encapsulation of water/oil-soluble substances, respectively.

In inverse miniemulsions, water droplets are dispersed in oil and nanocapsules having a hydrophilic core will form. The aqueous phase containing a diamine is dispersed in a cyclohexane phase containing a surfactant to stabilize the water droplets. Following emulsification, a diisocyanate dissolved in an apolar solvent is added. The polymerization takes place at the droplet surface to form nanocapsules. The reaction takes place very fast, and a polyurea surrounding aqueous droplets is obtained. The droplets and the nanocapsules are stabilized by a surfactant. After polymerization, the polyurea nanocapsules can be transferred into water. Nanocapsules displayed a diameter of 300–500 nm (Table 1).

Table 1: The amount of monomers used during synthesis is listed together with the results from DSL measurements (the hydrodynamic diameter, the size distribution as PDI as well as χ^2).

Monomer amount	d_h (DLS) / nm	PDI	χ^2
0.5x	333	0.16	0.18
	352	0.08	0.37
	407	0.10	1.08
	339	0.10	1.75
1.0x	407	0.14	0.22
	444	0.10	0.33
	346	0.08	3.17
	374	0.07	0.20
1.5x	488	0.27	4.06
	460	0.06	4.47
	408	0.08	0.25
	417	0.09	0.13

Scanning electron microscopy (SEM) micrographs show nanocapsules, which are collapsed upon sample preparation (*i.e.*, drop casting followed by drying) and under the SEM vacuum conditions. Transmission electron microscopy (TEM) micrographs confirm the hollow structure of the nanocapsules (Figure 11a).

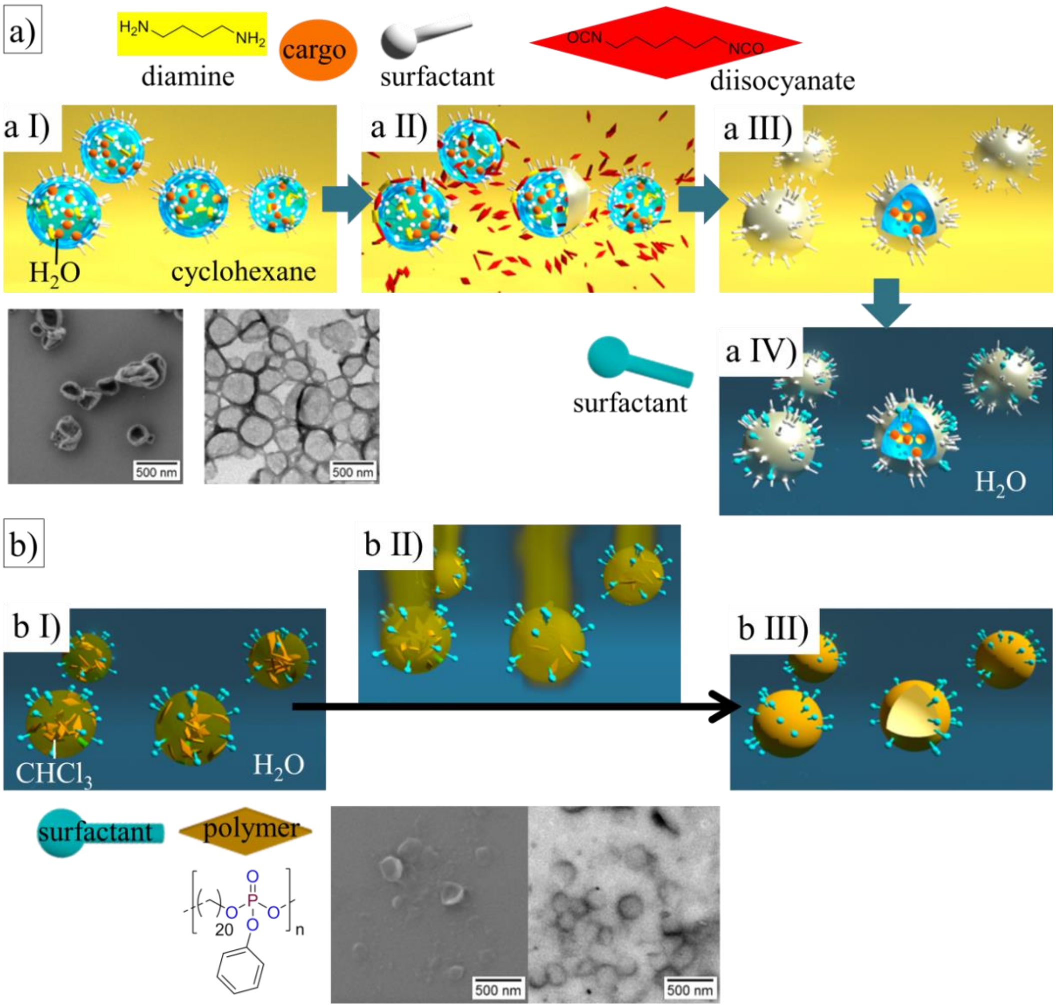

Figure 11: Synthesis of nanocapsules, SEM and TEM images: a) Nanocapsules with an aqueous core in an inverse miniemulsion. The water droplets, formed by emulsification and stabilized by a surfactant, contain a diamine and the cargo (aI). Upon addition of diisocyanate (aII), the polymerization is initialized at the water/oil interface to form a polymer shell surrounding the aqueous core (aIII). Following polymerization, nanocapsules can be transferred into water (aIV). b) Nanocapsules with a hydrophobic core in a direct miniemulsion. The pre-synthesized polymer is dissolved in a chloroform-PDMS mixture and emulsified in water (bI). The hydrophobic droplets are stabilized by a surfactant. Upon evaporation of chloroform (bII) the polymer becomes insoluble and nanocapsules with an oily core are formed (bIII).

By direct miniemulsion (*i.e.*, oil-in-water miniemulsion), nanocapsules with a hydrophobic core are obtained. We selected a polyphosphoester as a nanocapsules shell material because of its semi-crystalline nature[123] and its low melting temperature of about 50 °C, which made DSC measurements in aqueous dispersions possible. The core of nanocapsules was formed by polydimethylsiloxane, a polymer that is initially miscible with the polymer solution, but immiscible with water. For preparing semi-crystalline nanocapsules, the polyphosphoester is dissolved in chloroform, mixed with polydimethylsiloxane and emulsified in water. Upon evaporation of chloroform, an internal phase separation occurs because the polymer is insoluble in the core, yielding oil-filled polyphosphoester nanocapsules dispersed in water with a hydrodynamic diameter of 190 nm and a PDI of 0.11. SEM images show collapsed nanocapsules and TEM images identify core–shell structures (Figure 11b).

4.1.4.2. Crystallinity of Nanocapsules

Nanocapsules based on semi-crystalline polymers are rarely reported.[116,119] The polymeric nanocapsules shell is sandwiched between a liquid core and the liquid continuous phase, generating therefore a confinement for crystal growth. Crystalline lamellae are planar, but inside the nanocapsules shell they can only grow in a curved manner. Hence the growth of the crystalline domains and the overall degree of crystallinity is limited by the nanocapsules shell thickness as well as by the curvature of nanocapsules. In the present case, the shell thickness was adjusted by the total amount of polymer given by the amount of monomers used during the nanocapsules synthesis. This facilitates a comparison under a fixed nanocapsules size (Table 1). The increase in shell thickness is visible in TEM images (Figure 12).

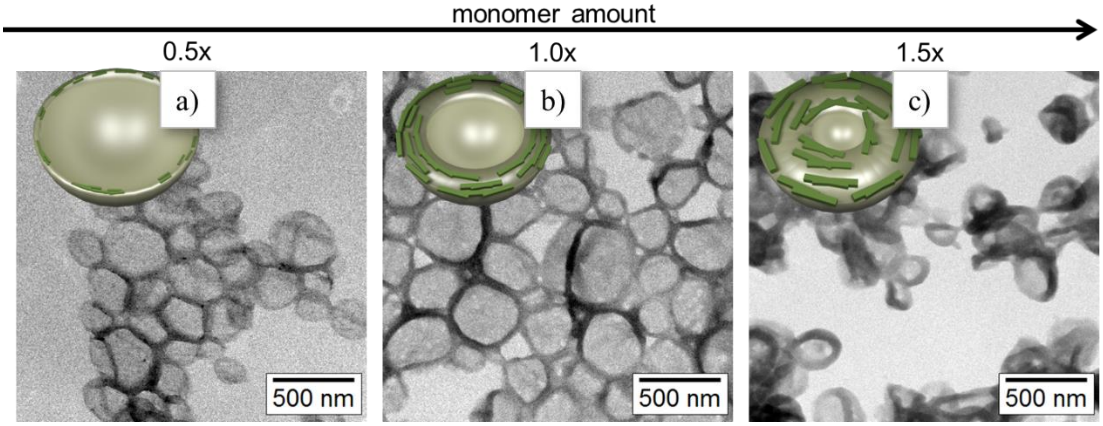

Figure 12: TEM micrographs of polyurea nanocapsules with different shell thicknesses, adjusted by the amount of monomers used for the nanocapsules synthesis. a) 0.5x monomer amount resulted in nanocapsules with a shell thickness of 14 ± 3 nm, b) 1.0x monomer amount resulted in nanocapsules with a shell thickness of 17 ± 4 nm, c) 1.5x monomer amount resulted in nanocapsules with a shell thickness of 23 ± 5 nm.

XRD patterns of polyurea nanocapsules (Figure 13a) exhibit prominent reflections in the region $15° < 2\theta < 27°$, a typical region for polyurea.[126] The reflections indicate the semi-crystalline character of the nanocapsules. XRD patterns showed an increasing degree in crystallinity (from 75% to 88% relative to the bulk) with increasing shell thickness (Figure 13b). As expected, nanocapsules were less crystalline than the bulk polyurea prepared by precipitation polymerization. In the XRD patterns of the nanocapsules samples a reflection at $2\theta = 32°$ is observed, which can be attributed to the NaCl[127] present in the nanocapsules. The area under the reflection caused by NaCl was therefore not included in the calculation of the degree of crystallinity. The relative intensity of the reflection at $2\theta = 32°$ correlates to the ratio of polymer to NaCl. The degree of crystallinity was further analyzed by DSC. In the first heating curve, a melting transition was found for all samples (Figure 13c). To ensure that the nanocapsules confinement was still intact and not destroyed by melting processes only the first heating curve of the DSC measurements was taken into account. With increasing shell thickness, an increase in melting enthalpy was found (Figure 13d), indicating that the nanocapsules were more crystalline.

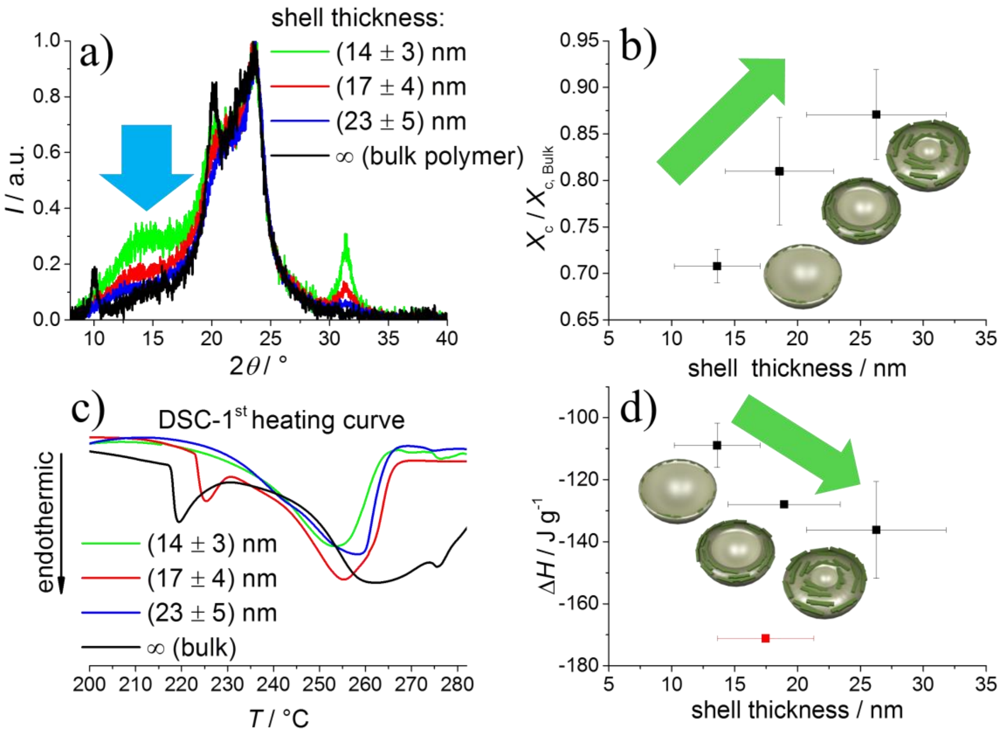

Figure 13: Crystallinity of polyurea nanocapsules. (a) XRD pattern of nanocapsules with different shell thicknesses normalized to the bulk. The crystalline reflections become sharper with increasing degree of crystallinity. (b) Degree of crystallinity extracted from XRD patterns plotted against the nanocapsules shell thickness. The data points were averaged over four samples each. Error bars represent standard deviations. (c) Thermograms during the 1st heating curve in DSC of the dried nanocapsules. (d) Melting enthalpy evaluated from integral of melting peak plotted against shell thickness. The values were averaged over 4 samples. Error bars represent standard deviations. In the DSC data one outlier (red), attributed to a degradation process during DSC heating cycle, was identified (significant outlier, $P < 0.01$) and not taken into account.

A shift of about 30 °C to lower temperatures for the nanocapsules as compared to the bulk material was observed for the crystallization temperature during the DSC cooling cycle (Figure 14).

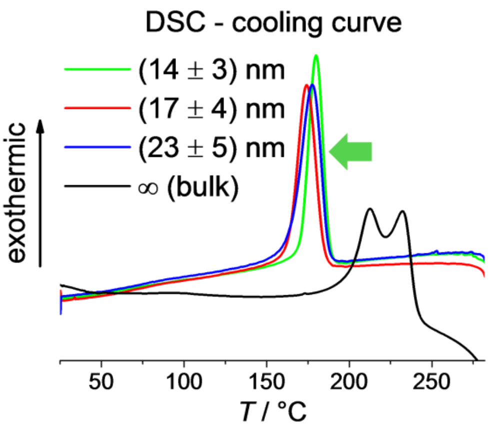

Figure 14: DSC thermogram cooling curve of polyurea: All samples exhibit signals attributed to crystallization. Compared to the bulk material, there is a shift in crystallization temperature of about 30 °C for the dried nanocapsules.

The shift in crystallization temperature can be explained either by the occurrence of a different crystalline phase or by confinement effects. The latter results to higher undercooling derived from the small confining volume of nanocapsules shells. Moreover, as shown in Figure 13c, the DSC thermogram of the bulk and relative thick sample contained two transitions, which is different from the thinner nanocapsules that display only one transition. Indeed, in the bulk, the broad and bimodal melting peaks reflect melting of crystals of variable thicknesses. Under confinement, and especially for the nanocapsules with smaller shell thickness, there is first a reduction in melting temperature and, second, a single melting peak. Both observations suggest the melting of a more uniform crystal of reduced thickness as compared to the bulk. These findings are consistent with finite size effects as described by the Gibbs−Thomson equation.

Dielectric spectroscopy (DS) measurements were carried out by the group of Prof. George Floudas at the University of Ioannina, Greece, on the pure bulk polyurea, the surfactant polyisobutylene succinimide pentamine, and the nanocapsules to investigate their molecular dynamics. In contrast to X-ray scattering, which emphasizes the order within crystalline segments, DS is probing the segmental dynamics for those segments located in amorphous parts. Since all crystallizable polymers are semi-crystalline in nature, X-ray scattering and DS provide complementary information on the structure and molecular dynamics, respectively. Figure 15 presents representative dielectric loss curves of the surfactant, the bulk polymer, and the nanocapsules at the same temperature. The curves indicate higher losses for the more polar surfactant.

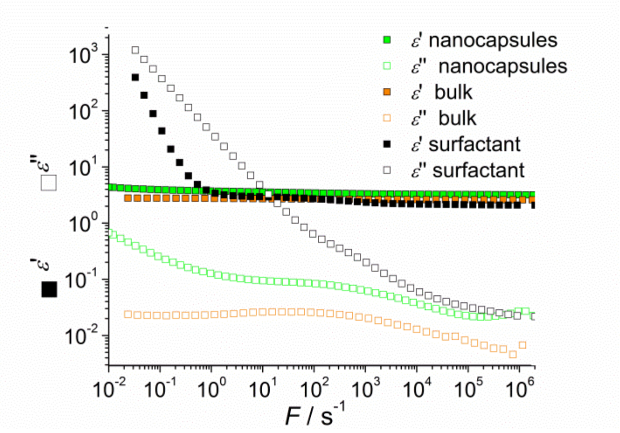

Figure 15: Dielectric permittivity (solid symbols) and loss (open symbols) for the pure surfactant (black), the pure bulk polyurea (orange) and the nanocapsules (green) measured by the group of Prof. George Floudas at the University of Ioannina, Greece. All measurements refer to 22 °C. The bulk polymer and the nanocapsules spectra are of low intensity reflecting the dipolar dynamics in the amorphous part of polyurea.

In addition, the segmental dynamics within the amorphous parts of the bulk material are effectively plasticized by the surfactant, as indicated by the shift of the relaxation times at maximum loss to lower temperatures (Figure 16).

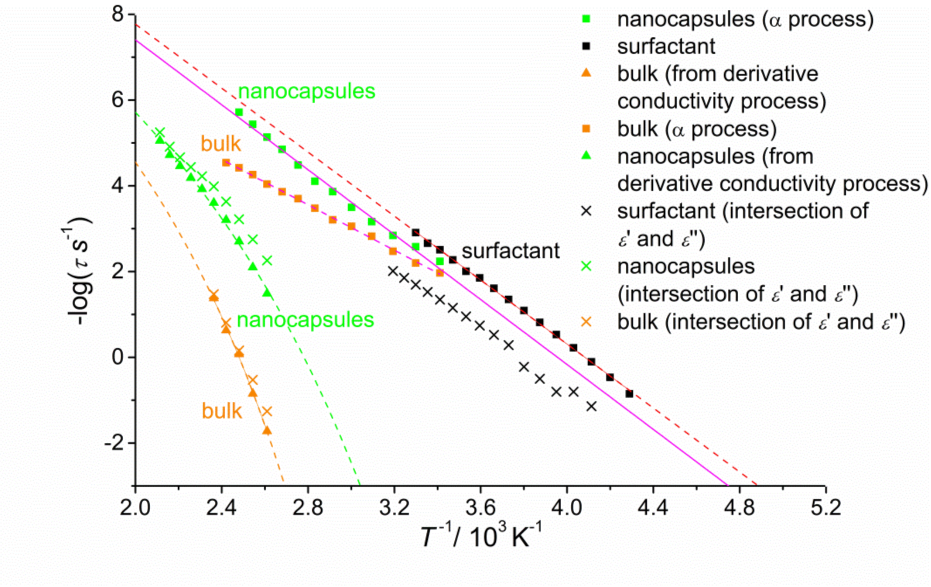

Figure 16: Relaxation map of all dynamic processes in the pure surfactant (black), the bulk polyurea (orange) and the nanocapules (green) measured by the group of Prof. George Floudas at the University of Ioannina, Greece. Crosses indicate the relaxation due to conductivity obtained from the crossing of the real and imaginary parts. Up triangles gives the same process from the derivative of dielectric permittivity. Evidently, pure polyurea in bulk has high conductivity. With squares are molecular processes in the bulk material and the nanocapsules. These molecular processes reflect the dipolar dynamics of polyurea in its amorphous part. Regarding the nanocapsules, this process speeds up reflecting the plasticization of segmental polymer dynamics by the surfactant.

4.1.4.3. Release of Cargo from Semi-Crystalline Nanocapsules

Release experiments were performed by encapsulating a fluorescent dye in the polyurea nanocapsules. The Cy5 molecule was selected because it is a dye presenting a good quantum yield and that is commonly used in biology. The only difference between the nanocapsules with Cy5 and the aforementioned nanocapsules was the presence or absence of Cy5. To evaluate the impact of polymer crystallinity on the diffusion of encapsulated payloads through the nanocapsules shell membrane, nanocapsules with comparable size and shell thickness should be formed. Accordingly, nanocapsules differing only in the diamine were synthesized. Side chain branches act as defects and are known to reduce crystallinity. The methyl group in methylpropane-1,3-diamine (MPDA) disturbs the packing and results in a polyurea (PUA) with a lower degree of crystallinity as compared to polyurea synthesized with 1,4-diaminobutane (DAB). DSC and XRD measurements

(Figure 17) demonstrated that both types of nanocapsules were semi-crystalline.

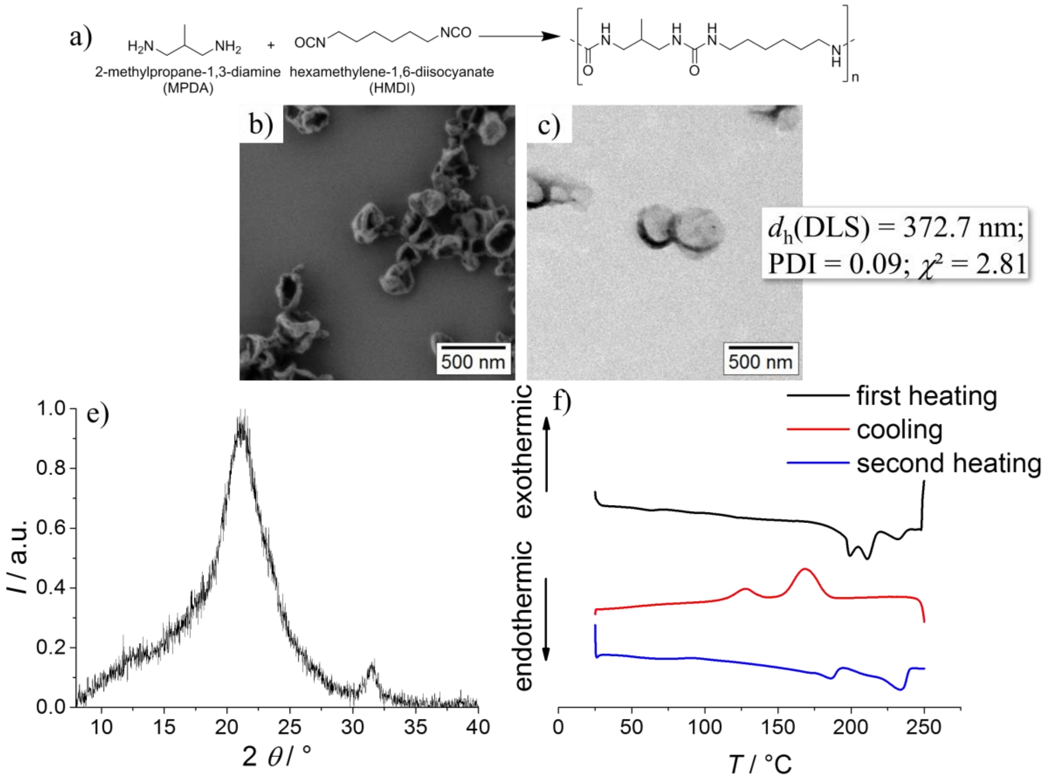

Figure 17: Nanocapsules from MPDA and HMDI. a) Polymerization taking place at the interface of the aqueous nanodroplets upon addition of HMDI. b) SEM and c) TEM micrographs of MPDA-HMDI polyurea nanocapsules. The nanocapsules collapsed due to the measurement conditions. The electron micrographs show nanocapsules formation. d) Results of DLS measurements. e) XRD pattern exhibits one main reflection at $2\theta = 21°$. f) DSC thermogram of nanocapsules made of MPDA-HMDI. The first heating curve shows two melting peaks at 199 °C and at 211 °C, the cooling curve two crystallization temperatures at 128 °C and at 168 °C and the second heating curve two melting peaks at 184 °C and at 234 °C.

The degree of crystallinity of MPDA-PUA nanocapsules was calculated to be roughly 60% of the degree of crystallinity from corresponding nanocapsules made of DAB-PUA. No significant difference in the shell thickness was observed (the shell thickness was 16 ± 3 nm and 16 ± 4 nm for DAB-PUA and MPDA-PUA, respectively). Subsequently, the release of encapsulated Cy5 from nanocapsules was measured during dialysis (Figure 18). Evidently, the MPDA-PUA-based nanocapsules showed a faster release of Cy5 than DAB-PUA-based nanocapsules. After 72 h, roughly twice of the amount of Cy5 was released from MPDA-PUA as compared to DAB-PUA capsules. This confirms that crystalline domains in the nanocapsules shell may act as barriers that hinder Cy5 diffusion. However, it is important to notice that properties such as specific volume and molecular weight are different for the two types of polyurea. This may also influence the release behavior of the payloads from the nanocapsules.

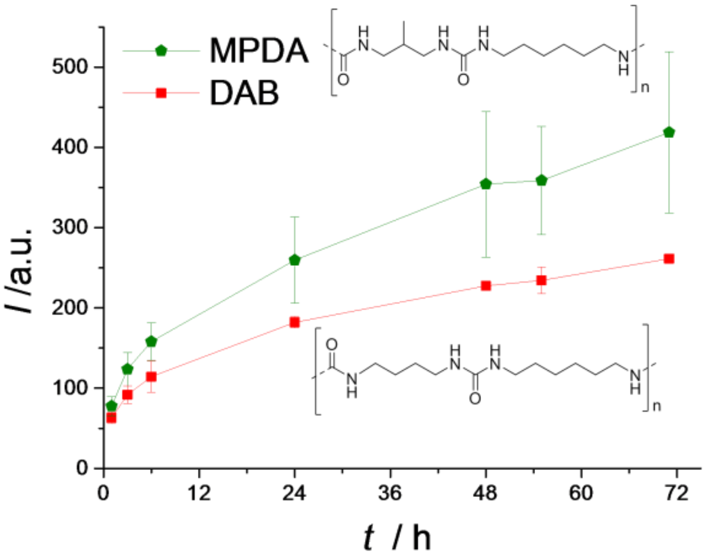

Figure 18: Plot is showing the fluorescence intensity *I* after certain time intervals *t*. The release of Cy5 from nanocapsules with lower degree of crystallinity (green) is faster as compared to the release from nanocapsules with higher degree of crystallinity (red).

4.1.4.4. Semi-Crystalline Polyphosphoester Nanocapsules

To show that the crystallinity of the nanocapsules is not limited to the process and to the nature of polyurea nanocapsules, we prepared nanocapsules from a pre-synthesized semi-crystalline polymer (*i.e.*, polymer not formed in a dispersed medium) in direct miniemulsion. In this case, polymer crystallization is confined between the core formed by polydimethylsiloxane (PDMS) and the outer interface of nanocapsules, which are dispersed in water. Firstly, an organic solution of PDMS and polyphosphoester is prepared and emulsified in an aqueous solution of surfactant. Small droplets are obtained after sonication. The dispersion is then subjected to the evaporation of the organic solvent so that PDMS and the polyphosphoester remain in the dispersed state. Because both polymers are immiscible, an internal phase separation occurs, leading to the formation of core−shell nanoparticles. PDMS is more hydrophobic than the polyphosphoester and therefore the PDMS is in the core of the nanoparticles.

XRD patterns of the nanocapsules and the corresponding bulk material were recorded (Figure 19a). Both exhibit a reflection at $2\theta = 21°$, corresponding to a lattice spacing of 4.1 Å, which can be assigned to the polyethylene unit cell.[123] At $2\theta = 12°$ a halo for PDMS[128] is observed. For the phenoxypolyphosphoester, two crystalline phases were reported: A 2-dimensional orthorhombic unit cell with lattice parameters $a = 7.4$ Å and $b = 5.0$ Å and a pseudohexagonal unit cell with lattice parameters $a = 8.2$ Å and $b = 4.7$ Å.[129] The XRD pattern of the nanocapsules displayed broader reflections than the bulk material. Following the Scherrer equation (eq. 8), the thickness of the crystals L was calculated from the full width at half maximum of the reflections. L was found to be 5 nm for the reflections of the nanocapsules at $2\theta = 21°$. This observation indicates that smaller crystallites are present in the nanocapsules shell as in the bulk material (L = 8 nm).

DSC thermograms of nanocapsules were recorded in the dispersed state to ensure that confinement is kept intact upon melting. The latter was confirmed by DLS, SEM, and TEM measurements made after the thermal treatment experienced during DSC. As for the polyurea nanocapsules also the DSC cooling curves of PPE nanocapsules (Figure 19 b) displayed a shift of 10 °C in crystallization temperature as compared to the bulk material.

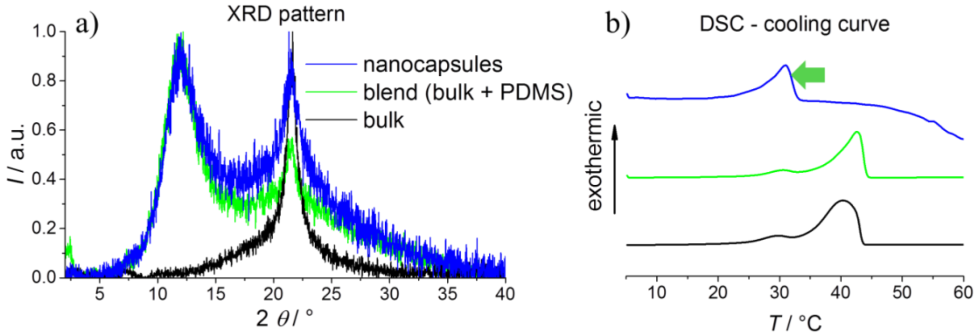

Figure 19: Crystalline character of PPE nanocapsules. (a) XRD pattern and (b) DSC thermogram of nanocapsules (blue) compared to the blend material made of bulk and PDMS (green) and the bulk material (black).

This shift in the crystallization temperature was not observed for nanoparticles made of PPE (Figure 20).

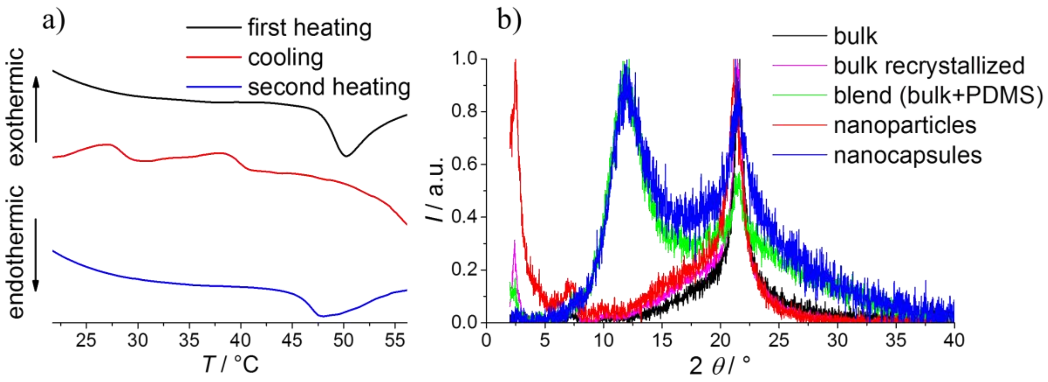

Figure 20: a) DSC thermogram of PPE nanoparticles. The DSC thermogram was measured in dispersion to keep nanoparticle confinement upon melting. Melting and crystallization temperatures do not differ significantly from the bulk material. b) XRD pattern of phenoxypolyphosphoester: Bulk material as synthesized (black); bulk material (treated like nanocapsules) (pink); nanoparticles (synthesized in the same way as nanocapsules, but without addition of PDMS), (red); blend consisting of a mixture of bulk and PDMS (green) and nanocapsules (blue). All XRDs exhibit a reflection at $2\theta = 21°$, which corresponds to the PE crystal structure. The blend material as well as the nanocapsules show a halo at $2\theta = 11°$ caused by PDMS. For the recrystallized bulk material (green, pink) as well as for the nanoparticles (red), reflections in the small angle region appear, corresponding to the crystalline stem of the crystal lamellae.[123]

4.1.5. Conclusions

It is shown that the permeability of the nanocapsules shell and therefore the release of small molecules depend not only on the thickness of the polymer shell, but also strongly on the degree of crystallinity of the semi-crystalline polymer. The degree of crystallinity can be further tuned by the molecular structure of the polymer. Increasing degree of crystallinity in the shell acts as a barrier and effectively hinders molecular diffusion from the capsules. This opens the way to construct nanocapsules with a tunable permeability for defined release kinetics.

4.2. Highly Loaded Semi-permeable Nanocapsules for Magnetic Resonance Imaging

The improved encapsulation capacities of semi-crystalline nanocarriers, presented in Chapter 4.1 are used for the encapsulation of a commercial MRI contrast agent. An aliphatic polyurea allowed for the synthesis of highly loaded nanocarriers with improved relaxivity.

4.2.1. Abstract

Magnetic resonance imaging has become an essential tool in medicine for the investigation of physiological processes and for the detection of tumors in the body. The key issues related to contrast agents, *i.e.*, substances that are injected in the body for imaging, are the efficient enhancement of contrast, their low toxicity, and their defined biodistribution. We describe here polyurea nanocapsules containing the gadolinium complex Gadobutrol as contrast agent in high local concentration and high relaxivity up to 40 $s^{-1}mmol^{-1}L$ (Figure 21). A high concentration of the contrast agent inside the nanocapsules could be ensured by increasing the crystallinity in the shell of the nanocapsules. Nanocapsules from aliphatic polyurea were found to display higher crystallinity and higher relaxivity at an initial Gadobutrol concentration of 0.1 M than aromatic polyurea nanocapsules. The nanocapsules and the contrast agent were clearly identified in cells. After injection, the nanocarriers containing the contrast agent were mostly found in the liver and in the spleen, which allowed for a significant contrast enhancement in magnetic resonance imaging.

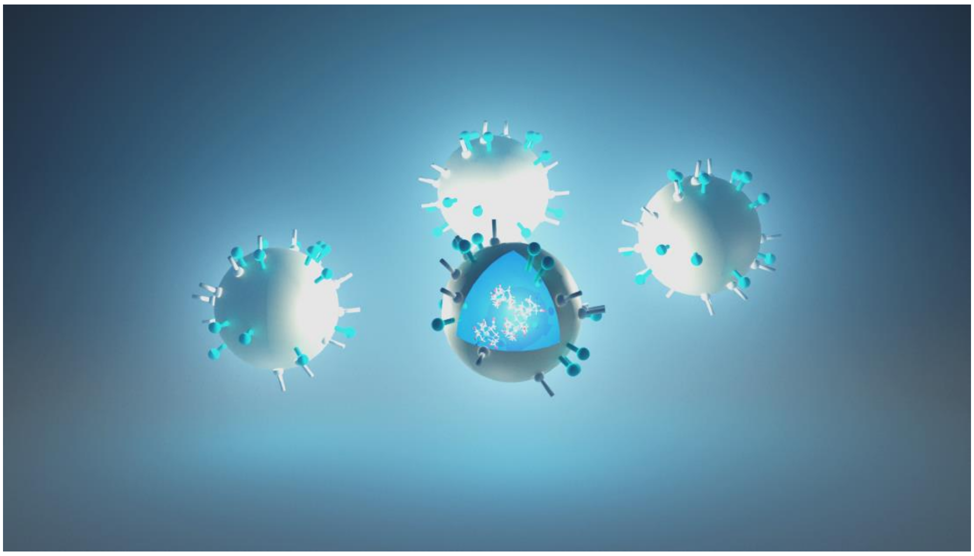

Figure 21: Shining light in darkness with hollow sphere nanocapsules containing the MRI contrast agent Gadobutrol. The contrast enhancing effect of the contrast agent is increased by a factor of 10 by encapsulation.

4.2.2. Introduction

The identification of tumors in human body is essential to increase the chances of patients' early and adequate treatment.[130-133] Magnetic resonance imaging (MRI) is now a common medical technique that is used in radiology to visualize the anatomy and the physiology of patients. A good contrast is achieved only by employing contrast agents,[134-138] the most common being based on gadolinium(III) complexes,[5,139,140] which usually accelerate the relaxation of water protons in the tissue of the patients.

The key issue is to increase the contrast without adverse effects for the body, such as toxicity or other side effects. Therefore, one of the main scientific questions associated to this issue is: How can we increase the relaxivity of gadolinium(III) agents with a limited concentration in the body?

This issue was addressed by materials scientists and medical doctors who designed different types of materials. One strategy is to produce materials with high local concentration of gadolinium(III) realized by the fabrication of nanoparticles of gadolinium(III) oxide Gd_2O_3 [141-143], gold nanoparticles with adsorbed gadolinium complexes,[144,145] metal-organic frameworks with gadolinium,[146] conjugates of gadolinium chelates on virus capsids,[147] dendrimers containing gadolinium,[148-151] gadofullerenes,[44,152,153] or precipitated complex forming nanoparticles stabilized by polyelectrolytes.[154]

In other approaches gadolinium(III) complexes were embedded in lipid-based nanoparticles[155] and silica nanocontainers.[156,157] Polymer nanoparticles were also investigated as nanocarriers for the gadolinium complexes for magnetic resonance imaging.[158-162] An alternative to the encapsulation of gadolinium complexes is to design polymer nanocapsules, *i.e.* polymer nanoparticles with a core-shell structure consisting of a liquid aqueous core and a polymer shell.[92,106] Still, the gadolinium complex relies here on a fast proton exchange. Since within the nanocapsule, the water to gadolinium ratio may not be high enough the polymer shell has to be permeable for protons/water from the continuous phase, while being impermeable for the gadolinium complex so that the complex is trapped inside. The nanocapsules can be synthesized by interfacial polyaddition in a water-in-oil miniemulsion system.[117] Poly(urthane/urea) nanocapsules were prepared by interfacial polyaddition for the encapsulation of contrast agents based on gadolinium complexes.[9,118,163] Sharma *et al.* reported on poly(urethane/urea) nanocapsules carrying $2.5 \cdot 10^6$ Gd^{3+} complexes per nanocapsule with a particle-based relaxivity of $\sim 10.8 \cdot 10^6\ mM^{-1}s^{-1}$.[163] By co-encapsulating sucrose with the contrast agent, the viscosity and, therefore, the relaxivity was increased by a factor of 6 compared to an aqueous solution of the contrast agent[9] and to the nanocapsules previously presented by Sharma *et al.*[163] However, in this study the gadolinium concentration in the nanocontainers was low (up to ~0.07 M) and encapsulating higher amounts of contrast agent (an initial Gadobutrol concentration of >100 mM) yielded to a leakage which occurred due to osmotic pressure.[9]

To our knowledge it was not possible so far to combine high relaxivity of a gadolinium-based MRI contrast agent with high local contrast agent concentrations in nanocapsules. To obtain a MRI signal at low local capsule concentration, the internal concentration of the gadolinium complex has to be significantly increased. This requires the construction of shells which can withstand the higher osmotic pressure inside the capsule, but still allowing water permeability. To entrap the contrast agent efficiently even at a shell thickness less than 30 nm, the implementation of crystallinity[43] in the shell is thought to be a feasible way.

Herein, we encapsulate the gadolinium(III) complex Gadobutrol, a commercial contrast agent for MRI, in semi-crystalline polyurea nanocapsules with the aim to maximize the concentration and at the same time to maximize the relaxivity of the contrast agent. We compare aliphatic polyurea leading to a higher crystallinity of the shell and aromatic polyurea with a lower crystallinity of the shell. By treating nanocapsules with proteins, a protein corona around the nanocapsules is formed which increases the colloidal stabilization of the nanocapsules and at the same time determines the biological identity of the nanocarriers.[164,165] The protein corona is analyzed by SDS-PAGE and LC-MS. The initial assessment of the non-toxicity of the nanocapsules is proven by cell experiments using dendritic and mesenchymal stem cells. Mesenchymal stem cells were chosen because they show self-renewal while still being multipotent.[166] Dendritic cells are primary cells with a higher sensitivity to toxic agents than immortalized or tumor derived cell lines. Moreover, dendritic cells belong to the 'professional' antigen-presenting cells and thus are part of the most important cells of the immune system.[167] They provide exact information of location, type, and strength of inflammations to T-lymphocytes. Therefore, they are ideally suited as drug transporting cells.[168] The contrast enhancement after intravenous application of the nanocapsules was analyzed in mice by magnetic resonance imaging.

4.2.3. Materials and Methods

Materials

Hexamethylene-1,6-diisocyanate (HMDI, ≥ 99.0%), toluene-2,4-diisocyanate (TDI, 95%, filtrated over 0.2 µm nylon syringe filter (Chromacol) prior to use), and tetrahydrofuran (THF, HPLC grade) were purchased from Sigma Aldrich. Cyclohexane (HPLC grade) was purchased from VWR. 1,4-Diaminobutane (DAB, 98+%) was purchased from Alfa Aesar. Sodium dodecyl sulfate (SDS, 99%) was purchased from Fluka. Dulbecco's phosphate buffered saline (PBS) (no calcium, no magnesium) was purchased from Sigma Aldrich. The surfactant polyisobutylene-succinimide pentamine was obtained from Lubrizol France. The fluorescent dye Cy5-oligo (an oligonucleotid with the sequence CCACTCCTTTCCAGAAAACT, modified with Cy5 at 5' position) was purchased from Thermo Fisher Scientific GmbH. Gadobutrol (Gadovist, 1.0 M solution for injection) was kindly provided by Bayer Healthcare. Gadolinium standard for the inductively coupled plasma (ICP) measurements was purchased from VWR International GmbH. All chemicals were used as received unless noted otherwise. Milli-Q water (18 MΩ cm) was used for all experiments.

Synthesis of polyurea nanocapsules

Gadobutrol was diluted with PBS to the desired concentration ranging from 5 mM to 1 M. To 1.4 mL of the Gadobutrol solution, 1,4-diaminobutane (DAB, 1 mmol) was added. To visualize the nanocapsules in cells, the fluorescent dye Cy5-oligo (29.01 nmol) was added to the aqueous solution. The surfactant polyisobutylene-succinimide pentamine (100 mg) was dissolved in cyclohexane (7.5 g). The aqueous phase was added to the organic phase and the mixture was placed in an ultrasonic bath for 10 min to obtain a coarse emulsion. Sonication of the emulsion was performed under ice-cooling using a Branson W450-D sonifier equipped with a 1/2 inch tip. The sample was sonicated for 3 min at 70% amplitude with a pulse-pause regime of 20 and 10 s, respectively. The diisocycanate (1.5 mmol) was dissolved in cyclohexane (2.5 g) and added dropwise to the miniemulsion under stirring (900 rpm). The sample was kept stirring (900 rpm) for 24 h at room temperature in a closed glass vial. For thermogravimetric analysis (TGA), differential scanning calorimetry (DSC), scanning electron microscopy (SEM) and transmission electron microscopy (TEM) measurements, the nanocapsule dispersions in cyclohexane were purified by centrifugation at 5,000 rpm for 30 min. The supernatant was removed, the nanocapsules were dispersed in THF, and the centrifugation step was repeated. The nanocapsules were dispersed in cyclohexane and freeze-dried.

Transfer of nanocapsules from cyclohexane into water

1 g of non-purified nanocapsule dispersion in cyclohexane was added dropwise to 5 g of 0.3 wt% SDS solution placed in an ultrasonic bath. Cyclohexane was evaporated by stirring the sample (900 rpm) at room temperature in a glass vial with an open lid for 24 h.

The nanocapsules dispersions in water were purified by centrifugation at 5,000 rpm for 1.5 h. The supernatant was removed and the nanocapsules were dispersed in the same amount of fresh SDS solution as removed before.

The gadolinium (complex) concentration in the nanocapsule dispersion and in the supernatant was determined by inductively coupled plasma-optical emission spectrometry (ICP-OES). The aqueous supernatant was filtrated over a 0.2 µm nylon syringe filter prior to ICP-OES analysis in order to withdraw nanocapsules that have not been removed during centrifugation. To monitor the leakage from nanocapsules, the purification was performed on non-purified nanocapsules in water after 1 week and after 3 weeks and was compared to the initially encapsulated Gadobutrol (Figure 22).

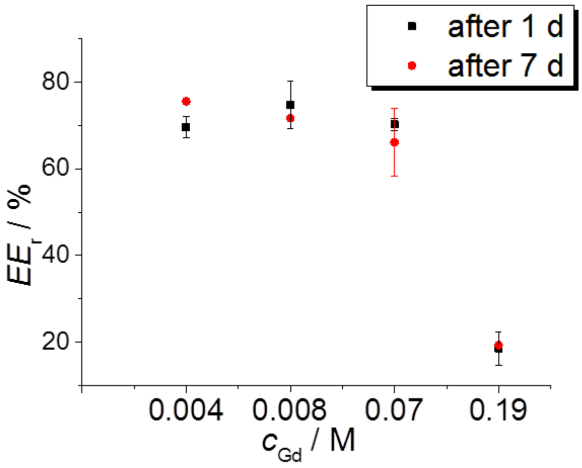

Figure 22: Encapsulation efficiency after the transfer to water *EE*$_r$% after 7 days compared to *EE*$_r$% measured after 24 h. There are only minor differences between the encapsulation efficiency after 24 h and after 7 days. For the nanocapsules of aromatic polyurea (not shown), the difference was also negligible.

Purification of nanocapsules dispersions for bioimaging

Nanocapsules synthesized with 100 mM initial Gadobutrol concentration were tested in bioimaging experiments. After the transfer into water, the nanocapsules dispersion was stabilized with 2% FBS (Gibco, Thermo Fisher) for 1 h at room temperature and dialyzed first against sterile water and subsequently against PBS solution using a 14,000 MWCO regenerated cellulose dialysis membrane (Carl Roth). After the purification, the nanocapsules in dispersion had a diameter of ~ 500 nm and a solid content of (0.61 ± 0.09) wt%. The zeta potential was found to be -(33.3 ± 0.3) mV. The Gadobutrol concentration was determined to be 1.2 ± 0.1 mM in the nanocapsule dispersion. The proteins adsorbed on the nanocapsule surface during the treatment with FBS were analyzed by SDS-PAGE and LC-MS (Figure 31).

Polyurea synthesis in bulk

1,4-Diaminobutane (DAB, 2 mmol) and optionally 1 M Gadobutrol solution (280 µL) were dissolved in a mixture of tetrahydrofuran (THF, 10 mL) and water (5 mL). HMDI (2 mmol) dissolved in THF (5 mL) was added dropwise to the DAB solution. The mixture was stirred at room temperature for 24 h. The precipitate was purified via centrifugation at 10,000 rpm for 5 min, washed two times with a THF-water mixture and one time with cyclohexane. The polymer was dispersed in cyclohexane and freeze dried.

Protein adsorption

The protein adsorption was analyzed by Johanna Simon. Nanocapsules were centrifuged (20,000 g, 4 °C) for 5 min and the remaining supernatant was kept for protein analysis. The resulting nanocapsule pellet was washed with PBS (3x, 1 mL, Gibco) to remove loosely bound proteins. Proteins were desorbed with 2% SDS + 62.5 mM Tris-HCl (Sigma). Samples were incubated 5 min, 95 °C and centrifuged (20,000 g, 4 °C). The remaining supernatant contains desorbed hard corona proteins. The amount of the protein solution was quantified using Pierce 660nm Assay (Thermo Fisher) according to the manufactors´ instructions.

SDS-PAGE

Sodium dodecyl sulfate-polyacrylamide gel electrophoreses (SDS-PAGE) to identify the proteins adsorbed on the nanocapsules surface was carried out by Johanna Simon. A total amount of protein (6 µg) was added to NuPage Reducing agent (4 µL), NuPAGE LDS Sample buffer (10 µL) and loaded onto a NuPage 10% Bis Tris Gel. The gel was run for 1 h at 100 V in NuPAGE MES SDS Running Buffer using SeeBlue Pre-Staining Standard as marker. Protein bands were visualized using Simply Blue safe stain (all Thermo Fisher).

LC-MS

Liquid chromatography-mass spectrometry (LC-MS) was performed by Johanna Simon to quantify the proteins adsorbed on the nanocapsules surface. Prior to in-solution digestion, SDS was removed via detergent removal columns (Thermo Fisher) and proteins were precipitated with Proteo Extract protein precipitation kit (Millipore) overnight. The resulting protein pellet was resuspended with 0.1% RapiGest SF (50 mM ammonium bicarbonate solution, Waters). The solution was incubated at 80 °C for 15 min and afterwards dithiothreitol (Sigma) was added (5 mM) to reduce the disulfide bonds (45 min, 56 °C). Iodoacetamide (Sigma) was added (15 mM) and the protein solution was incubated in the dark for 1 h. Digestion was performed overnight at 37 °C using a trypsin (Promega) to protein ratio of 1:50. Hydrochlorid acid (2 µL) was added to stop the digestion and the remaining peptide solution was centrifuge for 15 min at 4 °C. Peptide samples were diluted 1:5 with 0.1% formic acid and 50 fmol·μL^{-1} Hi3 EColi Standard (Waters) was supplemented for absolute quantification.

Proteomic analysis was performed using a Synapt G2 Si mass spectrometer coupled to NanoACQUITY UPLC with a C18 analytical reversed-phase column (1.7 µm, 75 µm x 150 mm) and a C18 nanoACQUITY Trap Column (5 µm, 180 µm x 20 mm, both Waters). Mobile phase A consists of 0.1% (v/v) formic water and mobile phase B of 0.1% (v/v) formic acetonitrile. Peptides were injected with a flow rate of 0.3 µL·min^{-1} over a gradient over 2–40% from mobile phase A to B. Glu-Fibrinopeptide and Leucine Enkephaline (both Sigma) were infused at a flow rate of 0.5 µL·min^{-1} and served as reference component. A NanoLockSpray source was used for electrospray ionization (ESI) in positive ion mode. Data-independent acquisition (MSe) experiments were performed over a mass to charge range of *m*/*z* 50–2,000 Da, using a trap collision energy (20–40 V), scan time of 1 s and total run time of 90 min. Data acquisition and processing were carried out using MassLynx 4.1.

Proteins were identified by Progenesis QI software. For data analysis, the noise reduction thresholds for low energy (120 counts), high energy (25 counts) and peptide intensity (750 counts) were set and continuum LC-MS data was post acquisition lock mass corrected. A protein false discovery rate of 4% was chosen. Peptides were searched against a reviewed database from Uniprot. The sequence of Hi3 Ecoli standard (Waters) and porcine trypsin was added. A peptide was identified if at least three assigned fragments were found and for protein identification least two assigned peptides and five assigned fragments are needed. Further criteria were set: Max. protein mass 600 kDa, one missed cleavage, fixed carbamidomethyl modification and variable oxidation. With a Top/Hi3 approach the amount of each protein in fmol was calculated. Relative amounts of each protein were calculated based on the total amount of all identified proteins.

Distribution of nanocapsules in human mesenchymal stem cells and in dendritic cells

The distribution of gadolinium in human mesenchymal stem cells and in dendritic cells was analyzed by Dr. Patricia Renz. For the visualization of fluorescently labeled nanocapsules containing Gadobutrol, approximately 100,000 cells (human mesenchymal stem cells (MSC) cell line and dendritic cells (DC) from primary monocytes) were seeded in a 24 well plate and were incubated for 24 h with the polyurea nanocapsules. The incubated cells were stained with cell mask green (MSCs) or Oregon Green® (DCs) in order to stain the cell membrane. After the incubation time, MSCs were removed from the substrate by using trypsin. The imaging was carried out with a Leica SP5 confocal laser scanning microscope (cLSM).

Cytotoxicity measurements

The cytotoxicity of the nanocapsules was determined by Dr. Patricia Renz. Approximately 100,000 to 200,000 cells were seeded and incubated with the nanocapsules for 24 h the next day. Subsequently the cells were removed with trypsin, washed with phosphate-buffered saline solution PBS and stained with 2 $\mu g \cdot mL^{-1}$ propidium iodide (PI). Measurements were conducted at a wavelength of 488 nm in a 40 mW Partec CyFlow ML.

MRI experiments

All animal procedures and experiments were carried out according to the guidelines of the German Regulations for Animal Welfare in collaboration with the Department of Nuclear Medicine, University Medical Center Mainz, Germany by Dr. Stefanie Pektor and Nicole Bausbacher. The protocols were approved by the local Ethical Committee for Animal Experiments (Landesuntersuchungsamt Rheinland Pfalz). The nanocapsule dispersion was tested in ten 6–8 week old C57B1/6J mice (Janvier, France). The mice were anaesthetized with 2% isoflurane vaporized in 70% O_2. The desired amount of nanocapsules dispersion or non-encapsulated contrast agent was diluted to a total volume of 200 µL with PBS solution and injected intravenously via the tail vein. The MRI measurements were performed with a 1.0 T Mediso nanoScan PM PET/MRI *in vivo* molecular and preclinical imager (Mediso, Hungary). A Gradient Echo Spoiled External Averaging was chosen as T_1 weighted 3D sequence. The measurement parameters were: $T_R = 13.6$ ms, $T_E = 2.9$ ms, Flip Angle: 20°, FOV 60x60 mm, 32 slices, 1 mm slice thickness, Exc: 2; measurement time ~4 min. The magnetic resonance images were recorded before the injection (0 min), and 2 min *p.i.*; 15 min *p.i.* and 1 h *p.i.* For one mouse, the magnetic resonance images were recorded 18.5 h *p.i.*

Biodistribution of the nanocapsules in mice

After the MRI experiments, the mice were sacrificed and the organs were removed by Dr. Stefanie Pektor and Nicole Bausbacher. The organs were freeze-dried, weighted, and digested in a mixture of 65% HNO_3 and 35% H_2O_2 (6:4, v/v) in a closed vessel under microwave heating at 170 °C. The solution was diluted with MiliQ water and the gadolinium content was analyzed by ICP-OES. Calibration solutions were obtained by diluting a commercial gadolinium standard in the same solvent mixture as used for the organs, namely of HNO_3, H_2O_2 and water. For calibration and quantification of gadolinium in the mice organs, the emission lines at 342.247 nm and at 376.839 nm where chosen. The absolute amount of gadolinium found in the tissue was divided by the injected dose (ID) and the weight of the respective tissue. The results are presented as percentage injected dose per gram tissue.

Analytical Tools

Dynamic light scattering (DLS) performed with a PSS Nicomp Particle Sizer 380 at a scattering angle of 90° was used to determine the hydrodynamic radius and size distribution of the nanocapsules. The nanocapsule dispersions were diluted with cyclohexane or water for DLS measurements. The results of DLS measurements are listed in Table 2. A LEO (Zeiss) 1530 Gemini field emission microscope at an extractor voltage of 0.2 kV was used to record scanning electron microscopy (SEM) images. For transmission electron microscopy (TEM) images a

JEOL JEM-1400 electron microscope operating at an acceleration voltage of 120 kV was used. The sample preparation for SEM and TEM was performed by drop-casting the diluted nanocapsule dispersion with a solid content of about 0.01 wt% onto a silicon wafer or onto a carbon-coated copper grid, respectively. TEM imaging of biological samples and the energy filtered TEM spectrum imaging were performed using a FEI Tecnai F20 electron microscope operating at an acceleration voltage of 200 kV. MSCs or DCs were incubated with polyurea nanocapsules for 40 min before the cells were fixed by high pressure freezing (HPF) followed by freeze substitution and finally ultramicrotomy by Dr. Patricia Renz. For every sample, the solid content of the cyclohexane and aqueous nanocapsules dispersions were assessed gravimetrically by weighing 100 µL of sample before and after freeze-drying. The solid contents are listed in Table 2. A Mettler Toledo ThermoSTAR TGA was used for thermogravimetric analysis (TGA) by Petra Räder. The experiments were run in a nitrogen atmosphere and a temperature program heating from 25 °C to 800 °C with a heating rate of 10 $°C \cdot min^{-1}$. Differential scanning calorimetry (DSC) measurements were performed on a Mettler Toledo DSC 3+ calorimeter. DSC measurements were performed in a closed 100 µL aluminum crucible in a N_2 atmosphere (30 $mL \cdot min^{-1}$). In three cycles, the sample was heated, cooled, and heated again with a heating and cooling rate of 10 $°C \cdot min^{-1}$. DSC measurement results were analyzed using the software STAR^e 14.00 provided by Mettler Toledo. A Philips PW 1820 diffractometer with monochromatic Cu$K\alpha$ radiation ($\lambda = 1.54$ Å) at 30 kV (5 s, $\Delta\theta = 0.02°$) was used by Michael Steiert for X-ray diffraction (XRD) analysis. The ratio of the area under the reflexes to the area under the total XRD pattern was used to calculate the degree of crystallinity. Prior to the integration, a background correction was performed. The crystalline contribution was obtained by subtracting the amorphous part from the XRD pattern by underground correction (Figure 23).

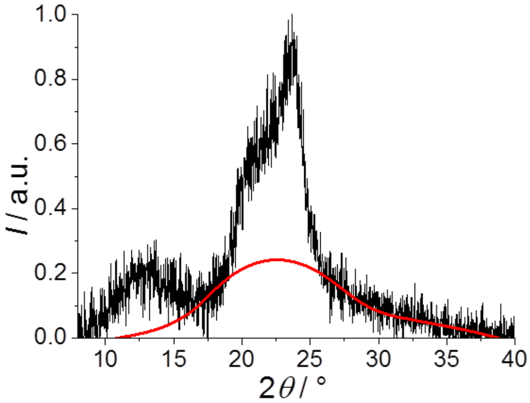

Figure 23: Calculation of the degree of crystallinity from XRD patterns. An amorphous halo (red) was drawn into the XRD pattern (black). The degree of crystallinity was calculated as the ratio of the integral under the reflexes, obtained by subtracting the amorphous halo from the XRD pattern, to the integral of the whole XRD pattern. Prior to the evaluation, a background correction was performed.

The encapsulation efficiency after re-dispersion in water $EE_r\%$ was evaluated from the ratio of the concentration of gadolinium in the filtrated supernatant after centrifugation of the aqueous dispersion c_s to the gadolinium concentration in the nanocapsules dispersion before purification c_t (eq. 11).

$$EEr\% = 1 - \frac{c_s}{c_t} \tag{11}$$

To determine the concentration of gadolinium, inductively coupled plasma-optical emission spectroscopy (ICP-OES) was performed using a Horiba Jobin Yvon Activa M spectrometer equipped with a Meinhardt-type nebulizer and a cyclone chamber. The results were collected using the software ACTIVAnalyst 5.4. For the ICP-OES measurements, the following conditions were chosen: 1250 W forward plasma power, 12 L·min^{-1} Ar flow, and 15 rpm pump flow. The Ar emission at 404.442 nm was chosen as reference line. For calibration and quantification of gadolinium, the emission lines at 354.936 and at 358.496 nm with a 5 s integration time were chosen. Five different gadolinium concentrations were used for calibration. The solutions for the calibration were prepared by dilution of a commercial gadolinium standard for ICP with 0.3wt% SDS aqueous solution. To obtain concentrations within the calibration range, the samples were diluted with a 0.3wt% aqueous solution of SDS. The baseline correction and the dynamic underground correction were provided by the software ACTIVAnalyst 5.4. The relaxation times T_1 and T_2 were measured using a Bruker Minispec mq 20 operating at 20 MHz (0.5 T). The measurements were recorded at a temperature of 37 °C. The T_1 and T_2 relaxation times were measured with a saturation recovery sequence and a Carr-Purcell-Meiboom-Gill (CPMG) spin echo method, respectively. To determine the transversal relaxation time T_1, the spectra were recorded and integrated by the software *the minispec* (Bruker) for 10 different relaxation delays. The resulting data points were fitted with a monoexponential curve to give the T_1 time. The relaxation time T_2 was obtained by monoexponential fit of the CPMG data. The relaxivities were obtained as the slope of a linear fit on the inverse relaxation times for 3 different concentrations per sample and pure SDS solution without Gadobutrol as $x = 0$. Zeta potential was measured using a Zetasizer ZEN2600 system from Malvern Instruments. The sample was diluted with 1 mM potassium chloride and three measurements were run per sample with 10-100 runs per measurement.

4.2.4. Results and Discussion

The contrast enhancing effect of a contrast agent for MRI is directly correlated with two crucial points, the concentration of the contrast agent and its relaxivity, *i.e.*, the enhancing contrast effect per contrast agent molecule. By encapsulating contrast agents in polymer nanocontainers, both challenges, increasing local concentration of the contrast agent and relaxivity, are addressed. Nanocapsules with an aqueous core were synthesized in inverse miniemulsion.

4.2.4.1. Comparison between Aliphatic and Aromatic Polyurea

Aliphatic and aromatic polyurea as shell material are compared to maximize the encapsulation efficiency. The aliphatic polyurea is known to exhibit a higher degree of crystallinity[126] compared to an aromatic polyurea based on the monomers TDI and DAB. As in TDI the diisocyanate groups are angled, the degree of crystallinity is reported to be rather low.[169] However, a higher degree of crystallinity is expected to increase the encapsulation efficiency.[116] In addition to the loading capability, the relaxivity of the encapsulated contrast agent will be addressed, as it is strongly dependent on the barrier properties of the surrounding nanocapsule shell.

The formation of nanocapsules was confirmed by scanning and transmission electron microscopy (SEM and TEM, Figure 24a–b). The amount of Gadobutrol inside and outside the nanocapsules was quantified by ICP-OES measurements. The encapsulation efficiency was calculated from ICP-OES results (eq. 11). By using an aliphatic shell material, the loading after the re-dispersion in water (effective encapsulation efficiency, EE_r%) was increased from ~46% for the aromatic polyurea to ~70% for the aliphatic polyurea at an initial Gadobutrol concentration of 100 mM.

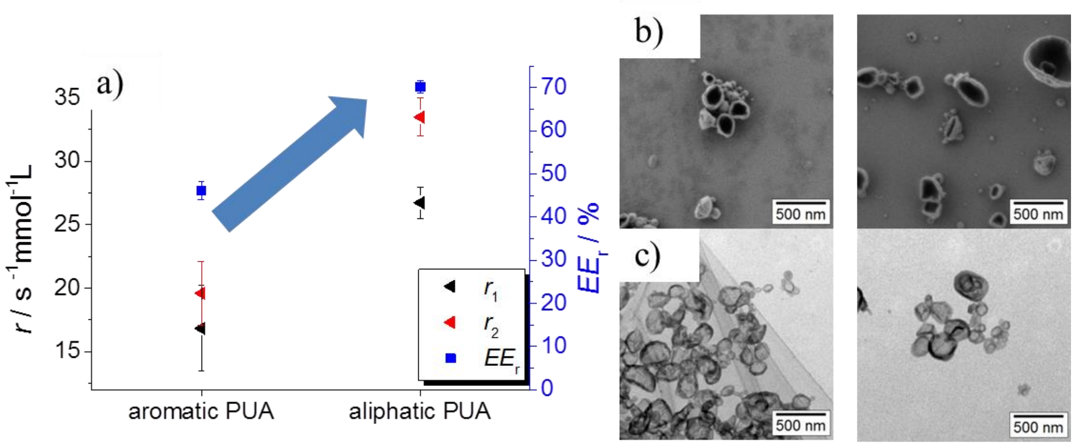

Figure 24: Comparison between aromatic (left) and aliphatic (right) polyurea nanocapsules. a) Relaxivity r_1 (black) and r_2 (red) (left y-axis) and encapsulation efficiency after the transfer to water EE_r% (blue, right y-axis). By replacing an aliphatic polyurea as nanocapsule shell material instead of an aromatic polyurea, the relaxivity is increased by a factor of 2 and the encapsulation efficiency is increased from ~46% to ~70%. b) SEM and c) TEM micrographs of polyurea nanocapsules reveal a core-shell morphology.

Furthermore, the relaxivity r_1 increased from ~17 to ~27 $s^{-1}mmol^{-1}L$ (Figure 24a). The semi-crystalline character of the nanocapsules was examined by XRD and DSC (Figure 26). The degree of crystallinity was determined by delimiting the amorphous halo and comparing the area under the crystalline peaks to the total area of the XRD pattern. The XRD of the aromatic polyurea revealed a mainly amorphous material. Very broad but characteristic reflexes[169,170] were observed at $2\theta = \sim 11$ and ~22°. For the aliphatic polyurea nanocapsules, the reflexes were sharper than those for the aromatic system and the degree of crystallinity was evaluated to be about 55%. Reflexes appeared in the angular region $10° < 2\theta < 30°$, as reported previously for hexamethylene polyurea prepared of hexamethylene-1,6-diamine and hexamethylene-1,6-diisocyanate.[126] Based on the

XRD patterns, the aromatic polyurea nanocapsules that displayed a very large amorphous halo were less crystalline than the aliphatic polyurea nanocapsules. In the DSC thermograms, melting and crystallization peaks were observed only for the nanocapsules of aliphatic polyurea. TGA measurements revealed that the aromatic polyurea started to degrade at temperatures above 250 °C (Figure 25).

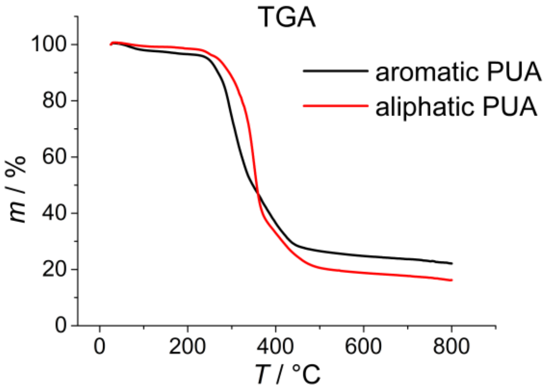

Figure 25: TGA of aliphatic and aromatic polyurea. The mass of the sample *m* is plotted against the temperature *T*. The nanocapsules based on aromatic polyurea degrade at lower temperatures than the aliphatic ones. The TGA of the aromatic polyurea exhibits an inflection point at 297 °C. The inflection point in the TGA of aliphatic polyurea is shifted of 60 °C to 357 °C. DSC settings were chosen on basis of TGA results.

The endothermic peak observed in the first heating curve of the aromatic polyurea was not confirmed by other peaks in the cooling or second heating cycle. For the aliphatic polyurea, melting and crystallization peaks are observed. The melting peak in the first heating curve exhibits a melting enthalpy that is roughly three times larger than the endothermic signal measured for the aromatic polyurea, implementing a larger degree of crystallinity for the aliphatic polyurea.

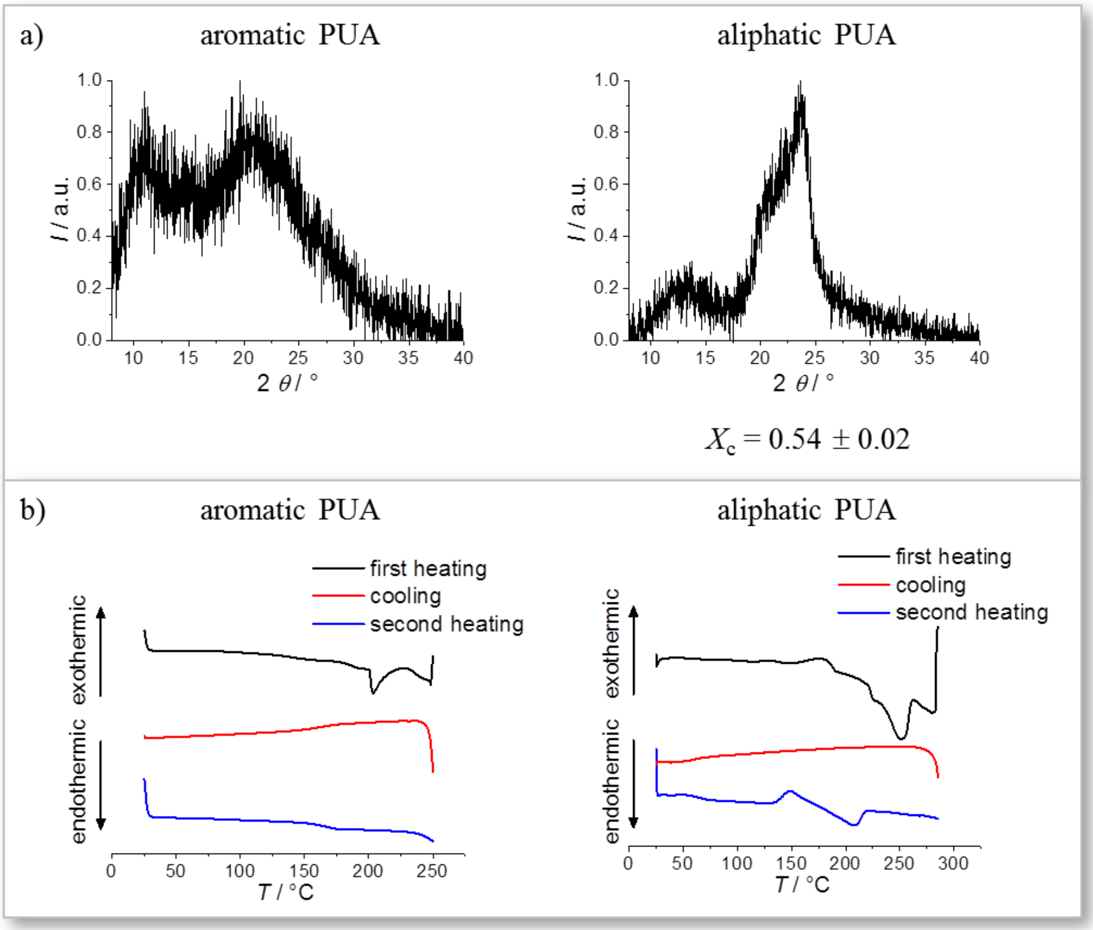

Figure 26: Crystallinity of aromatic (left) and aliphatic (right) polyurea nanocapsules. a) XRD patterns reveal a higher degree of crystallinity for the nanocapsules of aliphatic polyurea (X_c ~0.55) compared to the nanocapsules of aromatic polyurea, which are found to be mostly amorphous. b) The DSC thermogram of aromatic polyurea exhibits no crystallization and no melting transitions during the second heating cycle. Only in the first heating curve, an endothermal peak is observed. For the aliphatic polyurea nanocapsules, melting and crystallization peaks are observed.

With increasing Gadobutrol concentration from 10 to 100 mM, the crystallization process observed in the DSC thermograms shifted from the cooling cycle (Figure 27b) to the second heating cycle (Figure 26).

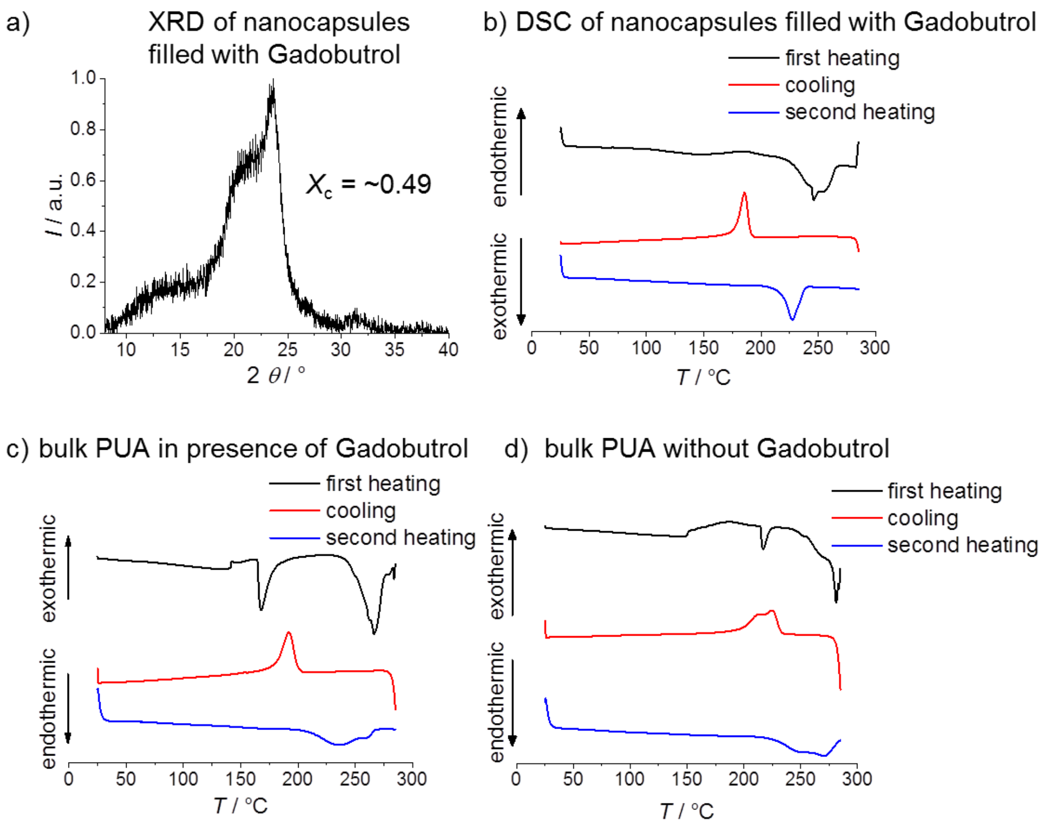

Figure 27: Crystallinity of aliphatic polyurea nanocapsules filled with Gadobutrol (10 mM Gadobutrol as an initial concentration. a) XRD pattern shows similar reflexes as already observed. The relative degree of crystallinity calculated by comparing the area under the reflex to the total area was calculated to be $X_c = \sim 0.49$. b) DSC thermogram. The crystallization point is appearing during the cooling cycle at 186 °C. The sample is melting at 246 °C (first heating curve) and at 227 °C (second heating curve). With 100 mM initial Gadobutrol concentration, cold crystallization occurred and the crystallization peak was shifted to the second heating cycle (see Figure 26b). c) DSC thermogram of polyurea (PUA) made of DAB and HMDI synthesized in bulk in presence of Gadobutrol. d) DSC thermogram of polyurea made of DAB and HMDI synthesized in bulk without Gadobutrol. The presence of Gadobutrol changes the thermal behavior of the resulting polymer.

XRD patterns indicate a similar degree of crystallinity for aliphatic polyurea based nanocapsules filled with 10 and 100 mM initial concentration of Gadobutrol (Figure 26a and Figure 27a). The shift of the crystallization signal from the cooling curve to the second heating curve could be attributed to the influence of Gadobutrol on the thermal properties of polyurea, since mixing of polymers with other substances is reported to result in retarding or accelerating the crystallization process.[171-173] The presence or absence of Gadobutrol influences the thermal behavior of the aliphatic polyurea synthesized in bulk from the monomers 1,4-diaminobutane (DAB) and hexamethylene-1,6-diisocyanate (HMDI) as observed by DSC (Figure 27c and d). The melting temperatures in the first and in the second heating curve as well as the crystallization temperature in the cooling curve of polyurea synthesized in bulk are shifted about 20–30 °C to lower temperatures in presence of Gadobutrol.

4.2.4.2. Relaxivity and Distribution of Gadobutrol in the Nanocapsules

By encapsulating Gadobutrol in nanocontainers of aliphatic polyurea, the relaxivity r_1 increased about 10 times (from ~4 $s^{-1}mmol^{-1}L$ for the non-encapsulated contrast agent up to ~40 $s^{-1}mmol^{-1}L$ (Figure 30a). Such an increase in relaxivity for polymeric nanocontainers was only reported so far if sucrose was co-encapsulated in addition to the contrast agent leading to an increase of the local viscosity.[9] Here we report on the increase in relaxivity without the need for co-encapsulation of sucrose. The highest relaxivity of ~40 $s^{-1}mmol^{-1}L$ was observed for the nanocapsules filled with ~4 mM Gadobutrol, which is a Gadobutrol concentration we expect to exhibit a similar viscosity as pure water. The relaxivity as well as the encapsulation efficiency strongly depend on the initial concentration of Gadobutrol used for the synthesis of the nanocapsules.[9] In a next set of experiments, the initial Gadobutrol concentration was varied from 5 mM to 1 M to find the best combination of relaxivity and local Gadobutrol concentration. The size distribution from DLS measurements and solid contents are reported in Table 2, the SEM and TEM micrographs in Figure 28.

Table 2: Characteristics of the polyurea nanocapsules: Monomers used for the synthesis, initial concentration of encapsulated Gadobutrol, sizes of the nanocapsules in cyclohexane determined by DLS, with X^2 and size distribution given as PDI, solid contents and standard deviations of the nanocapsules dispersion in cyclohexane and water.

c_{Gd} / mM	DLS					solid content	
	d_h /nm	X^2	PDI	$d_{h,1}$ / nm	$d_{h,2}$ / nm	cyclohexane /%	H_2O /%
aliphatic polyurea (DAB+HMDI)							
5	400	0.34	0.21			4.3 ± 0.05	0.53 ± 0.01
5	410	3.15	0.16			4.20 ± 0.04	0.54 ± 0.08
10	390	0.26	0.14			4.34 ± 0.07	0.67 ± 0.05
10	360	0.39	0.04			3.61 ± 0.08	0.41 ± 0.07
100	340	0.81	0.12			4.98 ± 0.09	0.74 ± 0.07
100	380	0.34	0.08			4.99 ± 0.03	0.72 ± 0.03
1,000		11.34		100(12.4%)	360 (87.6%)	11.89 ± 0.06	1.0 ± 0.1
1,000	280	3.15	0.28			10.42 ± 0.04	0.94 ± 0.05
aromatic polyurea (DAB+TDI)							
100	>1 µm			>1 µm		5.22 ± 0.08	0.91 ± 0.07
100	>1 µm			>1 µm		4.49 ± 0.01	0.95 ± 0.06

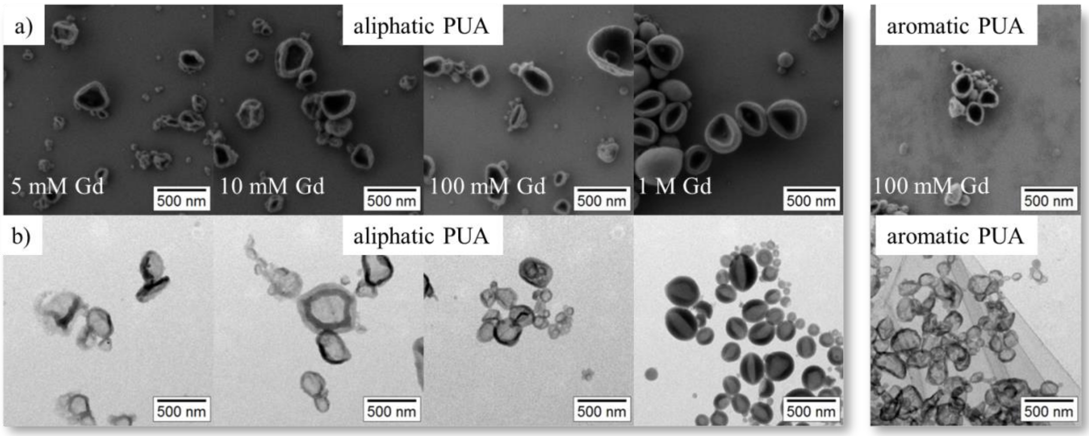

Figure 28: a) SEM and b) TEM micrographs of polyurea nanocapsules. The initial Gadobutrol concentrations are written in white. The nanocapsules filled with 1 M Gadobutrol solution did not collapse completely.

Here we observe a strong dependence of the relaxivity on the concentration of the encapsulated contrast agent (Figure 30a). Decreasing the amount of encapsulated contrast agent from the maximum concentration of 0.2 M to the minimum concentration of 4 mM Gadobutrol solution inside the nanocarriers led to an increase of the relaxivity from ~22 to ~40 $s^{-1}mmol^{-1}L$. As the relaxivity of a contrast agent is usually independent of its concentration, this trend is an intrinsic effect of the confinement in nanocapsules and was observed before for polyurea nanocapsules,[9] for nanozeolites[174] as well as for silica nanoparticles.[42,156] It can be attributed to a saturation effect. The diffusion of the water molecules between the aqueous core of the nanocapsules and the surrounding water outside the nanocapsules is hindered by the nanocapsule shell. The water protons inside the nanocapsule are exposed to the paramagnetic effect of the gadolinium centers. With increasing Gadobutrol concentration, saturation is observed (note that at 4 mM there are about 14000 water molecules per 1 Gd complex, whereas 0.2 M there are only 278 water molecules per Gd complex). Therefore additional Gadobutrol is reducing the average relaxivity. For an initial concentration of Gadobutrol as high as 1 M, a remarkable increase in relaxivity upon encapsulation was observed (from ~4 $s^{-1}mmol^{-1}L$ to ~22 $s^{-1}mmol^{-1}L$). This generates a powerful contrast agent for MRI, as it combines high local contrast agent concentrations (~0.20 M Gadobutrol inside the nanocapsules) with outstanding relaxivity (~22 $s^{-1}mmol^{-1}L$ for r_1).

The successful encapsulation of the contrast agent was further analyzed by element-specific analyses by TEM based energy dissipative X-ray (EDX) spectroscopy on the nanocapsules (Figure 29) and an elemental mapping via energy filtered spectrum imaging (Figure 30b).

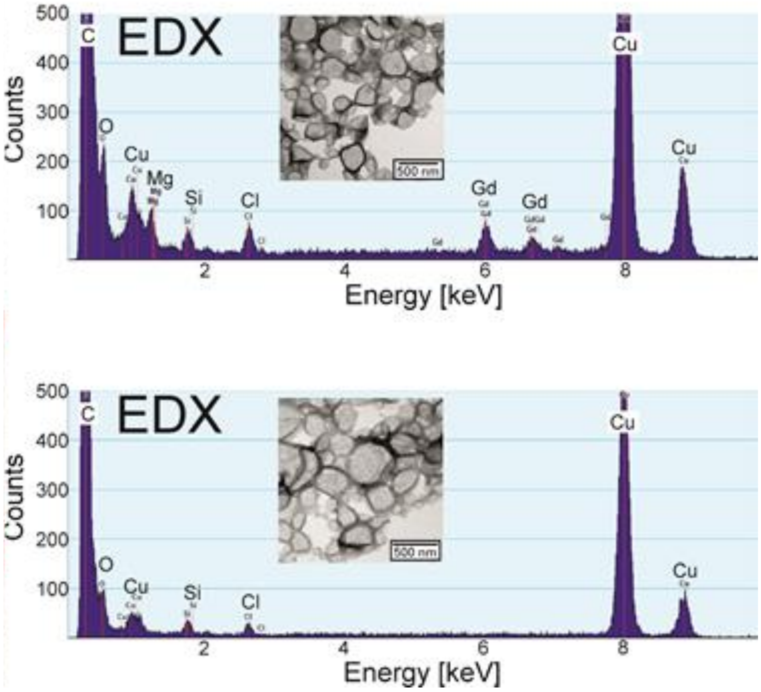

Figure 29: Energy dispersive X-ray spectroscopy (EDX) analyzed on nanocapsules containing gadolinium (top), measured by Dr. Patricia Renz. The characteristic peaks for gadolinium appear in the X-ray spectrum. When no Gadobutrol was encapsulated in the control sample, no signal was observed (bottom).

The element gadolinium was localized within the nanocapsules. Furthermore, an inhomogeneous distribution inside the nanocapsules was observed. The gadolinium was rather located at the nanocapsule shell than inside of the nanocapsules (Figure 30b). The incorporation in the nanocapsule shell could mean an immobilization of the gadolinium complexes, which would slow down its rotation. In turn, the rotational correlation time is related to the relaxivity [34]. Thus, the observed increase in relaxivity could be attributed to the (partial) incorporation of Gadobutrol into the nanocapsule shell.

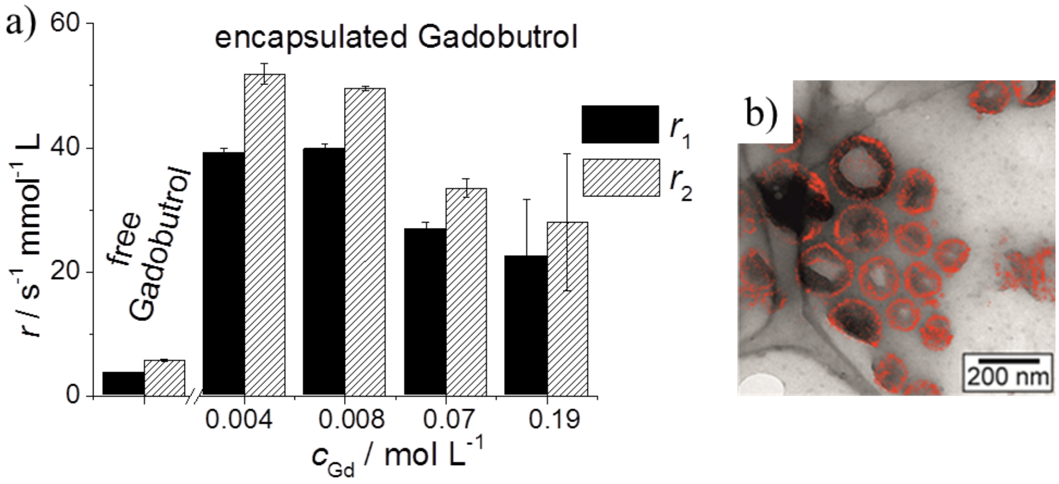

Figure 30: Polyurea nanocapsules filled with the contrast agent Gadobutrol. a) Relaxivity r_1 and r_2 of encapsulated Gadobutrol (right) and non-encapsulated Gadobutrol (left). The x-axis gives the concentration of Gadobutrol inside the nanocapsules, calculated from the initial concentration multiplied by the encapsulation efficiency. b) TEM micrograph of the capsules with an overlay of the gadolinium distribution (in red) mapped by energy filtered spectrum imaging, measured by Dr. Patricia Renz. Gadolinium is found to be mainly located in the nanocapsules shell rather than in the core.

4.2.4.3. Interactions of the nanocapsules with proteins

Once nanomaterials are introduced in biological fluids such as blood or serum components for *in vitro* testing, proteins rapidly adsorb on their surface, creating a protein corona, and hence altering their physicochemical properties. This, in turn, strongly affects their biological fate *in vitro* and *in vivo.* Fetal bovine serum (FBS) is a common protein source supplemented to cell culture medium. Here, we exploited the inevitable effect of protein corona formation by adding low amounts of FBS (2%) in order to stabilize nanocapsule dispersions as we have previously investigated the stabilization effect of a preformed protein corona.[175] In a detailed proteomic analysis, we identified the proteins that adsorbed on the nanocapsules and contributed to the stabilizing effect (Figure 31B). Nanocapsules were surrounded by an outer protein layer consisting of loosely bound proteins that are rapidly exchanged, the so-called soft corona. Below this layer, tightly bound proteins are adsorbed on the nanomaterial (hard corona). Protein corona analysis was performed as previously reported.[164,165] Briefly, after the first centrifugation, the supernatant containing unbound and loosely bound proteins *(S1)* was separated and the nanocapsules pellet was further washed three times to isolate nanocapsules surrounded by tightly bound proteins. Finally, in order to identify the hard corona proteins, the nanocapsules were redispersed with SDS to release the bound proteins. Serum albumin is the most abundant protein in serum (~45%) and was found in large amount in the supernatant after the first centrifugation as indicated by SDS-PAGE (molecular weight ~ 62 kDa) (Figure 31A). LC-MS analysis gave an insight in the composition of the protein pattern of the hard corona. It should be noted that the identity and composition of the protein corona strongly depends on the protein source (FBS vs. human serum).[176] High amounts of α-2-HS-glycoprotein, serum albumin, α-1-antiproteinase, and serotransferrin were found to cover the nanocapsules surface. This is important as albumin is supposed to be a protein that will enhance and prolong the circulation time of the nanocarriers.[177] α-2-HS-glycoprotein and serum albumin belong to the protein class of fetuins. Their major biological function is the transport of various substances in blood.[178] The detailed list of all identified proteins is shown in Table 3.

Table 3: List of all identified proteins in the protein corona (NC), supernatant (SI) and fetal bovine serum (FBS), analyzed by Johanna Simon. The relative amount (%) based on all identified proteins was calculated.

Entry	Description	FBS	NC	S1
P63258;P60712	**Actin. cytoplasmic 2**	0.11	0.07	0.20
Q3Y5Z3	**Adiponectin**	0.12	0.16	0.02
Q3SZR3	**Alpha-1-acid glycoprotein**	0.89	0.14	1.71
P34955	***Alpha-1-antiproteinase***	8.67	10.08	0.85
Q2KJF1	***Alpha-1B-glycoprotein***	0.45	0.66	0.02
P28800	**Alpha-2-antiplasmin**	0.15	0.20	0.01
P12763	***Alpha-2-HS-glycoprotein***	19.33	26.67	0.42
Q7SIH1	**Alpha-2-macroglobulin**	1.41	0.65	0.46
Q3SZ57	**Alpha-fetoprotein**	0.74	0.77	0.16
P41361	**Antithrombin-III**	0.14	0.14	0.07
P15497	**Apolipoprotein A-I**	1.89	1.37	1.63
Q5E9L4	**Apoptosis facilitator protein**	1.89	1.64	3.20
P17690	**Beta-2-glycoprotein 1**	0.23	0.35	0.07
Q2UVX4	**Complement C3**	0.46	0.41	0.13
P01030	**Complement C4 (Fragments)**	0.06	0.04	0.06
P81187	**Complement factor B**	0.10	0.07	0.01
P50448	**Factor XIIa inhibitor**	0.06	0.22	0.01
Q58D62	***Fetuin-B***	1.44	2.32	0.02
Q3SX14	**Gelsolin**	0.05	0.07	0.01
Q28115	**Glial fibrillary acidic protein**	0.03	0.04	0.01
P02081;P02070	**Hemoglobin fetal subunit beta**	0.24	0.62	0.05
Q3SZV7	**Hemopexin**	0.40	0.39	0.15
P56652	**Inter-alpha-trypsin inhibitor H3**	0.10	0.13	0.02
Q3T052	**Inter-alpha-trypsin inhibitor H4**	0.39	0.43	0.06
A1L595	**Keratin. type I cytoskeletal 17**	0.03	0.13	0.03
Q5XQN5	**Keratin. type II cytoskeletal 5**	0.02	0.06	0.03
A0JND2	**Keratin. type II cytoskeletal 80**	1.05	0.84	1.40
P01044	**Kininogen-1**	0.43	0.43	0.21
P01045	**Kininogen-2**	0.16	0.18	0.09
P24627	**Lactotransferrin**	2.74	1.53	2.67
Q2YDF2	**Mediator of RNA polymerase II**	0.02	0.07	0.01
Q58CQ9	**Pantetheinase**	0.04	0.05	0.24
Q95121	**Pigment epithelium-derived factor**	0.13	0.17	0.14
Q9N2I2	**Plasma serine protease inhibitor**	0.04	0.03	0.01
P06868	**Plasminogen**	0.34	0.48	1.43
P00978	**Protein AMBP**	0.37	0.44	0.34
Q2KIT0	**Protein HP-20 homolog**	0.03	0.04	0.01
P00735	**Prothrombin**	0.10	0.09	0.23
Q2KJ39	**Reticulocalbin-3**	0.03	0.03	0.02
Q29443	***Serotransferrin***	6.23	7.91	0.26
A2I7M9;Q9TTE1	**Serpin A3-2**	0.41	0.60	0.01
A2I7N1;A2I7N2	**Serpin A3-5**	0.09	0.10	0.04
A2I7N3	**Serpin A3-7**	0.11	0.12	0.00
A6QPQ2	**Serpin A3-8**	0.01	0.00	0.01
P02769	***Serum albumin***	46.37	36.77	83.17
Q9TT36	**Thyroxine-binding globulin**	0.07	0.09	0.01
O46375	**Transthyretin**	0.23	0.57	0.18
Q3MHN5	**Vitamin D-binding protein**	1.61	1.64	0.06

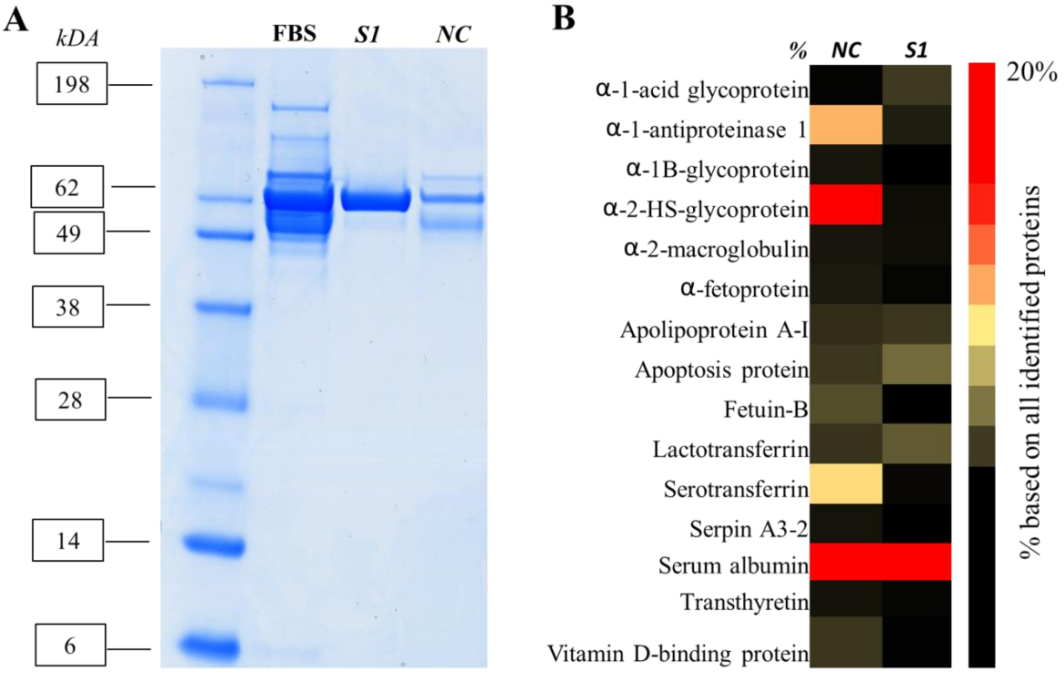

Figure 31: Identification of tightly bound proteins adsorbed on nanocapsules. Experiments were performed by Johanna Simon. **A.** SDS PAGE: Nanocapsules were centrifuged and washed three times with PBS to remove loosely bound proteins. After the last washing step, proteins were desorbed from the nanocapsules *(NC)* using 2% SDS and analyzed by SDS-PAGE. The supernatant after the first centrifugation step *(S1)* and fetal bovine serum *(FBS)* served as comparison. **B.** Heat map: Proteins were digested in-solution and analyzed by liquid chromatography mass spectrometry (LC-MS). Based on all identified proteins the relative amount of each protein is calculated (in %) and the most abundant proteins (> 0.5%) are presented.

4.2.4.4. Localization of the nanocapsules *in vitro* after cell uptake

In vitro studies were performed for nanocapsules containing Gadobutrol and the fluorescent dye Cy5-oligo. The uptake of fluorescently labeled nanocapsules in mesenchymal stem cells (MSCs) and in dendritic cells (DCs) was visualized by cLSM (Figure 32). After the cells have taken up nanocapsules, the cytotoxicity of the nanocapsules was investigated by staining the cells with propidium iodide (PI) followed by flow cytometry analysis. Nanocapsules with different concentrations showed a very low rate of dead cells. The cell viability was higher than 97% for MSCs and 93% for dendritic cells (Figure 32 A). Thus, the encapsulated Gadobutrol did not have a significant effect on the viability of the cells, even at high concentration of contrast agent.

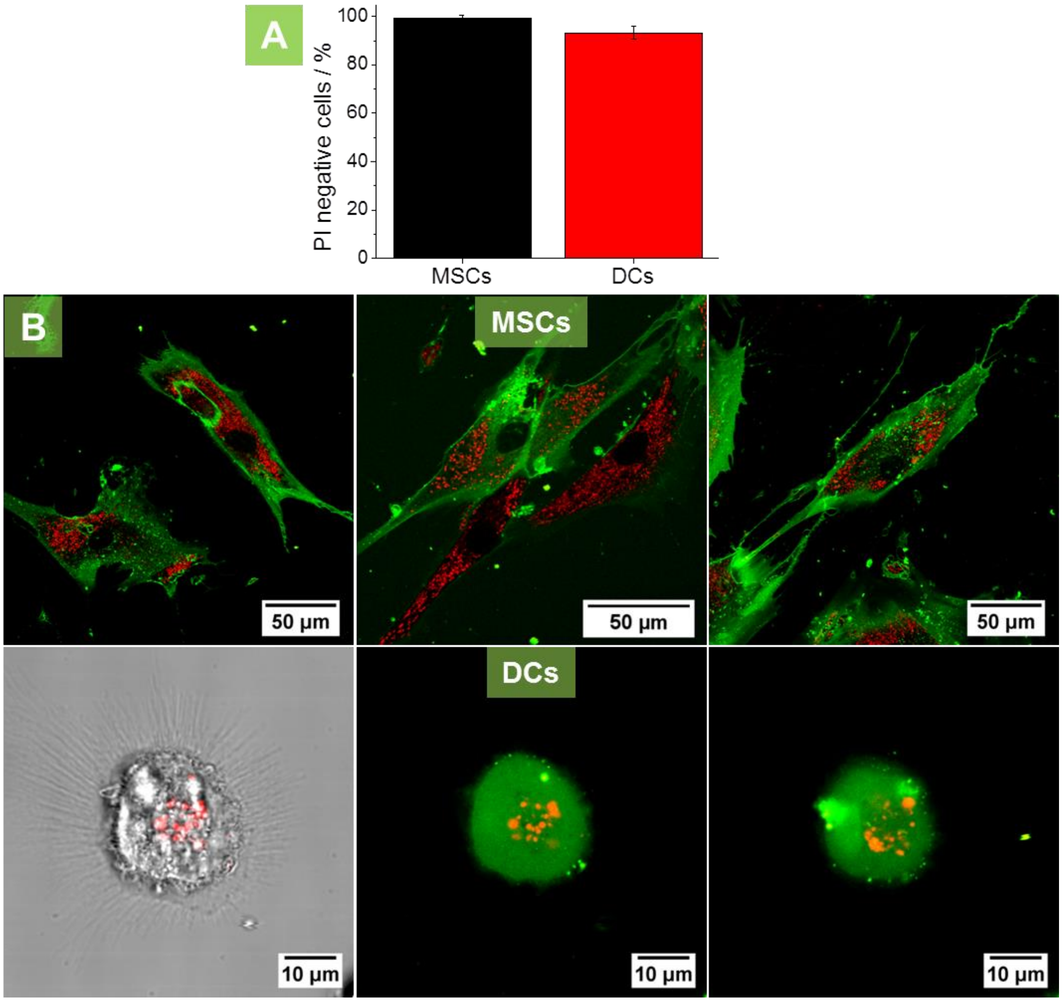

Figure 32: Uptake of the nanocapsules in cells, analyzed by Dr. Patricia Renz. A) The cell viability was measured by propidium iodide (PI) staining and subsequent flow cytometry. The PI-negative MSC and DC cells with incorporated polyurea nanocapsules indicate that the cell viability is as high as 97% and 93%, respectively. The dead cells were excluded from analysis by PI staining (2 µg·mL^{-1}). B) cLSM micrographs of the uptake morphology of polyurea nanocapsules into MSC (upper row of micrographs) and DCs (bottom row of micrographs). The cell membrane is displayed in green, the nanocapsules are displayed in red.

Whereas fluorescence labeling gives an insight in the localization of the nanocapsules in cells, it does not necessarily mean that the gadolinium complex is co-localized with the nanocapsules. Indeed, unwanted leaching of the metal complex may occur into the biological fluid. Therefore, we carried out element-specific analyses by TEM based energy dissipative X-ray (EDX) spectroscopy on the nanocapsules inside dendritic cells (Figure 33). The nanocapsules were identified remarkably well as being clustered in the dendritic cells by transmission electron microscopy as shown in Figure 33. Along the red line displayed in Figure 33, EDX spectra were recorded and the EDX gadolinium signal was found the strongest at the position of the nanocapsules shells. This indicates that the majority of the contrast agent is located in or near the wall of the nanocapsules shell, as already found for pure nanocapsules (Figure 30b). Furthermore, it confirms that the contrast agent is present in the cells and not leaking out of the nanocapsules. This feature is important because it allows for keeping a very high local concentration of gadolinium in the nanocapsules.

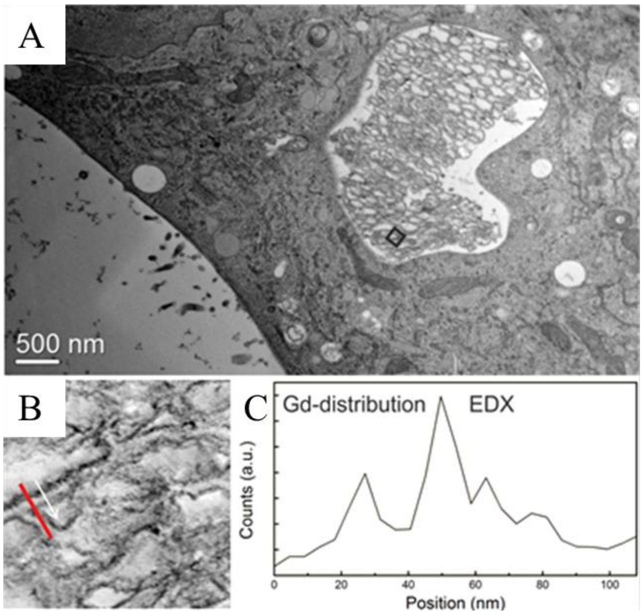

Figure 33: Visualization of the polyurea nanocapsules in dendritic cells and detection of gadolinium within the nanocapsules shell. **A)** The TEM micrograph shows a large cluster of polyurea nanocapsules inside a dendritic cell. The capsules are contained in large intracellular vesicles. **B)** The area marked by the black square in A) is examined by scanning TEM (STEM) with parallel EDX analysis showing the deformed capsules shell in dark contrast. Along the red line an EDX line profile was taken and the EDX gadolinium signal was recorded. C) The gadolinium distribution is correlated to the dark contrast of the STEM micrograph. This indicates that the gadolinium is distributed inside the nanocapsule shell**.**

4.2.4.5. Biodistribution of the nanocapsules and *in vivo* contrast enhancement

The contrast enhancing effect and the biodistribution of the nanocapsules prepared from DAB and HMDI loaded with the contrast agent was tested *in vivo* in mice. As a control experiment, non-encapsulated contrast agent with the same concentration was also tested. An enhancement of contrast could be clearly demonstrated by magnetic resonance images. The spleen was easily detected as dark area present in the highlighted squares in Figure 34 before injection.

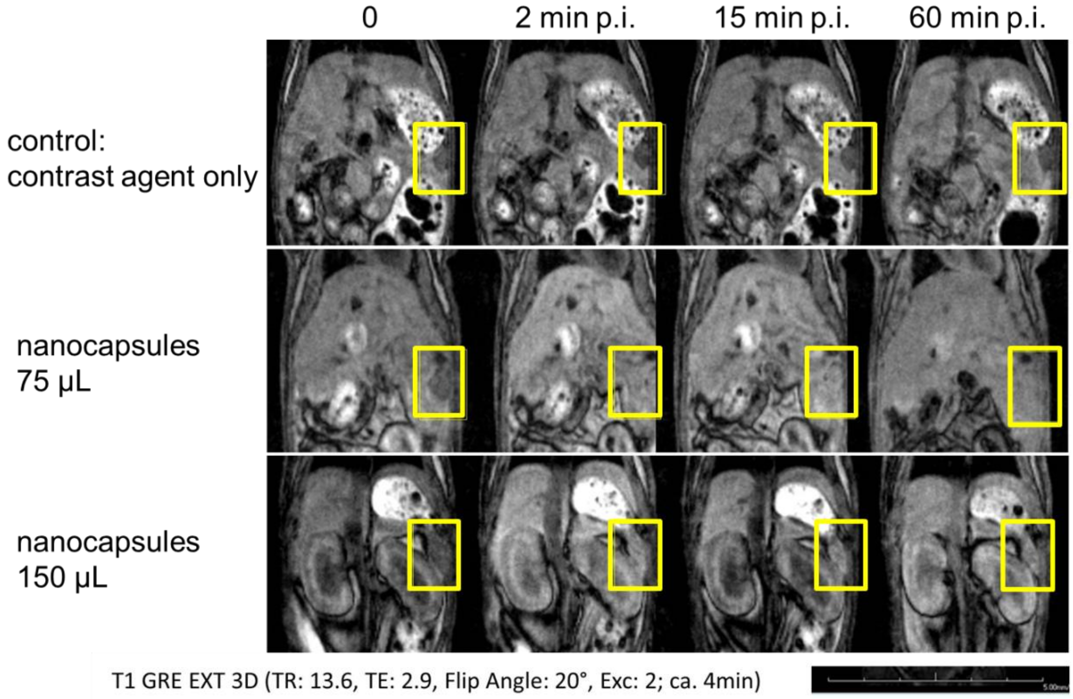

Figure 34: MRI images of mice treated with nanocapsules containing Gadobutrol and with free Gadobutrol as control. The non-encapsulated Gadobutrol was excreted very fast after the injection via the kidneys in the urine (not shown). The effect of the nanocapsules was best observed in the spleen (yellow rectangle). The spleen is enlightened after the application of the nanoparticles. The liver appears also brighter, especially in the first 20 min *p.i.* The effect was stronger when the volume of nanocapsules dispersion was increased from 75 to 150 µL, containing 186 nmol Gadobutrol in total, instead of 93 nmol Gadobutrol.

In the presence of non-encapsulated Gadobutrol, the spleen could still be identified as dark area. On the contrary, the spleen became significantly brighter when the nanocapsules were injected because of their accumulation in this organ. Also the liver appeared brighter after the injection of nanocapsules. In the liver, this effect became more visible when 150 µL of nanocapsule dispersion, containing 186 nmol Gadobutrol, were injected.

After MRI measurements, the mice were sacrificed. Their organs were removed and analyzed by ICP-OES after digestion to determine their gadolinium content. The *ex vivo* biodistribution is shown in Figure 35.

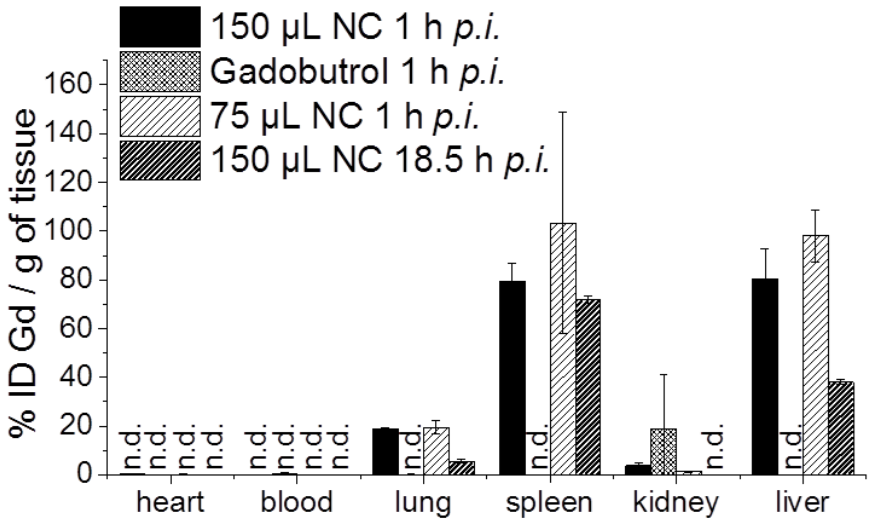

Figure 35: Biodistribution of gadolinium (as Gadobutrol) in mice determined by ICP-OES. Values are expressed as means and standard deviations of % injected dose per gram tissue (n.d. = not detectable). A higher (150 µL, 186 nmol Gadobutrol, three mice) and a lower amount (93 nmol Gadobutrol in 75 µL nanocapsule dispersion, three mice) of nanocapsules dispersion (NC) were injected to find out the optimum amount needed for a sufficient contrast enhancing effect. For the mice treated with nanocapsules, the Gadobutrol was mainly found to be in the liver and in the spleen. The non-encapsulated contrast agent (186 nmol Gadobutrol in 150 µL nanocapsule dispersion, three mice) was only found to be in the kidneys after 1 h. 18.5 h *p.i.* (186 nmol Gadobutrol in 150 µL nanocapsule dispersion, one mouse) only ~55% of the injected dose was found, indicating a partial excretion of contrast agent. Clinically, there were no signs of acute toxicity.

The gadolinium from nanocapsules was mainly found in the liver and in the spleen. Liver and spleen are typical targets for nanoparticles that are taken up by macrophages, as it is expected for nanoparticles larger 200 nm in diameter without further surface modification or targeting.[9,45] In MRI, the contrast enhancing effect in the spleen was easier to observe than in the liver though ICP-OES measurements revealed that a similar amount of gadolinium per g tissue also accumulated in the liver. As the spleen is appearing dark in the magnetic resonance images without contrast agent, it is easy to observe a difference in the brightness. The discrepancy to the *in vivo* MRI imaging with more significant contrast within the spleen as compared to the liver might be explained either by saturation effects, by differences in distributions within the tissue and within the intracellular compartments, or by a dilution effect since the liver is much bigger than the spleen. In the lung, ~20% ID per g tissue were found. For the non-encapsulated contrast agent only (7 ± 8)% of the injected dose in total was found in the mice, mainly in the kidneys, as the rest was already excreted in the urine (observed in MRI, not determined *ex vivo*). The excretion via the kidneys in urine is known for Gadobutrol.[47] 18.5 h *p.i.* the amount of gadolinium in the liver decreased from 80 ± 10 %ID / g tissue to 38 ± 1 % ID / g tissue. The decrease is indicating a partial excretion of the encapsulated Gadobutrol. In none of the experiments, a significant amount of Gadobutrol was found in the blood nor in the heart. Thus, the circulation time in blood is shorter than 1 h for all measured samples. The amount of injected dose of nanocapsules did not show any significant difference in the *ex vivo* biodistribution.

4.2.5. Conclusions

We designed nanocapsules with a remarkably high loading of Gadobutrol as contrast agent. The measured relaxivity was as high as ~40 $s^{-1}mmol^{-1}L$. With the nanocapsules a locally high concentration of the contrast agent could be clearly achieved and identified in cells by electron microscopy and energy dissipative X-ray spectroscopy. The contrast agent was co-localized with the nanocapsules, meaning that unwanted leaching of the contrast agent from the nanocapsules did not significantly occur. The nanocapsules were injected in mice and the biodistribution of the encapsulated contrast agent was found to be different from the biodistribution of non-encapsulated contrast agent. Particularly, the liver and the spleen were highly loaded, allowing for a clear enhancement of contrast in magnetic resonance imaging. Thus, it was possible to enhance tissue contrast compared to free Gadobutrol by efficient encapsulation of Gadobutrol using less Gadobutrol.

4.3. Nanoscale Contrast Agents for Computed Tomography

Computed tomography (CT) contrast agents are suffering from similar drawbacks as contrast agents for MRI. In contrast to MRI, no aqueous surrounding is needed in the direct contrast agent environment. However, higher doses of contrast agents are required for CT. Thus, nanocarriers exhibiting an even higher loading capacity than the nanocapsules introduced in Chapter 4.2 are presented as contrast agents for CT.

4.3.1. Abstract

After the discovery of X-rays, CT became an important imaging tool in medicine. In contrast to other clinical imaging techniques, CT is fast and readily available. A major drawback of CT is the high amount of contrast agent required for the imaging of soft tissue, due to dilution over the whole body and fast depletion over the kidneys. By entrapment of contrast agents into nanocarriers, we aim at reducing the total amount of contrast agent needed for CT imaging.

Herein, we present nanoparticles containing commercial CT contrast agents. The morphology and the hydrophilicity of the nanocarriers were tuned to combine high entrapment efficiency with sufficient colloidal stability. *Via* inverse miniemulsion, iopromide is entrapped into polyurethane nanoparticles with an entrapment efficiency of ~94%. Thus, nanoparticles containing ~25 wt% of iodine were synthesized. Nanoparticle dispersions with an iodine concentration of ~12 ± 3 g/L were obtained.

4.3.2. Introduction

CT is a versatile and non-invasive imaging technique in medicine. Especially for patients that should not be examined by MRI because of metallic implants or cardiac pacemakers,[52] the use of X-rays instead of strong magnetic fields is a good alternative as it is completing the tool box of medical examination.[11]

The use of contrast agents is crucial for CT because soft tissue is only showing a poor absorption of X-rays. Common contrast agents are for example iodine containing molecules. Iodine is absorbing well X-rays and can therefore can enhance the contrast in CT.[3] A good alternative for patients that are hypersensitive to iodine are metal-based CT contrast agents. Additionally, metal-based CT contrast agents are exhibiting favorable X-ray attenuating properties due to their high atomic number, high density, and *k*-edge energy and thus, absorb X-rays stronger than iodine.[53] So far, iodine is the only element approved as CT contrast agent for intravascular administration.[3]

For a good contrast enhancing effect, high doses of the contrast agent are typically required. The need for high amounts of contrast agent is a major disadvantage for CT compared to other imaging techniques such as MRI, PET, and optical imaging methods.[11] Beside toxicity concerns, the high osmotic pressure and the high viscosity caused by high amounts of contrast agent is causing pain in the veins of the patients. Additionally, molecular iodinated contrast agents are excreted rapidly over the kidneys and are therefore limiting imaging times.[3]

The use of nanoparticles offers a possibility to overcome the issue of high osmotic pressure and viscosity.[3] By entrapping the contrast agent inside the nanoparticles, the number of molecules in solution or dispersion and therefore the osmotic pressure experienced by the patient are reduced. The option for targeting in combination with the high local concentration of contrast agent inside the nanoparticles provide another possibility to reduce the required dose of contrast agent.[86] Furthermore, nanomaterials differ from their bulk or molecular equivalents in their pharmacokinetics, biodistribution, and toxicity. Benefits of nanoparticles that are often claimed are accumulation in specific organs or enhanced blood circulation times.[3,179]

Some approaches for nanoscale CT contrast agents are reported in literature.[3,7,179-182] The challenge is to include a maximum amount of contrast agent inside the nanoparticles because the resulting contrast enhancing effect in CT is directly proportional to the amount of the contrast agent. Approaches to develop nanoscale CT contrast agents range from nanoemulsions,[183] micelles,[184] liposomes or polymersomes[185,186] to particulate systems like dendrimers,[187,188] nanocapsules,[189,190] or nanoparticles of inorganic materials or of coordination polymers.[191-193] Pan *et al.* reported of polymeric nanocapsules with a mixture of lipiodol and polysorbate as liquid core resulting in a nanocapsule diameter of ~100 nm and an iodine concentration of 12 mg/mL. Another type of polymeric nanocapsules made of Pluronic and PEG as polymeric shell and lipiodol as core with a diameter of

150 ± 10 nm and an iodine content of ~100 mg iodine/mL was presented by Kong *et al.*[190] DeKrafft *et al.* used $Zn(NO_3)_2$ or $Cu(NO_3)_2$ as precursors to coordinate a molecule containing iodine. The iodinated coordination polymer was forming nanoparticles with a diameter of 200–600 nm with an iodine content of 63 wt%.[191] Ho *et al.* prepared nanocapsules of cross-linked micelles and filled with lipiodol (30−40% w iodine/v) as oily, iodinated core. The dispersions were colloidally stable up to a solid content of 40 wt%.[190] Some iodinated nanoscale CT contrast agents are commercially available. Marval Pharma Ltd. is testing an iodinated CT contrast agent named NCTX™ for blood pool visualization in clinical phase 2 trials. NCTX™ is a PEGylated liposomal iodixanol injection, containing liposomes with a diameter in the range of 100–150 nm and an iodine content of 34.8 mg /mL.[194] A clinical phase I study revealed in 2001 that the administration of high dosage (70 and 100 mg I/kg) of a liposomal iodine contrast agent without a PEGylated surface induced mild and moderate adverse events including back pain, chills, flu-like symptoms, and nausea with vomiting.[195] ExiTron™ nano 6000 and ExiTron™ nano 12000 (nanoPET Pharma GmbH) are commercially available alkaline earth metal-based nanoscale CT contrast agents for visualization of blood pool, liver, and spleen for preclinical CT of small animals such as mice. ExiTron™ nano 6000 contains nanoparticles with a mean hydrodynamic diameter of 110 nm and an iodine content of 160 g / L.[196] Fenestra® VC (MediLumine Inc.) is a nanoemulsion-based CT contrast agent with a droplet size of 100–200 nm, an iodine concentration of 50 g / L, used for preclinical angiography, liver, and spleen imaging of small animals.[197] Due to toxicity issues, the use of Fenestra is still limited to preclinical animal models.[181] However, nanoscale contrast agents for CT encapsulating hydrophilic iodine-containing molecules were not reported so far.

In this chapter, polymeric nanoparticles entrapping hydrophilic iodine-based contrast agents are presented. The inverse miniemulsion used for the synthesis of the nanoparticles offers the possibility of co-encapsulation of other, hydrophilic substances such as drugs. Additionally, the polymeric nanoparticles are decorated with amino groups on their surface available for further surface modifications like targeting. Contrary to systems such as micelles, liposomes, polymersomes or emulsions, nanoparticles are mechanically stable against dilution or agitation, giving the possibility for purification *via* dialysis or centrifugation. Characterization of nanoparticles by electron microscopy is easily accomplished without time consuming sample preparation to conserve the nanoparticles morphology. Different approaches are presented to achieve a high iodine concentration in nanoparticles suspension. As polymeric matrix for the nanocarriers, polyurea has been chosen as versatile and biocompatible material.

4.3.3. Materials and Methods

Chemicals:

Chemicals were purchased as follows: hexamethylene-1,6-diisocyanate (HMDI, ≥99.0%, Sigma Aldrich); toluene-2,4-diisocyanate (TDI, 95%, Sigma Aldrich); cyclohexane (HPLC grade, VWR); dimethyl sulfoxide (DMSO, 99.7+%, Acros Organics); 1,2-diaminoethane (DAE, 99.5%, Carl Roth); 1,4-diaminobutane (DAB, 98+%, Alfa Aesar); sodium dodecyl sulfate (SDS, 99%, Fluka); dimethyl formamide (DMF, 99.9%, Acros Organics), NaCl, deuterated dimethyl sulfoxide (DMSO-d_6), and Hexaiodobenzene (Sigma Aldrich), $CaCl_2$ (Merck); iodide standard used for ICP-OES measurements (from NaI, $c = 1{,}000$ mg L^{-1}, SPEX CertiPrep). The surfactant polyisobutylene-succinimide pentamine was obtained from Lubrizol, France. Iopromide, Ultravist (1.0 M iopromide infusion solution) and Iotrolan were kindly provided by Bayer Healthcare. All chemicals were used as received if not noted otherwise. Milli-Q water (18 MΩ cm) was used for all experiments.

Synthesis of Polyurea Nanocapsules

Ultravist 370 (0.97 M iopromide solution, 370 mg iodine per mL) was diluted with water to the desired concentration. Alternatively, an iopromide solution was used, obtained by dissolving the respective amount of iopromide in water. To the iopromide solution (0.7 mL), NaCl (2 mg) as osmotic pressure agent and 1,4-diaminobutane (50 µL) were added. The aqueous solution was added to a solution of polyisobutylene-succinimide pentamine (50 mg) in cyclohexane (3.75 g). The mixture was stirred for 1 h at 900 rpm at room temperature to obtain a coarse emulsion. A miniemulsion was obtained by sonicating the sample under ice-cooling for 3 min at 70% amplitude with a pulse-pause regime of 20 and 10 s, respectively, using a Branson W450-D sonifier, equipped with a 1/2 in. tip. Under stirring

(900 rpm) the diisocycanate (0.75 mmol) dissolved in cyclohexane (1.25 g) was added dropwise to the miniemulsion. The sample was kept stirring in a closed glass vial (900 rpm, 24 h, at room temperature).

Preparation of Nanoparticles

Nanoparticles were obtained using DMSO or DMF instead of water as solvent for the dispersed phase. If necessary, the iopromide solution was filtrated over Kimtech science tissues (Kimberly-Clark) to remove undissolved residues and the iodine concentration of the dispersed phase was assessed using ICP-OES. Due to the solubility in DMSO, $CaCl_2$ (2 mg) instead of NaCl (2 mg) was added as osmotic pressure agent. No diamine was added. The nanoparticle synthesis was carried out as described before for the nanocapsules synthesis.

Preparation of Nanoparticles with Various Amounts of TDI

A miniemulsion was prepared using 0.5 M iopromide solution in DMF as dispersed phase. After emulsification by sonication, 0.35; 0.44 or 0.75 mmol of TDI were dissolved in cyclohexane (1.25 g) and added dropwise to the miniemulsion.

Preparation of Nanoparticles with Various Amounts of DAE

0.53 or 1.06 mmol of DAE were added to a solution of 0.5 M iopromide and 2 mg $CaCl_2$ in DMSO. The miniemulsion was carried out as described prior in this section for iopromide containing nanocapsules. After sonication, TDI (1.39 mmol) diluted in cyclohexane (1.25 g) was added to the miniemulsion.

Preparation of Nanoparticles Containing Iotrolan

Instead of iopromide, a 0.5 M solution of iotrolan in DMSO (0.7 mL) was used as dispersed phase. The inverse miniemulsion was obtained as described for iopromide nanoparticles prior in this section. After sonication, TDI (1.39 mmol) diluted in cyclohexane (1.25 g) was added to the miniemulsion.

Transfer of Nanoparticles from Cyclohexane into Water

The nanoparticle dispersion was filtrated over Kimtech science tissues (Kimberly-Clark) to remove agglomerates formed during nanoparticle synthesis. The filtrated nanoparticle dispersion in cyclohexane (1 g) was added dropwise and under stirring to 0.3 wt% aqueous SDS solution (5 g). Cyclohexane was evaporated under stirring (900 rpm, 24 h, at room temperature) in a glass vial with an open lid. The nanocapsule dispersions in water were purified in two steps. Firstly, the agglomerates were removed by centrifugation at 500 rpm for 5 min. The supernatant was transferred into a new vial and centrifugation was performed at 4000 rpm for 15 min. The supernatant was removed and the nanocapsules were dispersed in fresh SDS solution. The entrapment efficiency EE_r, giving the fraction of iodine remaining in the nanoparticles in percent, was evaluated by measuring the iodine concentration before purification c_t and in the second supernatant c_S by ICP-OES (eq. 12).

$$EE_\mathrm{r} = 1 - \frac{c_S}{c_t} \tag{12}$$

Transfer into Water with Sonication

The sample was placed in a sonication bath for ~5 min directly after mixing the nanoparticles dispersed in cyclohexane with the aqueous SDS solution. Evaporation of cyclohexane and purification of the nanocapsules in water were performed as described in the last paragraph.

Analytical Tools

The iodine content was determined by inductively coupled plasma-optical emission spectroscopy (ICP-OES, Activa M spectrometer, Horiba Jobin Yvon). A Meinhardt-type nebulizer, a cyclone chamber, and the software ACTIVAnalyst 5.4. were used for the ICP-OES measurements under the following conditions: 1250 W forward plasma power, 12 L min^{-1} Ar flow, and 15 rpm pump flow. As reference line, the Ar emission at 404.442 nm was chosen. Prior to the measurements, the ICP-OES spectrometer was flushed with a nitrogen gas flow for at least 4 h. For calibration and quantification of iodine, the emission lines at 178.214 and 182.976 nm with a 5 s integration time were chosen. A calibration curve was recorded using six different iodine concentrations prepared by dilution of a commercial iodine standard with 0.3 wt% aqueous solution of SDS. The nanoparticle samples were diluted with a 0.3 wt% aqueous solution of SDS to obtain concentrations within the calibration range. The baseline correction and the dynamic underground correction were provided by the software ACTIVAnalyst 5.4. The solid content was assessed gravimetrically by weighing 100 µL of the sample before and after freeze-drying. The hydrodynamic radius and the size distribution of the nanoparticles were measured by dynamic light scattering (DLS) at a PSS Nicomp Particle Sizer 380 at a scattering angle of 90°. Prior to DLS measurements, the dispersions were diluted with the respective solvent. DLS measurements in plasma were performed on an ALV spectrometer consisting of a goniometer and an ALV-5004 multiple-tau full-digital correlator (320 channels), which allows measurements over an angular range from 20° to 150°. A He-Ne Laser operating at a laser wavelength of 632.8 nm was used as light source. For temperature controlled measurements, the light scattering instrument is equipped with a thermostat from Julabo. The polyurea nanoparticles, dispersed in 0.3 wt% SDS with a solid content of (4.9 ± 0.2)% (1 µL), were incubated with human blood plasma (1 mL, citrate plasma, filtrated over membrane filter with a pore size of 0.22 µm (Millex GS syringe filters), prepared according to standard guidelines, obtained from the blood transfusion service at the University Medical Center Mainz) for 1 h at 37 °C. Measurements were performed at 20°C at different angles ranging from 30° to 150°. Scanning electron microscopy (SEM) measurements were performed using a LEO 1530 Gemini (Zeiss) field emission microscope at an extractor voltage of 0.2 kV. Transmission electron microscopy (TEM) micrographs were recorded at a JEOL JEM-1400 electron microscope operating at an acceleration voltage of 120 kV. The samples for SEM and TEM were prepared by drop-casting the diluted nanocapsule dispersion with a solid content of about 0.01 wt% onto a silicon wafer or onto a carbon-coated copper grid, respectively. ^{1}H NMR spectra in DMSO-d_6 were recorded using an Avance III 250 NMR spectrometer (Bruker BioSpin GmbH). The data was acquired using the Topspin 2.1 software (Bruker BioSpin GmbH). As internal standards, the signals of the solvent protons were used. Processing of the NMR spectra was achieved using the MestReNova 11.0.4 software (Mestrelab Research S.L.). Sodium dodecyl sulfate-polyacrylamide gel electrophoresis (SDS-PAGE) was carried out by Johanna Simon. An amount of protein (6 µg) was added to NuPage Reducing agent (4 µL), NuPAGE LDS Sample buffer (10 µL) and loaded onto a NuPage 10% Bis Tris Gel. The gel was run for 1 h at 100 V in NuPAGE MES SDS Running Buffer using SeeBlue Pre-Staining Standard as marker. Protein bands were visualized using Simply Blue safe stain (all Thermo Fisher).

4.3.4. Results and Discussion

This chapter focuses on two main issues: first the entrapment efficiency and second the colloidal stability of the dispersion. For the entrapment of the commercially available iodine-based CT contrast agent iopromide, nanocapsules (as presented in Chapter 4.1 and 4.2) and nanoparticles were tested. The colloidal stability was engineered by addressing the hydrophilicity of the nanoparticle matrix, the size distribution, and the transfer from organic to aqueous medium.

4.3.4.1. Nanocapsules from Ultravist *vs.* Iopromide

The commercially available infusion solution Ultravist contains the CT contrast agent iopromide (molecular structure see Figure 36) at a concentration of ~1 M.

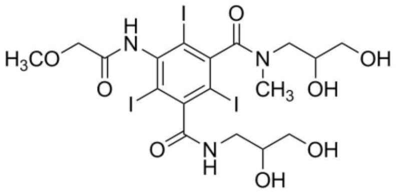

Iopromide (Ultravist)

Figure 36: Molecular structure of iopromide, an FDA approved CT contrast agent.

To obtain nanocapsules, a similar approach was chosen as presented in Chapter 4.2 for the nanocapsules containing Gadobutrol. The infusion solution was diluted with water to the desired concentration and encapsulated into polyurea nanocapsules *via* inverse miniemulsion. For the synthesis of polyurea, the hydrophilic monomer 1,4-diaminobutane (DAB) was added to the aqueous solution of iopromide. The hydrophilic phase was mixed with a solution of surfactant polyisobutylene-succinimide pentamine in cyclohexane and emulsified via sonication. After sonication, the hydrophobic monomer toluene-2,4-diisocyanate (TDI) diluted in cyclohexane was added. The polymerization (Figure 37 A) took place at the water-cyclohexane interface and nanocapsules with a polyurea shell and an aqueous core were obtained. The procedure is similar to the one depicted schematically in Figure 11 in Section 4.1.4.1. After the synthesis, the nanocapsules were transferred into water. To investigate the encapsulation efficiency, the nanocapsule dispersion was purified *via* centrifugation and the iodine content was measured using ICP-OES. The encapsulation efficiency after the re-dispersion in water EE_r was calculated as a ratio of the iodine content in the supernatant and the total iodine content in the nanocapsule dispersion prior to purification (Figure 37 B). The morphology was investigated by SEM, revealing a core-shell structure. The nanocapsules collapsed due to the evaporation of the encapsulated water upon sample preparation achieved by drop casting followed by drying and due to the SEM vacuum conditions (Figure 37 C).

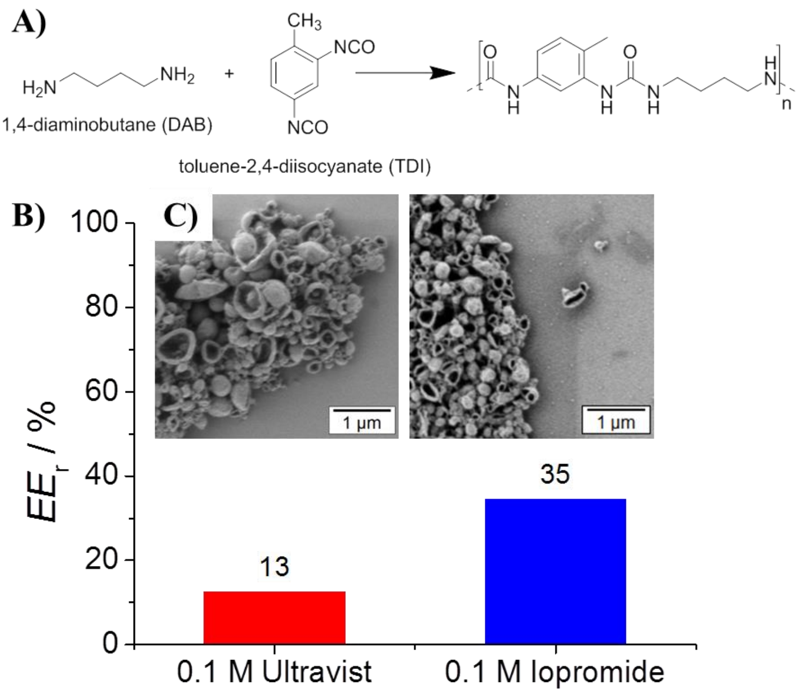

Figure 37: Polyurea nanocapsules filled with an initial concentration of Ultravist or iopromide of 0.1 M. A) Scheme of the polymerization taking place at the droplet interface, forming the polymeric nanocapsules shell. B) Encapsulation efficiencies EE_r and C) SEM micrographs of polyurea nanocapsules filled with Ultravist infusion solution (red, left) and with a solution of iopromide in water (blue, right). Nanocapsule synthesis and SEM of the Ultravist containing nanocapsules were performed by Kerstin Malzahn.

The infusion solution Ultravist does not only contain iopromide. It contains further components such as tris(hydroxymethyl)aminomethane (tromethamine, 2.4 mg/mL) as buffer and calcium disodium edetate (EDTA, 0.1 mg/mL) as sequestering agent (Figure 38).[198]

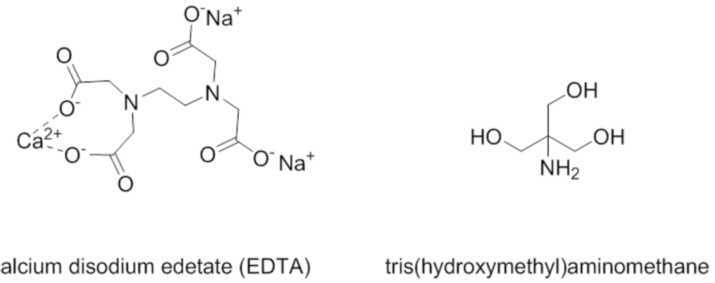

Figure 38: Molecular structures of calcium disodium edetate (EDTA, 2,2',2'',2'''-(1,2-ethanediyldinitrilo)tetrakis acetic acid calcium disodium salt, left) and tris(hydroxymethyl)aminomethane also known as tromethine (right), which can be found in the formulation of Ultravist beside iopromide. Tris(hydroxymethyl)aminomethane is bearing three hydroxylgroups and one amino group which can possibly react with an isocyanate.

While EDTA is not exhibiting any functional groups which could react with isocyanates, tris(hydroxymethyl)aminomethane displays three hydroxyl- and one amino-group that can react with isocyanates. The reaction between the mono-amine tris(hydroxymethyl)aminomethane and the diisocyanate might retard the polymer chain growth during the synthesis, as the reaction rate of the reaction between hydroxyl groups and isocyanates is ~1000 times slower compared to the reaction rate of the reaction between amines and isocyanates.[199] Though EDTA is not taking part in the polymerization, it increases the osmotic pressure inside the nanocapsules and might therefore promote uncontrolled release of the payload. Thus, polyurea nanocapsules filled with a solution obtained by dissolving iopromide in water were synthesized and compared to those filled with Ultravist solution, prepared by Kerstin Malzahn (Figure 37). By encapsulating iopromide solution instead of Ultravist, the iodine retention was increased from ~13% to ~35%. However, the encapsulation efficiency of iopromide solution was with ~35% rather low compared to previous experiments with Gadobutrol (Chapter 4.1 and 4.2). In the next steps, we will try to identify the factors determining the low encapsulation efficiency and to increase the encapsulation efficiency by engineering the nanocapsule shell.

4.3.4.2. Semi-crystalline Nanocapsules to Increase Encapsulation Efficiency

The diffusion of the contrast agent through the nanocapsules shell should be reduced by the use of a semi-crystalline shell material, as shown in Chapter 4.1

Thus, polyurea nanocapsules with an aliphatic polyurea as a shell material were synthesized (Figure 39).

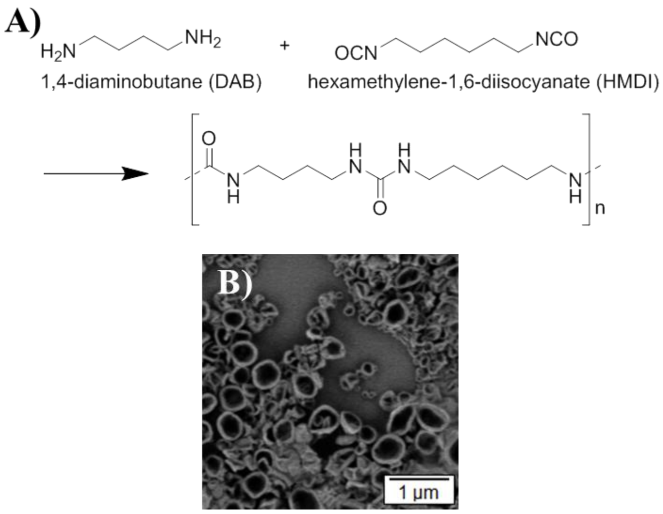

Figure 39: Chemical structure of polyurea (A) and SEM image (B) of polyurea nanocapsules synthesized from DAB polymerized with HMDI and 0.1 M initial iopromide solution in water.

The use of the linear, aliphatic diisocyanate HMDI instead of the angled, aromatic diisocyanate TDI resulted in a polyurea shell with a higher crystallinity degree (see Chapter 4.1). The nanocapsules exhibited a hydrodynamic radius of $d_h = 290$ nm (PDI = 0.17), which is smaller than the hydrodynamic radius of the nanocapsules synthesized with TDI ($d_h = 700$ nm, PDI = 0.24). Although the previous results presented in Chapter 4.1 revealed an enhanced density of the nanocapsules, the retention for iopromide in the nanocapsules was found to be only 2–4%.

Iopromide is bearing four hydroxyl groups and two amides (Figure 36) that could possibly react with isocyanates (Scheme 1).

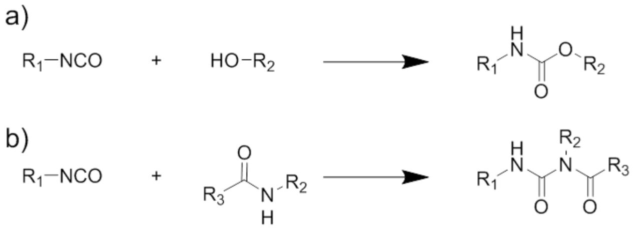

Scheme 1: Reaction between isocyanate and hydroxyl groups (a) and isocyanate and amides.

Amides exhibit a similar reactivity as hydroxyl groups in the reaction with isocyanates.[199] The increased retention of TDI-based nanocapsules could be attributed to a side reaction between iopromide and TDI, resulting in a covalent entrapment of iopromide in the nanocapsules. In contrary to TDI, HMDI is less reactive than TDI. The reaction rate constant for the reaction of TDI and a hydroxyl group is reported to be 2.5 times higher than the reaction rate constant for the reaction of HMDI and a hydroxyl group.[200,201] Reactions between HMDI and hydroxyl groups are rather taking place at higher temperatures (80 °C or higher) and/or in presence of catalysts such as dibutyltin dilaurate.[202] The reaction between an aliphatic isocyanate and a hydroxyl group is reported to reach 100% conversion after 15 min reaction time at a reaction temperature of 60 °C in presence of 0.1 mol equivalent dibutyltin dilaurate. With less catalyst (0.001 instead of 0.1 mol equivalent) the conversion reported to be only 32% after the same reaction time.[203]

4.3.4.3. Is Iopromide Chemically Bond or Physically Entrapped into Nanocapsules?

To monitor whether iopromide is physically entrapped or chemically bond in the nanoparticles, the reaction between iopromide and TDI was followed by ^{1}H-NMR spectroscopy. Iopromide is exhibiting two amide groups and four OH-groups that could possibly react with TDI. A solution of iopromide in deuterated dimethylsulfoxide (DMSO-d_6) was prepared and the NMR spectrum was recorded. TDI was added to the iopromide solution in DMSO-d_6 and the NMR spectrum was recorded 10 min and 17 h after the addition of TDI (Figure 40).

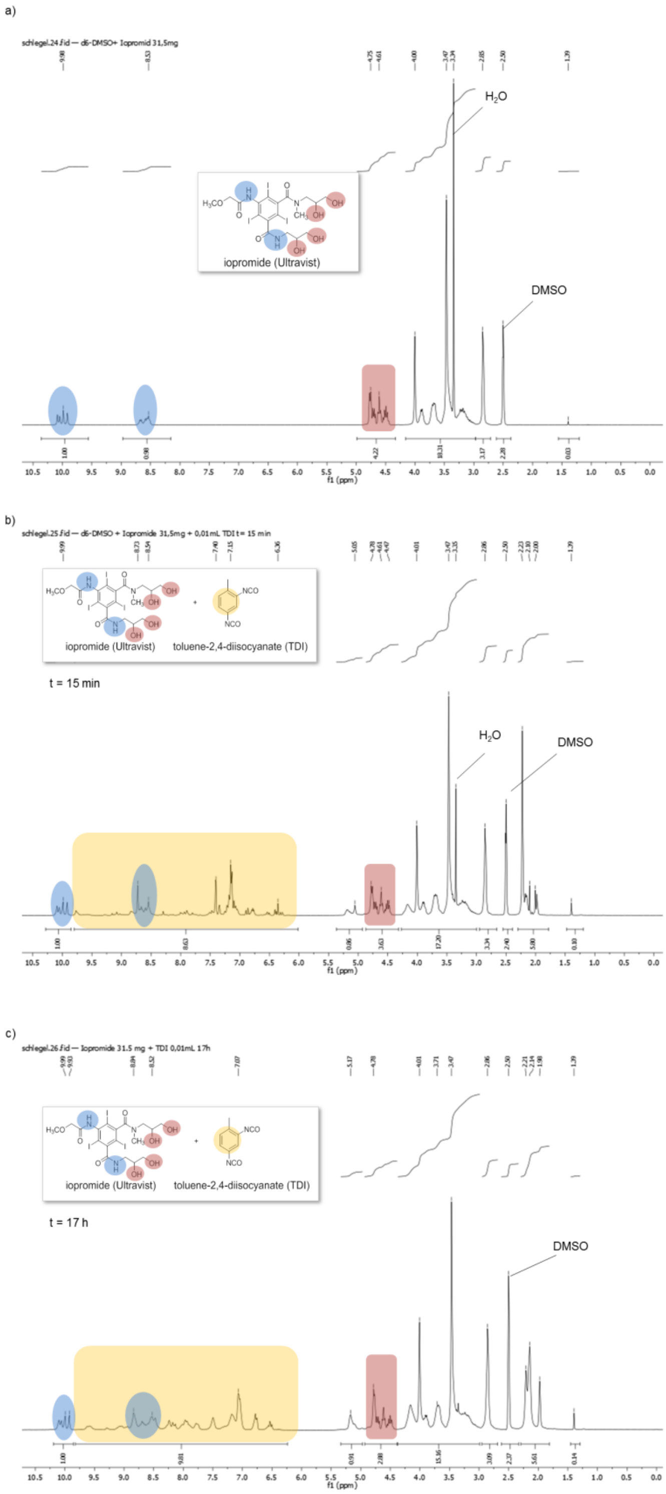

Figure 40: ^{1}H-NMR of iopromide dissolved in deuterated dimethylsulfoxide (DMSO-d$_6$) (a), 15 min (b) and 17 h (c) after the addition of TDI. The relative integral of the hydroxyl protons of iopromide is reduced from 4.22 before TDI addition to 2.88 after 17 h, implementing a reaction of hydroxyl groups with the isocyanate groups of TDI.

The signal of the aromatic protons of TDI was broadening over time and the signal at 3.34 ppm attributed to residual water in DMSO was vanished after 17 h. Thus, TDI was reacting with the residual water contained in DMSO-d_6. The signals referring to the amide and hydroxyl groups of iopromide are partially superimposed with new signals appearing upon TDI addition. The reaction products of isocyanates with water are urea bonds and, with hydroxyl groups, urethane bonds (see Scheme 1), both exhibiting protons next to a nitrogen atom that are observed in the region of 8−10 ppm. For integration, the integral of the NMR signal at 9.98 ppm, corresponding to one amide proton, was set to a value of 1.00 and used as an internal reference. 17 h after the addition of TDI, the relative integral of the hydroxyl protons of iopromide, observed at ~4.8 ppm, is reduced from 4.22 measured before TDI addition, to 2.88, implementing a reaction of hydroxyl groups with the isocyanate groups of TDI. The integrals of other iopromide related signals remained unchanged. This might indicate a reaction between iopromide and TDI. To provide further evidence that a reaction between TDI and iopromide was taking place, complementary measurements such as diffusion ordered spectroscopy (DOSY NMR) or Heteronuclear Multiple Bond Correlation NMR (HMBC-NMR) are required.

4.3.4.4. Iopromide Nanocapsules *vs.* Nanoparticles

Considering that covalent bonds between TDI and iopromide are formed, it could mean that no amine is needed to form nanocapsules or nanoparticles. Accordingly, nanocapsules were prepared without the addition of 1,4-diaminobutane. The dispersed phase contained a solution of iopromide in water. TDI was allowed to react with iopromide. Furthermore, side reactions of TDI with water and as well as with the surfactant might occur.

Without the presence of 1,4-diaminobutane in the dispersed phase, SEM images revealed nanocapsule formation (Figure 41). The absence of diamine enabled the encapsulation of iopromide with a higher initial concentration (0.5 M instead of 0.1 M) at a similar encapsulation efficiency (33% and 35%, respectively), compared to the nanocapsules presented in Section 4.3.4.1. Nevertheless, with 0.5 M initial iopromide concentration, the encapsulation efficiency was still rather low (~33%) for nanocapsules prepared without the addition of 1,4-diaminobutane.

To further increase the encapsulation efficiency, nanoparticles with a solid core instead of nanocapsules were synthesized. In contrary to MRI contrast agents, no aqueous core is required for CT contrast agents. In nanoparticles, the diffusion pathway for the entrapped payload is longer in comparison to nanocapsules, where only a thin shell is acting as obstacle. Crespy et al. described the formation of solid core nanoparticles, when DMSO was used as solvent for the dispersed phase.[117] Accordingly, iopromide was dissolved in DMSO and emulsified in a solution of the surfactant polyisobutylene-succinimide pentamine in cyclohexane. TDI, diluted in cyclohexane, was added after sonication. As TDI is miscible with DMSO, the polymerization is not limited to the droplet interface and nanoparticles are obtained. Conversely, nanocapsules were obtained when water was used as dispersed phase (Figure 41).

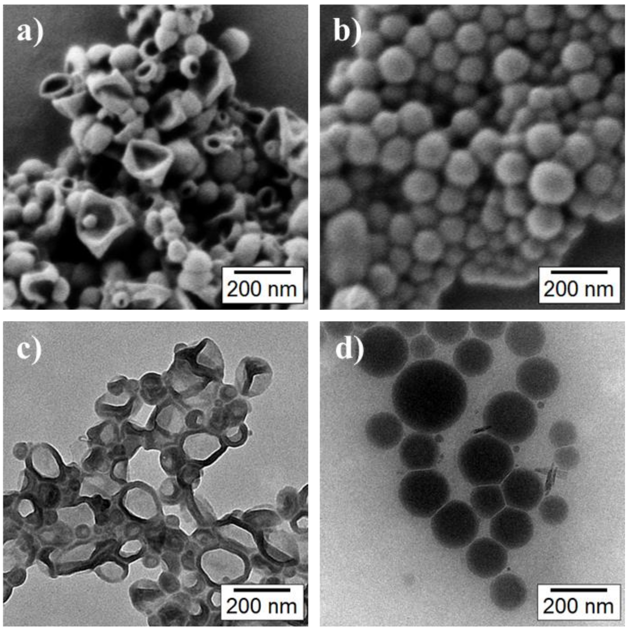

Figure 41: Electron micrographs of nanocapsules (left) and nanoparticles (right). SEM (upper row) and TEM images (lower row) of nanocapsules and nanoparticles, obtained using water or DMSO as dispersed phase, respectively. TEM images were recorded by Alexander Schoth.

By the use of DMSO as dispersed phase, the entrapment efficiency was raised from ~33% obtained for nanocapsules to ~94% for nanoparticles. SEM images revealed a nanoparticle structure with a solid core. No phase separation between DMSO and the formed polymer was visible in the SEM micrographs (Figure 41). As no major phase separation is observable and as DMSO is still present in the nanoparticles, it can be assumed that DMSO was equally distributed in the nanoparticles. DLS measurements revealed a mean hydrodynamic diameter of 310 nm (PDI = 0.39) for the nanoparticles dispersed in cyclohexane.

During the transfer to water, the formation of agglomerates was observed, which resulted in a lower iodine concentration in the nanoparticle dispersion, as the precipitated agglomerates were not available for ICP-OES measurements. Agglomerates were removed in a first centrifugation step at 18 rzb (500 rpm). The supernatant was then removed and centrifuged a second time at 1820 rzb (5000 rpm). The entrapment efficiency was evaluated by ICP-OES measurements from the second supernatant.

Though the entrapment efficiency was found to be ~94%, the iodine concentration was with ~5 mg/mL of iodine after purification far below the expected concentration of ~17 mg/mL. This discrepancy can be explained with the loss of nanoparticles during the first centrifugation step. By increasing the colloidal stability, the iodine concentration in the nanoparticle dispersion is expected to increase. Thus, approaches to increase the colloidal stability will be presented in Section 4.3.4.6 ff.

4.3.4.5. Nanoparticles with Hexaiodobenzene

To investigate whether similar entrapment efficiencies are available for a molecule that cannot undergo a chemical reaction with TDI and is not chemically bond in the nanoparticles, nanoparticles containing hexaiodobenzene, which is bearing no reactive groups towards TDI, were synthesized.

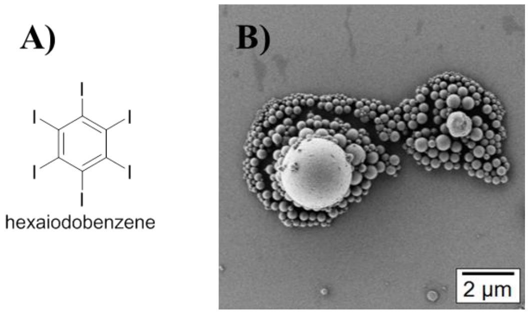

Figure 42: Nanoparticles filled with hexaiodobenzene. A) Chemical structure of hexaiodobenzene. B) SEM micrograph of nanoparticles filled with hexaiodobenzene.

The nanoparticles revealed a mean hydrodynamic diameter of 510 nm (PDI = 0.22) and an entrapment efficiency of (60 ± 10)%. The entrapment efficiency was ~60% for hexaiodobenzene, *i.e.* lower than for iopromide containing nanoparticles (~94%). Consequently, the entrapment in nanoparticles is also possible if no chemical bonds are formed between the matrix and the cargo.

4.3.4.6. Addition of 1,2-Diaminoethane

The iodine content of the nanoparticle dispersion was, so far, limited by the colloidal stability of the dispersion (see Section 4.3.4.4). One method to improve the colloidal stability of nanoparticles in water is to increase the hydrophilicity of the nanoparticle material. The reaction rate of the reaction of isocyanates with primary amines is about 1000 times higher than the reaction rate of the reaction between isocyanates and hydroxyl groups or water.[199] Thus, addition of amines would reduce the amount of side reactions such as TDI with water (Scheme 2).

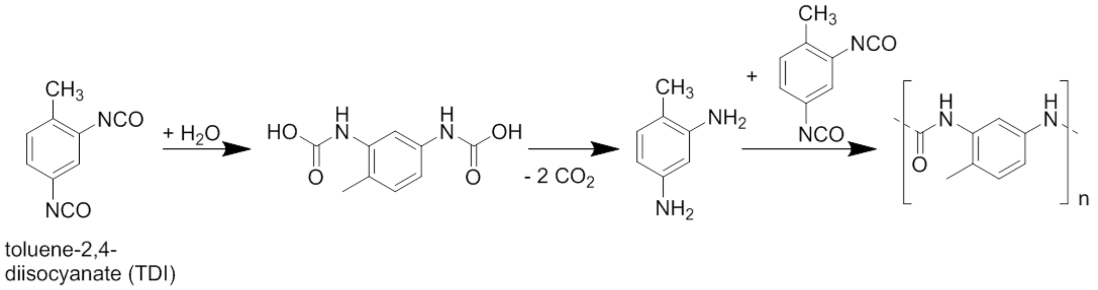

Scheme 2: Polyurea formation by the reaction of TDI with water. The aromatic isocyanate groups react with water and release CO_2 to form the amine. The isocyanate born amines can react with the remaining isocyanate groups to give an aromatic polyurea.

The density of functional groups in a molecule correlates with its hydrophilicity. 1,2-Diaminoethane (DAE) was chosen, as it exhibits two primary amines and two methylene groups (see Figure 43 A) and it is miscible with DMSO. The isocyanate born amine that might be formed due to the side reaction of TDI and water is exhibiting seven carbon hydrogen groups and two amine groups and is accordingly much more hydrophobic than DAE (DAE is miscible with water, the solubility of toluene-2,4-diamine in water is 1-5 mg/mL).[204] To increase the hydrophilic character of the nanoparticles, DAE was added to the dispersed phase of iopromide dissolved in DMSO. The hydrophilic phase was added to the continuous phase consisting of polyisobutylene-succinimide pentamine dissolved in cyclohexane. After sonication and the addition of TDI to the inverse miniemulsion, nanoparticles were obtained. Two different amounts of DAE were tested and compared to nanoparticles synthesized without DAE (Figure 43). [199]

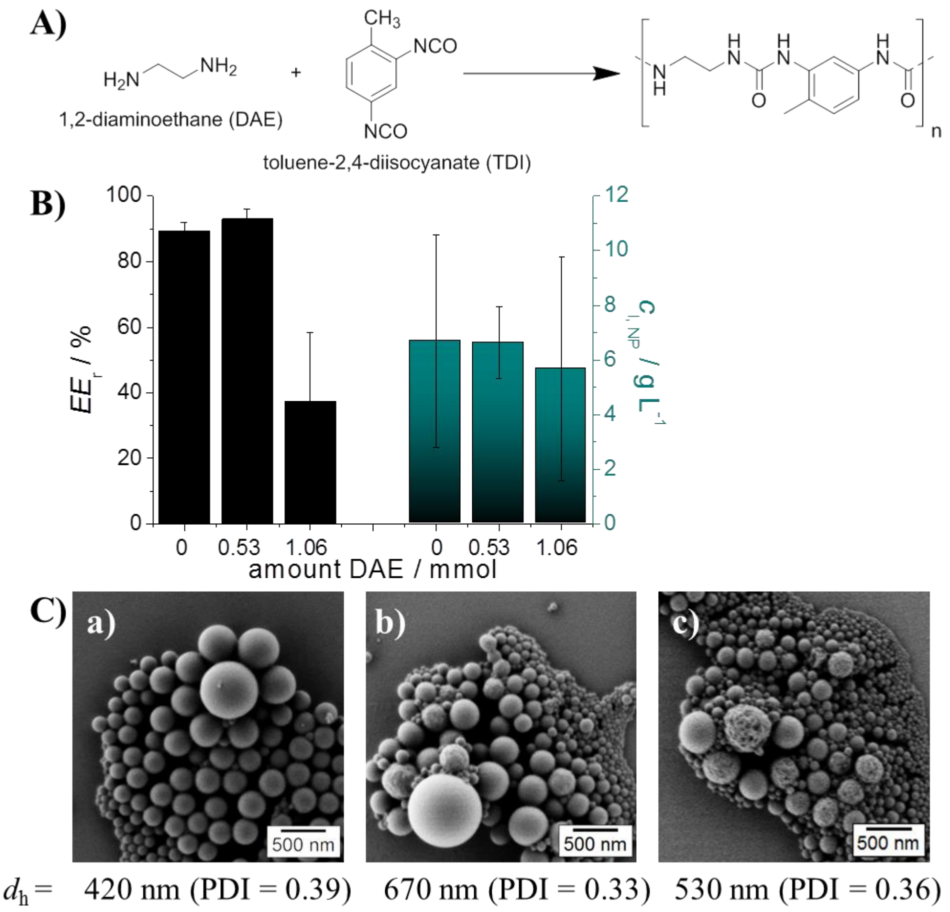

Figure 43: Nanoparticles synthesized from various amounts of 1,2-diaminoethane (DAE) and TDI with DMSO as dispersed phase. A) Scheme for the polyaddition of DAE and TDI. B) Entrapment efficiency EE_r and iodine concentration after purification. The data points were averaged over two samples. Error bars represent standard deviations. C) SEM micrographs and DLS data are revealing nanoparticle formation a) without addition of DAE, b) with addition of 0.53 mmol of DAE per batch (ratio DAE:TDI = 1:2.6), and c) with 1.06 mmol of DAE per batch (ratio DAE:TDI = 1:1.3). Per batch, 1.39 mmol of TDI was used, respectively.

With 0.53 mmol of DAE, the entrapment efficiency was comparable to the entrapment efficiency obtained without DAE. Nevertheless, the resulting iodine concentration remained constant. Upon addition of 1.06 mmol of DAE, the entrapment efficiency decreased from ~90% to ~34%. Due to the higher hydrophilic character of the nanoparticle matrix, diffusion of iopromide through the nanoparticle matrix was promoted. The improved colloidal stability was counterbalanced by a decrease in encapsulation efficiency. In the following part, no DAE was added because no increase in the resulting iodine concentration was achieved by addition of DAE.

4.3.4.7. Iopromide *vs.* Iotrolan

The size of the molecules is playing a key role in their diffusion behavior when they are physically entrapped in a matrix. Iotrolan is a dimer of iopromide, exhibiting roughly a double molecular weight and iodine content while the iodine content per molecular weight for iopromide and iotrolan is comparable. Nanoparticles containing iotrolan were synthesized using iotrolan and compared to nanoparticles containing iopromide with a similar initial iodine concentration (Figure 44).

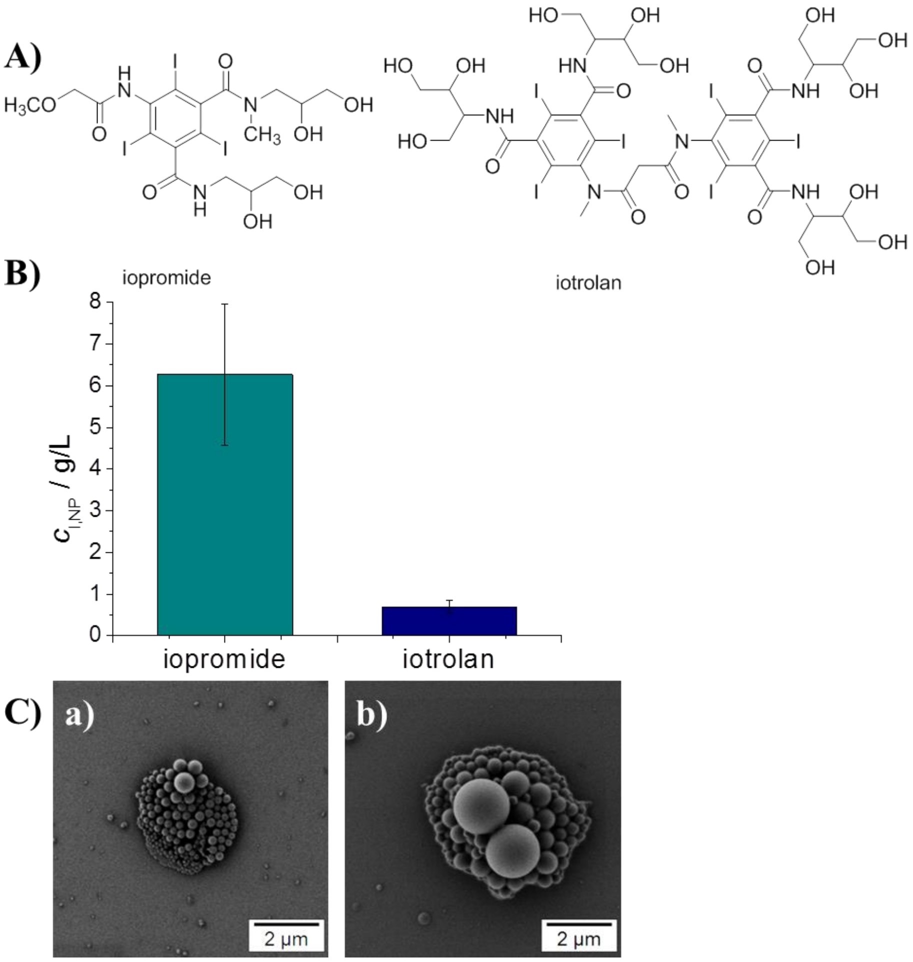

Figure 44: Nanoparticles filled with iopromide (left) or iotrolan (right). A) Chemical structure of iopromide and iotrolan. B) Comparison of resulting iodine concentration in nanoparticle dispersion after purification by centrifugation. The dispersion containing iotrolan-based nanoparticles exhibited a lower iodine concentration than the dispersion with iopromide-filled nanoparticles. C) Electron micrographs of nanoparticles filled a) with iopromide and b) with iotrolan.

The entrapment efficiency correlating with the amount of free iodine in solution was similar for both samples. Starting with the same initial concentration of iodine, only (88 ± 24) and (48 ± 3) mg/L of iodine were detected for iopromide and iotrolan in the supernatant, respectively. For iotrolan, slightly less iodine was found in the supernatant. This implements an entrapment efficiency of ~ 90%.

Interestingly, iotrolan-based nanoparticles resulted in a larger diameter (420 nm, PDI = 0.39 for iopromide based nanoparticles compared to ~1 µm, PDI = 0.06 for iotrolan based nanoparticles). Though DLS measurements implement a narrow size distribution for iotrolan based nanoparticles (PDI 0.06), a broad size distribution was observed in SEM micrographs, ranging from ~50 nm to several microns. Larger particles exhibit a stronger scattering intensity than smaller particles, which complicates the detection of smaller particles in bimodal samples by DLS.[87] Due to the larger size, the colloidal stability in water of iotrolan based nanoparticles was low, which resulted in a decrease of the final iodine concentration (Figure 44B). As iotrolan-based nanoparticles resulted in a larger hydrodynamic diameter and were not colloidally stable, iopromide-based nanoparticles were used in the following section.

4.3.4.8. Influence of Solvent Viscosity on Nanoparticle Size Distribution

SEM and TEM images of nanoparticles revealed a rather broad size distribution (Figure 41–Figure 44). These nanoparticles were synthesized via inverse miniemulsion. The emulsification was achieved *via* sonication. During sonication, droplets are ruptured to form smaller droplets. Besides the fission of droplets, also fusion as a consequence of collisions between the droplets occurs.[205] The size distribution might be attributed to the high viscosity η of DMSO ($\eta_{\mathrm{DMSO,25°C}} = 2.0$ mPa s)[206] in comparison to other solvents. Nazarzadeh *et al.* reported the viscosity of the dispersed phase to play a major role regarding droplet size and droplet size distribution in a miniemulsion. The droplet size distribution is related to the droplet rupturing mechanism. For emulsions with a low-viscosity dispersed phase (*i.e.* 0.49 mPa s) it has been reported that the droplets burst upon sonication to form several smaller droplets of comparable size. For high viscosity droplets (*i.e.* 96.5 mPa s), droplet rupturing occurs rather by stretching the droplets than by bursting, resulting in a bimodal size distribution. Upon longer sonication times, the bimodal droplet size distribution evolved to a monomodal size distribution.[207]

In this section, DMF is presented as an alternative solvent to DMSO. DMF exhibits, among other differences, a much lower viscosity than DMSO ($\eta_{\mathrm{DMF,25°C}} = 0.8$ mPa s).[206] Furthermore, DMF is immiscible with cyclohexane and solubilizes iopromide and TDI. Therefore, it is a suitable solvent as a dispersed phase in inverse miniemulsion. The nanoparticle formation with DMF as dispersed phase was confirmed by DLS and SEM measurements (Figure 45c). The encapsulation efficiency was found to be similar to DMSO-based nanoparticles (*ee* = ~96%). DLS measurements revealed a slightly larger hydrodynamic radius but a narrower size distribution when compared to DMSO-based nanoparticles ($d_{\mathrm{h,DMF}} = 370$ nm, PDI = 0.13; $d_{\mathrm{h,DMSO}} = 310$ nm, PDI = 0.39), though also larger particles have been observed in SEM images.

4.3.4.9. Amount of TDI

The amount of TDI is expected to affect the amount of cross-linking, the hydrophilicity, and, as a consequence, the entrapment efficiency of the payload inside the nanoparticles.[208] The lower the entrapment efficiency, the more free iodine can be found in the supernatant after centrifugation of the nanoparticle dispersion. The result is expressed as encapsulation efficiency after re-dispersion in water after purification EE_{r}. Especially the hydrophilicity is crucial for the colloidal stability of the nanoparticle dispersion in water. To remove agglomerated nanoparticles, a first centrifugation step with 500 rpm was applied. The nanoparticles, which did not precipitate during this first centrifugation step, were used for further analysis. If the nanoparticles was not colloidally stable, iodine was neither found in the supernatant nor in the purified nanoparticle dispersion. As a consequence, the remaining amount of iodine found in the nanoparticles dispersion after purification was far below the theoretically expected value, that can be calculated from the initial amount of iopromide used for the nanoparticle synthesis. The precipitated nanoparticles were not available for ICP-OES measurements.

The amount of TDI was varied to find the best compromise between entrapment efficiency and colloidal stability. Nanoparticles with three different amounts of TDI per batch were synthesized. Nanoparticles were obtained for all samples (Figure 45).

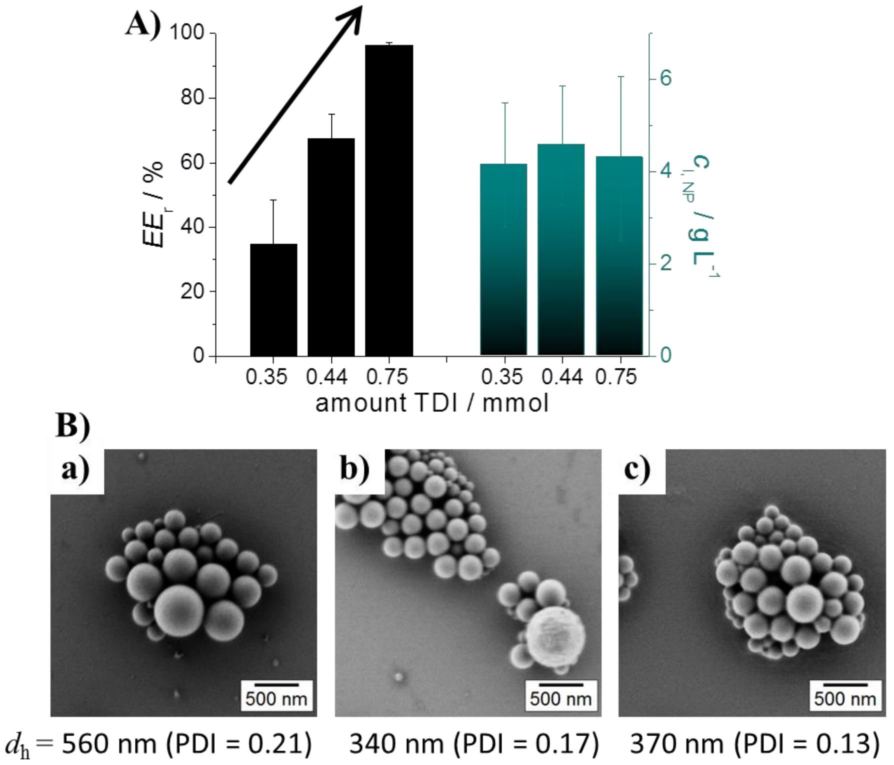

Figure 45: Iopromide-containing nanoparticles, synthesized using DMF as a dispersed phase, with different amounts of TDI cross-linker. A) Encapsulation efficiency EE_r calculated from the ratio of the total iodine amount in dispersion and the iodine content in the supernatant after centrifugation (left) and the iodine content of the nanoparticle dispersion after purification via centrifugation (right). The data points were averaged over two samples, respectively. Error bars represent standard deviations. The encapsulation efficiency increased with increasing amount of TDI per batch. B) SEM micrographs and DLS data revealing nanoparticle formation.

With 0.35 mmol of TDI per batch in presence of 0.3 mmol of iopromide and 50 mg surfactant, but without the addition of further diamines, only ~35% of iodine was found in the nanoparticle dispersion after purification. By increasing the amount of TDI from 0.35 mmol to 0.75 mmol per batch while keeping the amount of the other components constant, the entrapment efficiency increased from ~35% to ~96%. In turn, the colloidal stability decreased with increasing amount of TDI, yielding to no increase of the iodine content in the purified nanoparticle dispersion. The iodine containing nanoparticles formed agglomerates and precipitated. Thus, the iodine content measured was with ~4 g/L far below the theoretically expected one of ~19 g/L.

Because the approaches to engineer the hydrophilicity of the nanoparticle surface resulted in a higher leakage of the entrapped payload, another approach to increase the iodine concentration in the final dispersion was tested.

4.3.4.10. Reducing Agglomerates by Sonication

Upon transfer of the nanoparticles from cyclohexane into water, no colloidally stable nanoparticles dispersions were obtained. The obtained iodine content in the nanoparticle dispersion was, therefore, far below the theoretical expected iodine content (see Section 4.3.4.4). Thus, modifications of the transfer step were performed. By sonication shortly after the mixing of the two phases, the formation of agglomerates could be reduced. The iodine concentration in water after purification was measured (Figure 46).

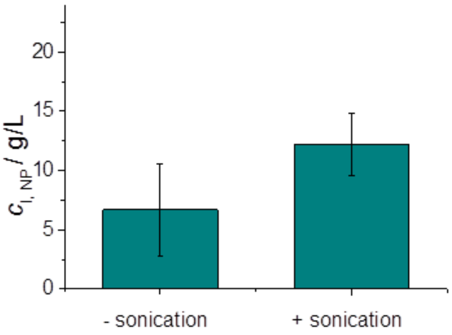

Figure 46: Comparison of the resulting iodine concentration of the nanoparticle dispersion after purification, transferred from cyclohexane to water without or with sonication.

During the transfer from cyclohexane to water, the hydrophobic nanoparticles were brought into a hydrophilic environment. By the addition of sodium dodecyl sulfate (SDS) as surfactant, an electrostatic stabilization of the nanoparticles was achieved. For iopromide nanoparticles, the colloidal stabilization by the surfactant was not enough. The formation of agglomerates led to precipitation of the particles and reduced the total amount of particles in the dispersion and therefore the iodine content in the dispersion. By the application of sonication shortly after the introduction into the aqueous phase, the formed agglomerates were separated again by sonication. The iodine concentration after purification was increased from 7 ± 4 g/L up to 12 ± 3 g/L by sonicating the sample during the transfer step. The later dispersion exhibited a solid content of (4.9 ± 0.2)%. By sonication, a suitable iodine concentration[187] was reached for *in vivo* visualization of the nanoparticles.

4.3.4.11. Interaction of the Nanoparticles with Plasma

To investigate whether the nanoparticles are suitable for biomedical applications, the interaction of the nanoparticles with plasma was examined. DLS measurements of the nanoparticles in the presence of human blood plasma were performed (Figure 47).

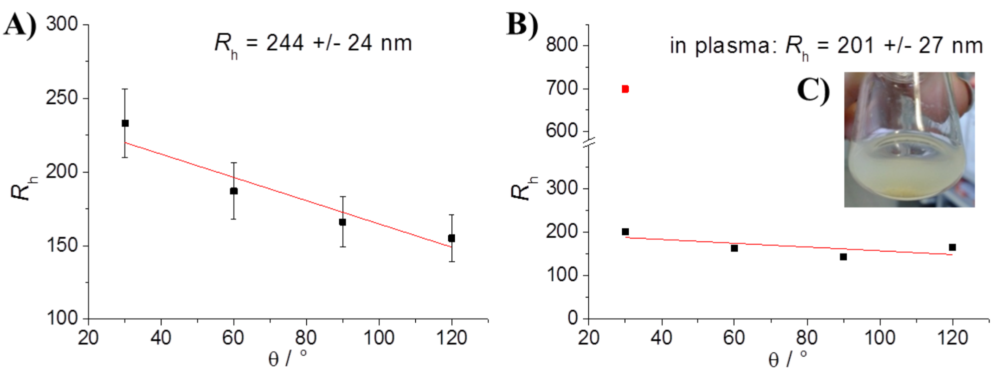

Figure 47: Nanoparticle size in plasma: A) DLS results of nanoparticles without plasma: $R = 244 \pm 24$ nm, no agglomerates observed. B) DLS of nanoparticles in human blood plasma: $R_h = 201 \pm 27$ nm. At $\theta = 30°$ (most sensitive scattering angle) a second signal (depicted in red) is observed. Aggregates with $R_h \approx 700$ nm (~ 40% of scattered intensity) are formed. C) Large agglomerates are formed after addition of nanoparticles to human blood plasma. Agglomerates disappear mostly upon diluting the nanoparticle dispersion with human blood plasma.

Prior to the addition of human blood plasma, the nanoparticles were found to have a hydrodynamic radius of 244 ± 24 nm. Dispersed in human blood plasma, the hydrodynamic radius of the nanoparticles was found to be 201 ± 27 nm, which is not significant different from the radius without human blood plasma ($P > 0.05$). At a scattering angle of 30°, a second signal was observed for the nanoparticles in human blood plasma, indicating the formation of agglomerates. At higher concentrations of nanoparticles, the formation of agglomerates was visible (Figure 47 C).

To gain further insight into the interaction of the nanoparticles with plasma, the proteins adsorbed onto the nanoparticle surface were analyzed by SDS-PAGE by

Johanna Simon (Figure 48). The nanoparticle dispersion was incubated with human blood plasma. The loosely bound proteins were removed by centrifugation and the remaining proteins forming the protein hard corona were analyzed by SDS-PAGE. As the amount of adsorbed proteins was unknown, different amounts ranging from 0.5 to 2 times 16.25 µL of nanoparticle dispersion were applied, to obtain a good visualization of the adsorbed proteins. To identify the molecular weight, a marker was added. For comparison, human blood plasma was also tested (Figure 48).

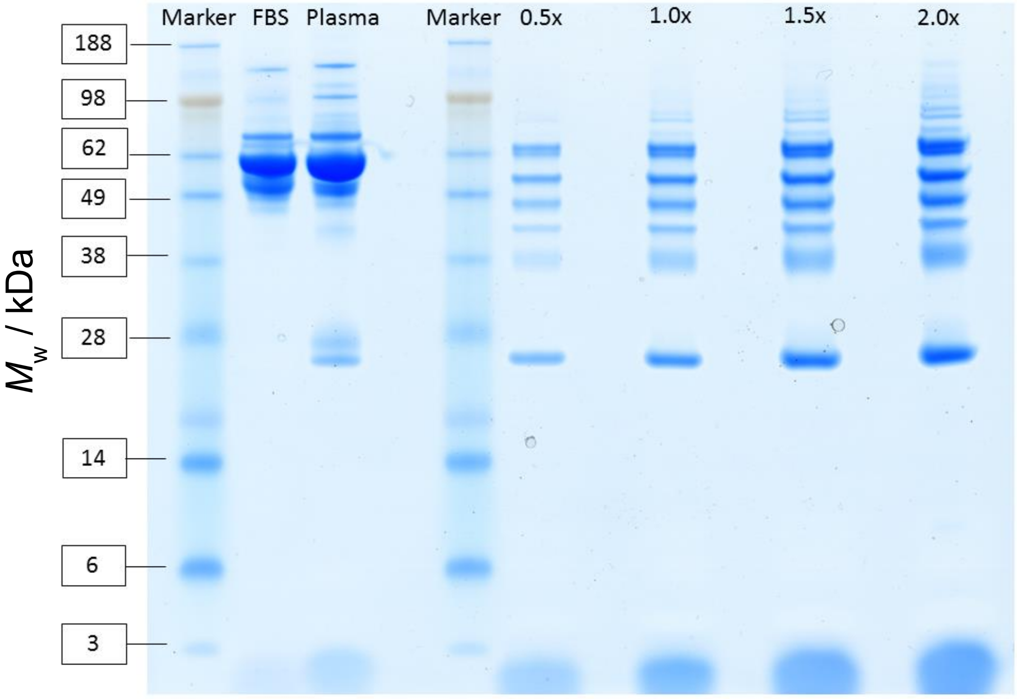

Figure 48: Sodium dodecyl sulfate-polyacrylamide gel electrophoreses (SDS-PAGE), measured by Johanna Simon: Proteins are separated due to their molecular weight. Blue lines are marking the proteins. The marker (left row) allows the identification of the molecular weights (y-axis). As comparison, FBS and human blood plasma was recorded. The nanoparticles were incubated with human blood plasma prior to SDS-PAGE measurements. Because the amount of the adsorbed proteins was unknown, different amounts of nanoparticle dispersion were added, ranging from 0.5 to 2 times 16.25 µL of sample (referring to the protocol reported in literature),[164,165] to obtain a sufficient visualization of the adsorbed proteins. While albumin is the most present protein class in FBS and plasma, other proteins, ranging from ~38 kDa to ~100 kDa, were more present in the nanoparticle protein corona.

As expected, the blue lines are getting more intense with increasing amount of sample used in the experiment. The SDS-PAGE revealed a different protein pattern in the protein corona of the nanoparticles hard corona from the protein composition of the plasma. The band at ~62 kDa is still observed for the nanoparticles, but less intense than in the human blood plasma, indicating that fewer albumins are present in the protein corona of the nanoparticles. As the band for albumin is less intense, bands of other proteins become visible. The SDS-PAGE indicates a high diversity of proteins over the whole detectable molecular weight range (3 kDa–188 kDa) in the protein corona of the nanoparticles. Possible proteins corresponding to the molecular weight range of the most intense bands could be immuniglobolin G (IgG) light chain (~22 kDa), fibrinogen alpha (~47 kDa), IgG heavy chain (~50 kDa), fibrinogen beta (56 kDa), albumin (~66 kDa), and fibrinogen gamma (63 kDa).[176] Fibrinogen is a coagulation factor in blood.[209] In the protein corona of nanocarriers it might cause the formation of agglomerates,[210] as it was observed for these particles during DLS measurements (Figure 47 B and C). Albumin is the most abundant protein in human blood and is a versatile carrier protein.[211,212] IgG in the protein corona is reported to trigger the cell uptake by macrophages to remove foreign material from the blood stream.[175,213]

To gain evidence about which proteins are present in the protein corona, complementary experiments such as LC-MS are required.

4.3.5. Conclusions

This chapter was focused on two main issues: encapsulation efficiency and colloidal stability. The encapsulation efficiency of iopromide in nanocapsules was not exceeding ~35%. To overcome the leakage from the nanocarriers, nanoparticles instead of nanocapsules were synthesized. In polyurea nanoparticles, the entrapment efficiency of iopromide was increased from ~35% for nanocapsules to ~94%. NMR spectroscopy experiments indicated a chemical reaction taking place between the hydroxyl groups of iopromide and the isocyanate groups of TDI. Without the formation of covalent bonds between the cargo and the nanocarrier matrix, the entrapment of hexaiodobenzene into nanoparticles was possible with an entrapment efficiency of ~60%. Iotrolan, a dimer of iopromide exhibiting a lower osmotic pressure at the same iodine concentration, showed similar entrapment efficiency but a lower colloidal stability than iopromide-based nanoparticles.

The colloidal stability is crucial for obtaining a high iodine concentration in the final dispersion as well as for biomedical applications. The increase of the colloidal stability was attempted by several approaches. The hydrophilicity was addressed by addition of 1,2-diaminoethane and by adjusting the amount of TDI in the formulation. The size distribution of the nanoparticles, which is also crucial for colloidal stability, was tuned by the viscosity of the solvent used in the dispersed phase. The transfer step from cyclohexane into water was optimized by sonication to reduce the formation of agglomerates. Finally, the interaction between iopromide containing nanoparticles and plasma was analyzed.

The use of a microfluidizer, as presented for DMSO-filled nanocapsules in Chapter 4.4, is expected to improve the nanoparticle size distribution. Surface modification might further increase the colloidal stability. Cell experiments and *in vivo* experiments shall reveal toxicity and biodistribution of iopromide containing nanoparticles.

4.4. Triggered Release from HES-HSA Nanocapsules

Nanocarriers are able to reach targets that are otherwise difficult to access. Besides nanocarriers as diagnostic tools introduced in Chapter 4.2 and 4.3, the treatment of the identified tumors is of high interest. For drug delivery, not only a high loading capacity is important but also the possibility to control the release of encapsulated payloads.

4.4.1. Abstract

The protein STAT3 (Signal Transducer and Activator of Transcription3) is a transcription factor. It is critically involved in tumor growth and in tumor escape mechanisms, which makes it an attractive target in cancer immunotherapy.[214] STAT3 inhibitors inhibit the phosphorylation of STAT3, are soluble in DMSO but practically insoluble in water, and highly toxic.[215] Entrapped into nanocapsules with DMSO-core, STAT3 inhibitors can be dispersed in an aqueous environment. Shielding by the nanocapsule shell hinders the direct contact of the encapsulated STAT3 inhibitors with the biological environment and reduces therefore the toxicity of the entrapped STAT3 inhibitors. Moreover the required dose of STAT3 inhibitors can be reduced as the desired cells can be directly targeted.

A suitable nanocarrier for the transport of STAT3 inhibitors has to fulfill two major issues. Firstly, the nanocapsules should not be depleted by the immune system before reaching their target. The "stealth effect" is describing the ability of certain materials to reduce unspecific cell uptake of nanocarriers and to minimize the immune response in the body.[216-218] Therefore, nanocarriers based on the stealth material hydroxyethylstarch were synthesized. Secondly, the drug has to be released once the target is reached. Human serum albumin was incorporated into the HES-based nanocapsules shell membrane as predetermined breaking points to allow the scission of the nanocapsules and the enzymatic triggered release of the encapsulated STAT3 inhibitors (Figure 49). As proteins tend to form clusters, we expect a phase separation between HES and HSA and, therefore, the formation of HES and HSA domains. Upon enzymatic degradation of HSA, channels are expected to form to allow for the release of the encapsulated cargo.

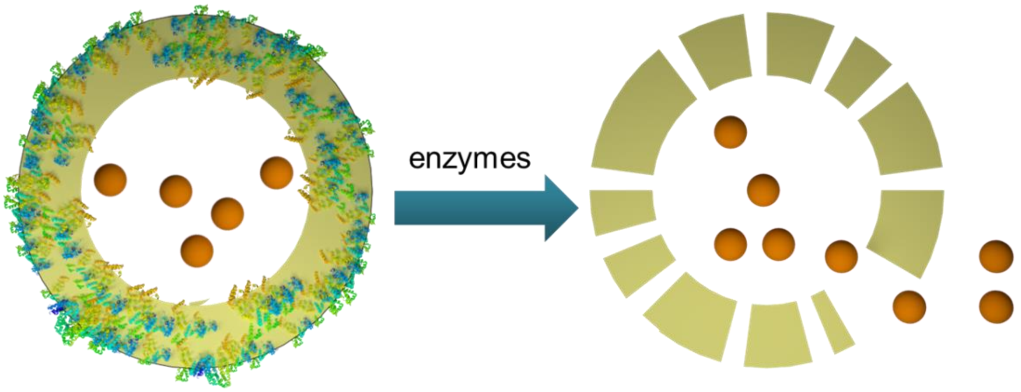

Figure 49: Scheme of nanocontainers based on HSA (multicolored) and HES (yellow). The cargo (orange) is released upon enzymatic degradation of the proteins that are located in the shell of the nanocarriers.

4.4.2. Introduction

STAT3 (Signal Transducer and Activator of Transcription3) is an attractive target in cancer immunotherapy as it is a protein involved in cell growth and, especially, in tumor growth. Furthermore, hyperphosphorylated STAT3 is found in tolerance inducing immune cells in the tumor microenvironment, where it is facilitating tumor escape.[214] STAT3 inhibitors are reported to inhibit the protein STAT3 by disabling the dimerization or the phosphorylation. But STAT3 inhibitors are also inhibiting cell growth of healthy cells, making the inhibitors highly toxic.[219] Besides, the STAT3 inhibitors are soluble in organic solvents such as DMSO (*i.e.* solubility of S3I-201 in DMSO: >10 mg/mL ≙ >0.03 M) but practically insoluble in water (*i.e.* solubility of S3I-201 in H_2O: <0.01 mg/mL ≙ <0.03 mM).[220] By encapsulating them in DMSO-core nanocapsules, STAT3 inhibitors become dispersible in water and the toxicity is reduced, as the nanocapsule shell is shielding the payload from the environment.

Atovaquone (Scheme 3) is an FDA-approved drug used against *Pneumocystis carinii* pneumonia, a major opportunistic infection in individuals with immunosuppression such as AIDS,[221] toxoplasmosis,[222] and cryptosporidiosis.[223] Furthermore, atovaquone is used for the treatment and the prevention of malaria. In combination with azithromycin, it is effective for the treatment of babesiosis.[224] The STAT3 inhibiting effect of atovaquone was recently discovered.[225,226] Some patents are reporting nanoparticles containing atovaquone.[227-229] Dearn *et al.* reported of nanosuspensions of atovaquone in the size range of 0.1 to 3 µm, prepared by mixing atovaquone with an aqueous surfactant solution followed by microfluidization.[229] Shubar *et al.* found nanosuspensions of atovaquone that were coated with apolipoprotein E and showed an improved uptake into the brain of mice and a reduced *T. gonadi* infection.[230] Recently, Soleimani *et al.* prepared STAT3 inhibitor loaded polymeric micelles of PEO_{114}-*b*-PCL_{22} or PEO_{114}-*b*-$PBCL_{20}$ in the size range of 40–70 nm for the treatment of melanoma. The encapsulation efficiency was for the STAT3 inhibitor S3I-201 25% maximum, resulting in a drug loading of the micelles (mg S3I-201 per mg polymer) of 2.3%, which is rather low. The concentration of S3I-201 in the aqueous dispersion was 0.68 mM. In contrary, an encapsulation efficiency of 94% and a drug loading of 9.2% of the micelles was obtained for the encapsulation of the STAT3 inhibitor S3I-1757, resulting in a concentration of 1.8 mM of S3I-1757 in the aqueous dispersion.[231]

Though the stealth effect is widely discussed, to our knowledge no studies are reporting so far regarding nanocarriers consisting of a stealth material and containing predetermined breaking points made of HSA to allow for an enzymatic triggered release for drug delivery of hydrophilic drugs. While a number of nanoscale atovaquone has been reported in literature, the STAT3 inhibiting effect of nanoscale atovaquone remains unclear. Nanocarriers of the STAT3 inhibitor S3I-201 with sufficient encapsulation efficiency are unreported to our knowledge.

Here, we aim at the encapsulation of two STAT3 inhibitors, S3I-201 and atovaquone, selected as models from the broad variety of STAT3 inhibitors.[215] In contrary to most of the other STAT3 inhibitors, atovaquone is not toxic (Scheme 3).[225,226]

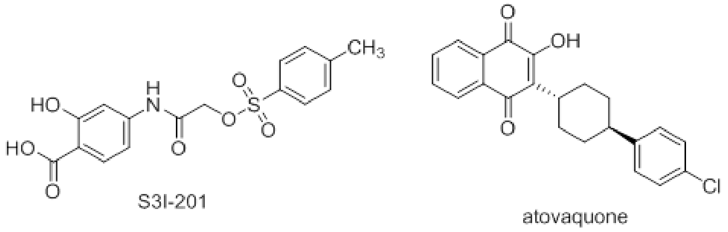

Scheme 3: Chemical structure of encapsulated payloads. STAT3 inhibitors S3I-201 and atovaquone were chosen as models.

The ability of certain materials to reduce unspecific cell uptake of nanocarriers and to minimize the immune response in the body is referred to as "stealth effect". Biocompatible hydroxyethylstarch (HES) is reported to exhibit stealth properties.[216-218] Herein, nanocapsules based on HES were synthesized. As the degradation of HES is taking place on a much longer timescale than the degradation of human serum albumin (HSA),[8,232] HSA was incorporated into the nanocapsules shell to accelerate the enzymatic triggered release of the payload (Figure 49).

For the formation of nanocapsules, TDI was used as cross-linker (Scheme 4). The isocyanate groups of TDI are meant to react with the functional groups of HSA, which is bearing hydroxyl, thiol and amino groups, and with the hydroxyl groups of HES. The reaction rate for the reaction of primary aliphatic amines with isocyanates is ~1000 times higher than the reaction rate of primary hydroxyl groups.[199] The reactivity of thiol groups is much lower than the reactivity of hydroxyl groups.[199,233-235]

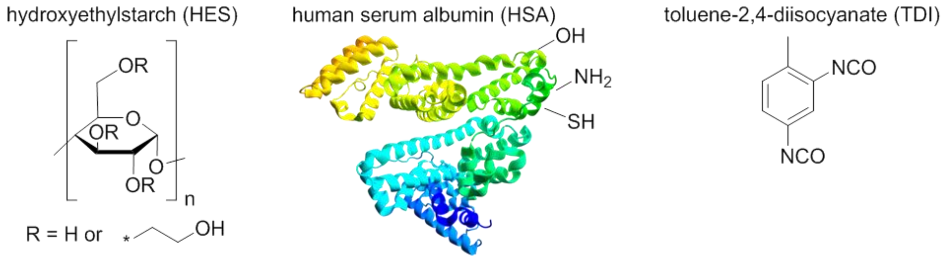

Scheme 4: Educts used for the synthesis of HES-HSA nanocarriers. HSA is a protein, containing functional groups as hydroxy, amino or thiol groups. Hydroxyethylstarch and HSA are crosslinked with TDI.

4.4.3. Materials and Methods

Materials

Chemicals were purchased as follows: hydroxyethylstarch (HES) (M_w = 130,000 g mol^{-1}, degree of substitution = 0.4, dialyzed and freeze dried from infusion solution) (Fresenius Kabi); toluene-2,4-diisocyanate (TDI, 95%, filtrated over 0.2 µm nylon syringe filter (Chromacol) prior to use) and atovaquone (>98%) (Sigma Aldrich); sodium dodecyl sulfate (SDS) (Fluka and Alfa Aesar); cyclohexane (>99%) (VWR); DMSO (99.7+%, Acros Organics); sulfo-cyanine-5-carboxylic acid

(Cy5, Lumiprobe); CellTracker Green CMFDA (biomol); S3I-201 (Calbiochem). The surfactant poly((ethylene-*co*-butylene)-*b*-(ethylene oxide)) P(E/B-*b*-EO), with a poly(ethylene-*co*-butylene) block (M_w = 3,700 g mol^{-1}) and a poly(ethylene oxide) block (M_w = 2,900 g mol^{-1}) was synthesized as described before *via* anionic polymerization.[236] All chemicals were used as received unless otherwise noted. Mili-Q water (18 MΩ cm) was used throughout all experiments.

Synthesis of Nanocapsules via Inverse Miniemulsion

The surfactant P(E/B-*b*-EO) (200 mg) was dissolved in cyclohexane (15 g). For HES-TDI nanocapsules, HES (200 mg) and $CaCl_2$ (40 mg) were dissolved in the polar phase consisting of a mixture of H_2O and DMSO with a DMSO content ranging from 0%, 50%, 90%, 95% to 100% (v/v). For HES-HSA nanocapsules with different ratios of HES and HSA, the total amount of HES and HSA was 200 mg and the ratio was adjusted by varying the amount of the components, respectively. To avoid denaturation of HSA, no salt ($CaCl_2$) was added as osmotic pressure agent. For the encapsulation of STAT3 inhibitors, HSA (100 mg) was dissolved in MiliQ water (1.4 mL) and mixed with a solution of HES (100 mg) in DMSO (1.54 g). In DMSO were further dissolved the respective fluorescent dyes Cy5 (60 µg) and/or CellTracker Green (0.2 mg) and, if required, the STAT3 inhibitors S3I-201 or atovaquone (10 mg), respectively.

The two phases were mixed and a coarse emulsion was obtained by using the Ultra Turrax T18 digital (IKA), equipped with a dispersing tool of the type S18N10 at 24 k rpm for 60 s. Subsequently the pre-emulsion was transferred to the microfluidizer LV1, equipped with a ceramic chamber of the type F20y 75µ. The cooling coil was placed in a water bath of 4–6 °C to cool the sample. The first stroke was discarded and the sample was pumped 3 times at a working pressure of 1,500 bar through the chamber. To the emulsion (9.2 g) a mixture consisting of cyclohexane (5 g), P(E/B-*b*-EO) (30 mg) and TDI (100 mg) was added dropwise. The sample was allowed to react for 24 h under stirring at room temperature.

Transfer to Water

If not otherwise mentioned, the unpurified nanocapsule dispersion in cyclohexane (1 g) was added dropwise to a solution of 0.1 wt% SDS (Fluka) in water (5 g). The sample was stirred in an open vial to evaporate cyclohexane.

Release of Cy5 from HES-TDI nanocapsules

The HES-TDI nanocapsules dispersed in water (4 mL) were transferred into a dialysis tube (14 kDa MWCO, regenerated cellulose dialysis tube, Roth) and dialyzed against MiliQ water (146 mL). The release of Cy5 was evaluated from the dialysate. After 1, 3, 6, 24, 48 and 72 h, respectively, 1 mL of dialysate was drawn and the content of Cy5 was determined by fluorescence intensity using the platereader Tecan i-control infinite M1000 (λ_{ex} = 646 nm, λ_{em} = 662 nm). For the measurement of the fluorescence intensity, 100 µL of sample were placed into a 96 well plate. The fluorescence intensity of each dialysate sample was measured three times. No correction for the detected signals was used. To determine the concentration of Cy5, the fluorescence intensity from five different Cy5 concentrations in MiliQ water was recorded and a calibration curve was obtained by linear regression. No background correction was used for the calibration curve. The release was calculated by comparing the amount of Cy5 released during dialysis to the theoretical amount of Cy5 contained in the nanoparticles.

Release of Cy5 upon enzymatic degradation of the nanocontainers

To avoid loss of the fluorescent dye, the nanocapsule dispersions were not purified. After transfer to water, trypsin was added (444 µL of trypsin solution to 4.00 g of nanocapsule dispersion). The dispersion was stirred at room temperature for 1 h, transferred into a dialysis tube (100 kDa MWCO cellulose ester, spectra por), and dialyzed against MiliQ water (146 mL). The release of Cy5 was evaluated from the dialysate. After 1, 3, 6, 24, 48 and 72 h, respectively, 1 mL of dialysate was drawn and the content of Cy5 was determined by fluorescence intensity using the platereader (λ_{ex} = 646 nm, λ_{em} = 662 nm). No correction for the detected signals was used.

HES-TDI Nanocapsules filled with 90%, 95% or 100% DMSO

The surfactant P(E/B-*b*-EO) (100 mg) was dissolved in cyclohexane (7.5 g).

HES (100 mg), $CaCl_2$ (20 mg) and the fluorescent dye Cy5 (20 µg) were dissolved in the polar phase consisting of a mixture of H_2O and DMSO with a DMSO content ranging from 90%, 95%, 100% (v/v DMSO/H_2O), and added to the cyclohexane phase.

Emulsification was carried out as described prior in this chapter. By using the Ultra Turrax T18 digital (IKA), equipped with a dispersing tool of the type S18N10 at 24 k rpm for 60 s, a coarse emulsion was obtained. The coarse emulsion was transferred to the microfluidizer LV1, equipped with a ceramic chamber of the type F20y 75µ. To cool the sample, the cooling coil was placed in a water bath of 4–6 °C. The first stroke was discarded. The sample was passed 3 times at a working pressure of 1,500 bar through the chamber. To the miniemulsion (4.5 g), a mixture consisting of cyclohexane (2.45 g), P(E/B-*b*-EO) (15 mg) and TDI (49 mg) was added dropwise. The sample was allowed to react for 24 h under stirring at room temperature. The unpurified nanocapsule dispersion in cyclohexane (400 µL) was added dropwise to a solution of 0.1 wt% SDS (Alfa Aesar) in water (5 g). The sample was stirred in an open vial to evaporate cyclohexane. The nanocapsules dispersed in water (3 mL) were transferred into a dialysis tube (14 kDa MWCO, regenerated cellulose dialysis tube, Roth) and dialyzed against VE-water (900 mL). The release of Cy5 was evaluated from the dialysate after 24 h from the fluorescence intensity ($\lambda_{ex} = 646$ nm, $\lambda_{em} = 662$ nm). For the detected fluorescence intensity, no correction was used.

Enzymatic Degradation of Celltracker Green

Purification of the nanocapsule dispersion was performed *via* dialysis for 24 h (MWCO 14 kDa, regenerated cellulose dialysis tube, Roth). To 450 µL of dialyzed nanocapsule dispersion, 50 µL of trypsin were added. The nanocapsules were kept shaking at 37°C for 3 h and afterwards at room temperature. The fluorescence intensity of the nanocapsule dispersions was measured using the plate reader ($\lambda_{ex} = 492$ nm, $\lambda_{em} = 517$ nm). For comparison, the fluorescence intensity was divided by the solid content of the nanocapsule dispersions.

Analytical Tools

To determine the hydrodynamic radius and size distribution of the nanocapsules, dynamic light scattering (DLS) measurements were performed using a PSS Nicomp Particle Sizer 380 operating at a scattering angle of 90°. Prior to DLS measurements, the nanocapsule dispersions were diluted with the respective solvent (cyclohexane or water). The solid content of the cyclohexane and aqueous nanocapsule dispersions were assessed gravimetrically by comparing the weight of 100 µL of the respective sample before and after freeze-drying. Scanning electron microscopy (SEM) images were recorded with a LEO (Zeiss) 1530 Gemini field emission microscope at an extractor voltage of 0.2 kV. For transmission electron microscopy (TEM) images, a JEOL JEM-1400 electron microscope operating at an acceleration voltage of 120 kV was used. The samples for SEM and TEM were prepared by drop-casting. A diluted nanocapsule dispersion with a solid content of about 0.01 wt% was dropped onto a silicon wafer or onto a carbon-coated copper grid, respectively, and the solvent was allowed to evaporate. A Zetasizer ZEN2600 system from Malvern Instruments was used to assess the zeta potential. Three measurements were run per sample with 10–100 runs per measurement. Prior to zeta potential measurements, the sample was diluted with 1 mM potassium chloride.

Statistical Analysis

Errors given for the measured release of Cy5 after 72 h were calculated using the Gaussian error propagation.The statistical significance was determined using the unpaired t-test. A two-tailed P value of less than 0.05 was considered to indicate statistical significance. The P value was calculated using the free web calculator GraphPad QuickCalcs *t* test calculator by GraphPad Software, La Jolla California, USA.[237]

High Performance Liquid Chromatography

High performance liquid chromatography (HPLC) measurements were performed using a HPLC Agilent Technologies Series 1200 equipped with a degasser, quaternary gradient pump, column oven and photodiode detector (all

Agilent Technologies), and an injection valve 7725i with 20 µl loop (Rheodyne). A reversed phase column (HD8, Macherey Nagel) with a length of 125 mm, a diameter of 4 mm and a particle size of 5 µm was chosen. The flow was set to 1 mL/min. The temperature was 20 °C. As eluent, a mixture of acetonitrile (HPLC grade, Fischer) and water (containing 0.1% TFA, HPLC grade, Merck) was used in the beginning and was changed to 100% acetonitrile after 10 min. The signal at the UV detector was recorded at 270 nm or at 254 nm for atovaquone or S3I-201, respectively. Prior to each measurement, the baseline was recorded. Each measurement was run 2 times. For quantification of the STAT3 inhibitors S3I-201 and atovaquone, a calibration curve was recorded. 2, 4, 6, 8, 10 µL of a solution of known concentration of S3I-201 or atovaquone were injected and the absorbance signal was integrated. The encapsulation efficiency was calculated by comparing the amount of STAT3 inhibitor found in the dialysate to the theoretically expected content.

Cell Experiments

Cell experiments were performed in cooperation with the AG Steinbrink at the University Medical Center Mainz by Tina Hares and Matthias Domogalla to investigate the effect of the generated nanocapsules on tumor cells, uptake and viability by the human HeLa cells. The HeLa cell line is an immortal cancer cell line that was isolated from a cervical cancer of Henriette Lacks in 1952 and hence serves as an essential tool in cancer research (Greely H. T. & Cho M.K. 2013).[238] For cell culture maintenance HeLa cells were grown in 75 cm^2 cell culture flasks (Greiner BioOne) and diluted (with the factor 1/10, v/v) twice a week by trypsinization. Cells were harvested and seeded at a density 0.5x10^6 cells in 6 well plates (Costar). After a resting period of 24 h, nanocapsules were added at a concentration of 10 µg/mL and 25 µg/mL. Past 16 h, cells were obtained, stained with Fixable Viablility Dye (Thermo Fisher), and analyzed by the BD™ LSR II flow cytometer (BD Biosciences).

4.4.4. Results and Discussion

Because STAT3 inhibitors are practically insoluble in water (*i.e.* solubility of S3I-201 in H_2O: <0.01 mg/mL ≙ <0.03 mM) but soluble in DMSO (*i.e.* solubility of

S3I-201 in DMSO: >10 mg/mL ≙ >0.03 M),[220] DMSO was chosen as solvent for the dispersed phase in the inverse miniemulsion process. On the contrary, HSA, which was chosen as model protein class because it is readily available, is only slightly soluble in DMSO (solubility of BSA (same class of proteins as HSA but different protein source) in DMSO: 5.12 mg/L ≙ 75.29 µM),[239] but well soluble in water (>50 mg/mL).[240] Thus, a mixture of water and DMSO was needed to combine all components. To investigate the impact of DMSO on uncontrolled release, HES-TDI nanocapsules that contain different ratios of DMSO and water (0/100, 50/50, 90/10, 95/5, 100/0, v/v DMSO/water) were prepared. Subsequently, nanocapsules with different ratios of HES and HSA were synthesized and the release of the payload upon enzymatic degradation was examined. Finally, an optimized formulation for the nanocapsules was chosen for the encapsulation of STAT3 inhibitors.

4.4.4.1. HES-TDI Nanocapsules

Before focusing on the controlled release of the payload, the impact of the DMSO amount on the uncontrolled release was monitored. Because the nanoparticle shell is permeable for DMSO, uncontrolled release might be influenced by the amount of DMSO encapsulated in the nanoparticles. Furthermore, the morphology of the nanoparticles is affected, because the morphology is related to the solubility of TDI in the dispersed phase among other factors. TDI is indeed practically insoluble (e.g. <0.01 mg/mL ≙ <0.06 mM) in water,[241] but miscible with DMSO.[242] Thus, with DMSO as dispersed phase, the cross-linking reaction is not limited to the interphase and can take place inside the droplets as well. Nanocapsules were obtained with water as dispersed phase, whereas nanoparticles were obtained when DMSO instead of water was used as dispersed phase (Figure 50), as it was reported before by Crespy *et al.* for TDI as cross-linking agent.[117] Interestingly, the hydrodynamic diameter obtained from DLS measurements of the water-core HES-TDI nanocapsules was with ~200 nm larger than the diameter of nanoparticles obtained with DMSO as dispersed phase in inverse miniemulsion (~130 nm).

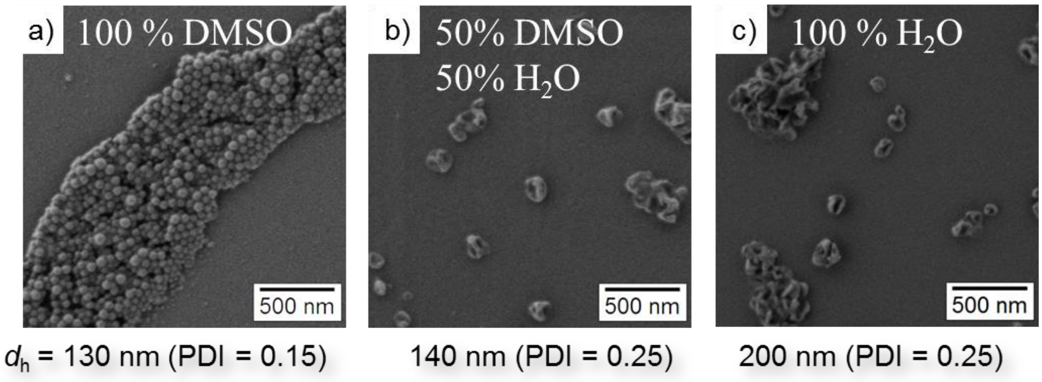

Figure 50: SEM and DLS results of HES-TDI nanocapsules. a) Filled with 100% DMSO, b) With 50% H_2O and 50% DMSO (v/v), c) 100% H_2O. With pure DMSO, nanoparticles are formed. With water, a core-shell morphology is observable.

HES nanoparticles cross-linked with TDI were synthesized with different DMSO/water ratios. To monitor the uncontrolled leakage in dependence of the DMSO/water ratio, the fluorescent dye sulfo-cyanine-5-carboxilic acid (Cy5) was incorporated into the nanoparticles. The release of Cy5 during dialysis was measured by fluorescence spectroscopy (Figure 51). After 72 h of dialysis, slightly less Cy5 was released from nanocapsules filled with water ((19 ± 3)%) than from nanoparticles filled with DMSO ((25 ± 2)%). The release for the nanocapsules containing 50:50 (v/v) DMSO/water mixture was (23 ± 1)% and is laying between the two other results. As expected, DMSO was accelerating the release of Cy5. The difference between 50% DMSO and 100% DMSO was found to be not significant ($P>0.1$).

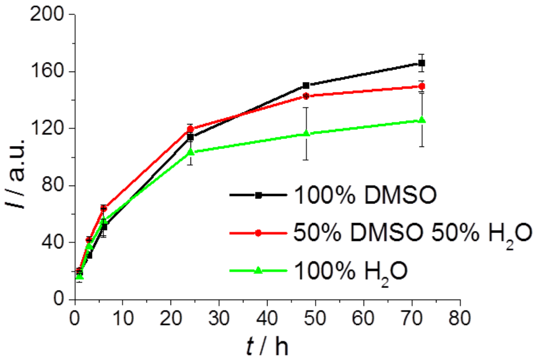

Figure 51: Release of Cy5 over time from HES-TDI nanocapsules during dialysis. The fluorescence intensity of Cy5 in the dialysate is plotted against the time of dialysis. The release from nanoparticles filled with pure DMSO (black) and nanocapsules filled with a DMSO/water mixture (red) is slightly faster than from nanocapsules filled with water (green).

The miscibility of TDI in the hydrophilic core determines the morphology of the nanoparticles (hollow or solid core). Because the morphology of the nanoparticles *e.g.,* hollow core nanocapsules or solid core nanoparticles, might influence the release profile, HES-TDI nanocapsules without HSA with a DMSO content ranging from 90 to 100% DMSO (v/v) were synthesized and the release of Cy5 after 24 h of dialysis was measured (Figure 52).

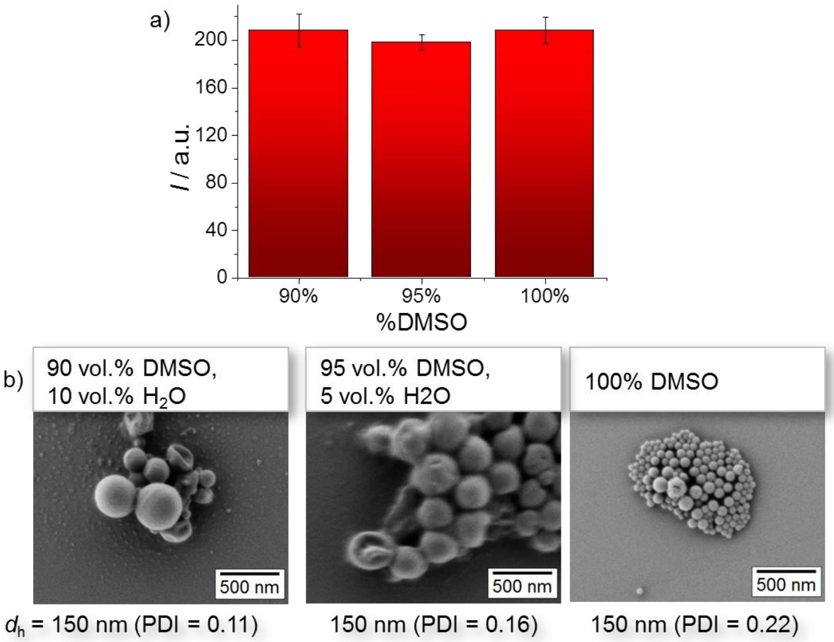

Figure 52: HES-TDI nanocapsules prepared without HSA a) Release of Cy5 during dialysis. The plot is showing the fluorescence intensity of Cy5 in the dialysate after 24 h of dialysis. The results show no significant difference in the release of Cy5 during dialysis after 24 h for the tested DMSO/water ratios ranging between pure DMSO, 95% DMSO or 90% DMSO (v/v). The error bars represent the standard deviation calculated from 3 fluorescence intensity measurements. b) SEM micrographs of HES-TDI nanocapsules after purification and results from DLS measurements. SEM images show some single and collapsed nanocapsules next to non-collapsed nanoparticles when water was present in the core. Though DLS measurements implement a similar size for all HES-TDI samples, different nanoparticle sizes were observed in SEM images.

The presence of DMSO complicated the observation of nanoparticles in SEM micrographs as DMSO was covering the nanoparticle sample as a film. Thus, the HES-TDI nanocapsules were purified for SEM images via centrifugation and washed with THF to remove the excess of DMSO. After purification, the SEM images were recorded. The size of the nanoparticles differed from DLS results measured prior to purification. HES-TDI nanocapsules filled with 100% of DMSO shrank to a diameter of ~100 nm after the excess DMSO was removed. This observation implements that nanoparticles were swollen by DMSO. In turn, the nanoparticles prepared with 5 and 10 v% of water as core exhibited a rather broad size distribution in SEM images ranging from ~100–~400 nm after purification. Single nanoparticles were collapsed, implementing the formation of some nanocapsules with a hollow core-shell structure. The different response to purification by washing with THF of the nanoparticles in the presence or absence of water in the hydrophilic core during the synthesis might be attributed to a side reaction between water and TDI (see Scheme 2, p. 91) yielding to the formation of polyurea in the presence of water as side reaction, resulting in a polymer different from HES cross-linked by TDI.

Though nanocapsules were obtained to some extent, no significant difference of the DMSO content in the range of 90–100% DMSO on the release of Cy5 during dialysis was observed after 24 h. Thus, the addition of water needed to dissolve HSA did not significantly affect the release profile of Cy5 from HES-TDI nanocapsules though it affected the nanoparticle morphology.

Because HSA is well water-soluble (>50 mg/mL)[240] but only slightly soluble in DMSO (solubility of bovine serum albumin (BSA, same class of proteins as HSA but different protein source) in DMSO: 5.12 mg/L ≙ 75.29 µM),[239] a mixture of both solvents was needed to synthesize HES-HSA-TDI nanocapsules. To dissolve a broad range of HSA amount, a water and DMSO ratio of 50/50 (v/v) was chosen for further experiments.

4.4.4.2. Release of Cy5 upon Enzymatic Degradation

HES-HSA nanocapsules with a DMSO/water ratio of 50:50 (v/v) have been synthesized at a ratio of HSA and HES of 5/95, 10/90, 50/50 wt%/wt%. To monitor the release, Cy5 was encapsulated. Trypsin was added to the nanocapsule dispersion to enable enzymatic degradation of the protein units. After 1 h of incubation at room temperature, the release of Cy5 during dialysis was measured. As a control, the release of Cy5 during dialysis without trypsin treatment was monitored (Figure 53).

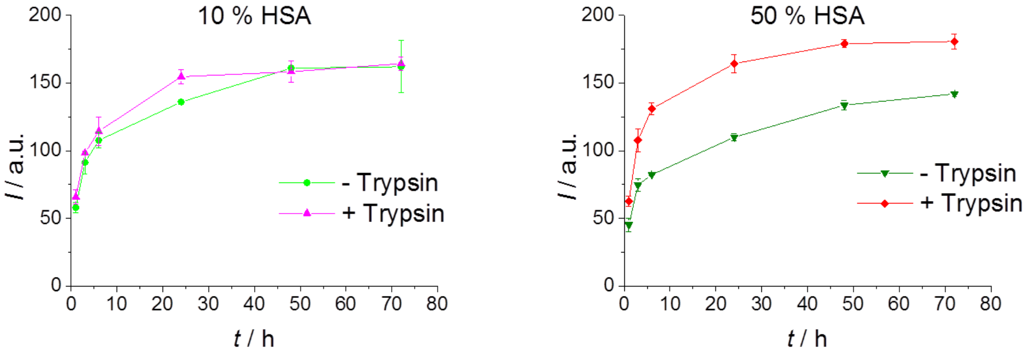

Figure 53: Release of Cy5 from HES$_{90}$-HSA$_{10}$-TDI and HES$_{50}$-HSA$_{50}$-TDI nanocapsules, prepared with 10 wt% and 50 wt% HSA, respectively. The fluorescence intensity of Cy5 in the dialysate is plotted against the time of dialysis. To trigger the release of the dye from the nanocapsules, the samples were treated with trypsin prior to dialysis (pink, red). To monitor the uncontrolled release of Cy5, the same sample without trypsin treatment was taken as control (green). The values presented are mean values and the error bars result from standard deviation from three fluorescence intensity measurements. The release behavior from these nanocapsules based on 10 wt% HSA is not affected by the addition of trypsin. More Cy5 was released after the addition of trypsin to nanocapsules based on 50 wt% HSA.

For the nanocapsules made of 10 wt% HSA, (25 ± 3)% of Cy5 was released without trypsin treatment after 72 h. With trypsin treatment prior to dialysis, (26 ± 1)% Cy5 were released. No significant difference between the treatment with trypsin and an uncontrolled release was observed ($P<0.05$).

10 wt% of HSA in the nanocapsule shell was not enough to allow for enzymatic controlled release. The release could be hindered for several reasons. The protein units can be shielded by HES and therefore cannot be degraded by trypsin. Or HSA is not forming clusters but is equally distributed inside the nanocapsule shell. Thus, enzymatic degradation of the proteins would not result in channels or holes in the nanocarriers' matrix and would not result in an enhanced permeability through the opened gates.

In turn, a significant increase in the release of Cy5 was observed with 50 wt% HSA (from (22.0 ± 0.5)% to (27 ± 1)% of Cy5 in the dialysate). Furthermore, the release profiles of HES-HSA-TDI nanocapsules with a HSA content ranging from 5–50 wt% after trypsin treatment were plotted in one graph (Figure 54).

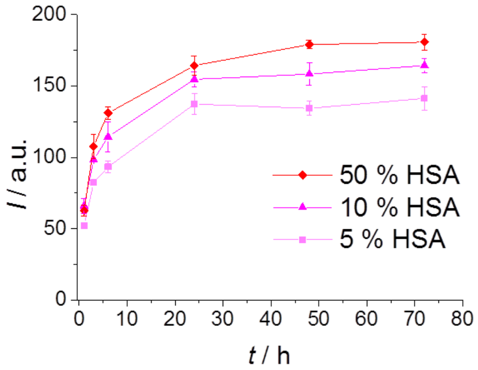

Figure 54: Effect of HSA ratio on the release of Cy5 after enzymatic degradation. With increasing amount of HSA, more Cy5 is released after enzymatic degradation using trypsin. The fluorescence intensity of Cy5 is plotted against the time of the dialysis. Prior to dialysis, the samples were treated with trypsin. The values presented are mean values and the error bars result from standard deviation from three fluorescence intensity measurements.

After the addition of trypsin, the release of Cy5 into the dialysate was found to increase from (21 ± 1)% of Cy5 for 5 wt% HSA to (26 ± 1)% for 10 wt.% HSA and to (27 ± 1)% for 50 wt% HSA in the dialysate after 72 h. Thus, more Cy5 was released during dialysis when more HSA was incorporated in the nanocapsules shell. As complementary experiments, another approach was investigated. Herein, the CellTracker Green dye was used as a sensor for enzymatic degradation. Indeed, as soon as the dye got in contact with degrading enzymes, fluorescence evolved.

4.4.4.3. Celltracker Green as Sensor for Enzymatic Degradation

CellTracker Green can be used as additional method to monitor the degradation of the nanocapsules. CellTracker Green becomes fluorescent upon scission of intramolecular ester bonds (Scheme 5). When the nanocontainers are degraded, CellTracker Green is released and digested by trypsin. This can be monitored by the upcoming fluorescence. In turn, when nanocontainers are prepared with a non-degradable material, CellTracker Green is shielded by the nanocontainer and no fluorescence should be observable.[76]

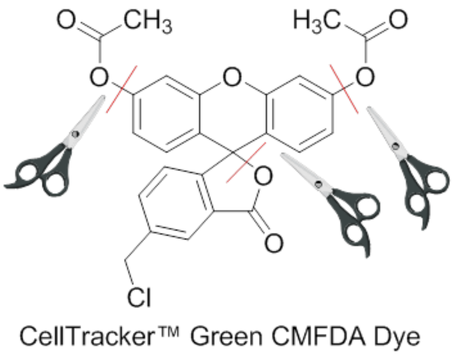

Scheme 5: Chemical structure of CellTracker Green CMFDA, a molecule that becomes fluorescent upon scission of ester bonds.

Nanocapsules filled with CellTracker Green have been prepared with different ratios of HES and HSA (0, 10, 50 and 100 wt% HSA). After purification by dialysis, the samples were treated with trypsin and the fluorescence was measured before as well as 3 h and 3 days after the treatment with trypsin (Figure 55).

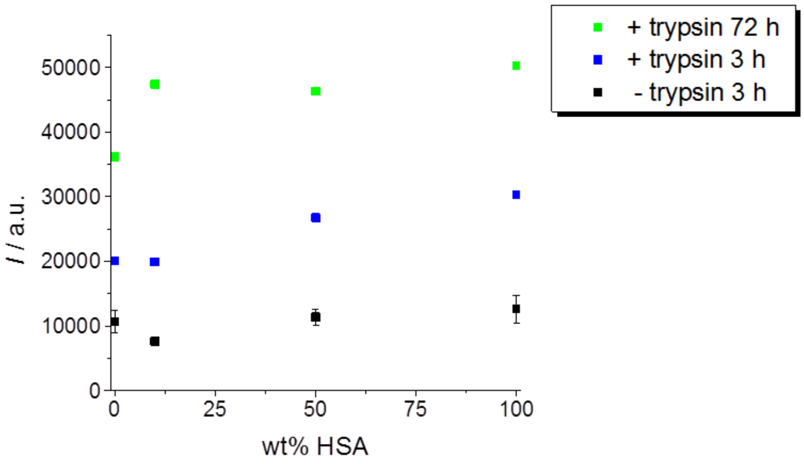

Figure 55: Effect of the HSA ratio on the fluorescence of CellTracker Green. The fluorescence intensity of CellTracker Green is plotted against the HSA content. With increasing amount of HSA in the nanocapsule shell, more CellTracker Green was converted in the fluorescent species upon addition of trypsin (blue). 72 h after the addition of trypsin (green), the fluorescence intensity was higher than after 3 h (blue). Values are normalized by solid content of nanocapsule dispersions.

To avoid the degradation of non-encapsulated CellTracker Green, the nanocapsules were purified via dialysis prior to the addition of trypsin. Even without treating the HES-HSA nanocapsules with trypsin, the CellTracker Green encapsulated in the nanocapsules was found to be fluorescent. This indicates a cleavage of the ester bonds in the CellTracker Green molecule without the presence of enzymes by hydrolysis of ester bonds in water.[243] Differences in the initial fluorescence intensity can be attributed to differences in the encapsulation efficiency and in the solid content. When trypsin was added to the nanocapsule dispersions, the fluorescence intensity increased for all the samples by a factor of 2–3. The fluorescence intensity increased with the amount of HSA in the nanocapsules (from 1.9 times increase in fluorescence intensity for 0 wt% HSA to a 2.4–2.6 times increase for 10 wt% HSA or more, ~30% more increase in fluorescence intensity when the nanocapsule shell was containing HSA). For 50 wt% of HSA, the fluorescence intensity was ~30% higher, for 100 wt% HSA ~50% higher compared to the fluorescence intensity of nanocapsules prepared with 0 or 10 wt% HSA after 3 h incubation time with trypsin. After 3 h, the scission of CellTracker Green was not completed. The fluorescence intensity was even higher (~2 times) after 3 days in the presence of trypsin for all nanocapsules (Figure 55). After 3 days in presence of trypsin, nanocapsules containing HSA were exhibiting a ~30% times higher increase in fluorescence intensity than the nanocapsules based on HES only. Over the time the fluorescence intensity of CellTracker Green increased also without any HSA moieties in the nanocapsule shell (see sample labeled as 0% HSA in Figure 55). This induces that trypsin is able to get into contact with the cargo entrapped into nanocapsules from pure HES-TDI or that hydrolysis of CellTracker Green in water is taking place and is accelerated at 37 °C in comparison to the hydrolysis at room temperature.

For the nanocapsules prepared from 50 wt% HES and 50 wt% HSA, the highest release of Cy5 (see Section 4.4.4.2) and the highest fluorescence intensity of Celltracker Green after 3 h incubation time with trypsin (~30% higher fluorescence intensity compared to lower amounts of HSA incorporated in the nanocapsule shell) were obtained. Therefore, this type of nanocapsules was chosen for the encapsulation of STAT3 inhibitors.

4.4.4.4. Encapsulation of STAT3 Inhibitors

The encapsulation of STAT3 inhibitors was achieved by dissolving them in DMSO and carefully mixing the solution with HSA dissolved in water. Subsequently, the synthesis was carried out *via* inverse miniemulsion. By addition of

TDI, cross-linking of HES and HSA was achieved and the STAT3 inhibitors were encapsulated into the nanocarriers. As a control, nanocapsules without STAT3 inhibitor but with Cy5 and CellTracker Green were synthesized. Figure 56 shows SEM micrographs revealing the formation of nanoparticles with a core-shell morphology. The structure of nanocapsules was collapsed due to the measurement conditions.

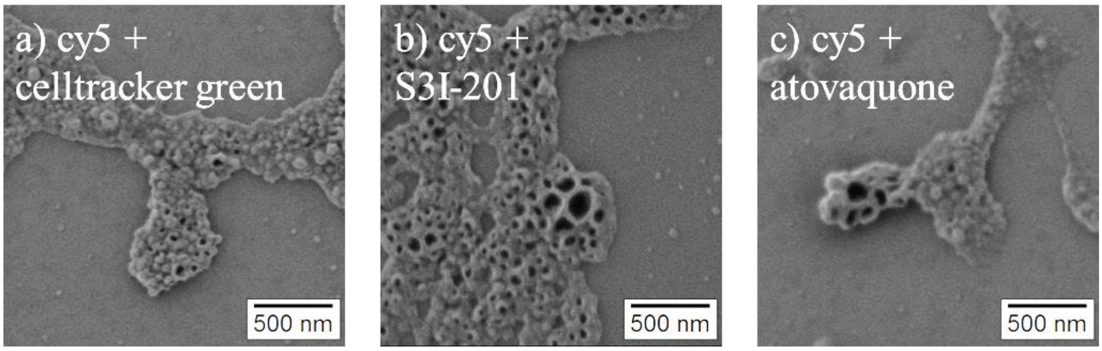

Figure 56: SEM of HES$_{50}$-HSA$_{50}$-TDI nanocapsules filled with a) Cy5 and CellTracker Green, b) Cy5 and S3I-201, and c) Cy5 and atovaquone. For all samples, nanocapsules with a core-shell morphology were observed.

The characteristics of the prepared samples are listed in Table 4. The hydrodynamic diameter was around 130 nm for the nanocapsules containing atovaquone and was similar to the diameter of nanocapsules prepared without STAT3 inhibitor. For the nanocapsules filled with S3I-201, the most abundant average value was ~200 nm in diameter. This diameter was larger than the diameter of the other samples and might be indicating the formation of agglomerates in dispersion. The encapsulation efficiency of Cy5 was calculated from the amount released during dialysis quantified by the fluorescence intensity. For all three samples, the encapsulation efficiency of Cy5 was found to be ~88%.

The amount of the STAT3 inhibitors was quantified *via* HPLC measurements. In the dialysate, no signal for atovaquone was observed. Consequently, 100% of atovaquone should be contained in the purified nanocapsule dispersion. For S3I-201, the encapsulation efficiency was calculated to be 38.7%. Interestingly, two signals were observed in the HPLC chromatogram of the dialysate of S3I-201 containing nanocapsules, implementing that a side product of S3I-201 formed during the nanocapsules synthesis. To validate the results from HPLC, the diffusion behavior during dialysis of the STAT3 inhibitors needed to be monitored. Furthermore, HPLC always requires a filtration of the sample prior to measurement. Thus, the amount of STAT3 inhibitor lost during the filtration step needed to be quantified.

Table 4: Characteristics of nanocapsules with STAT3 inhibitors. The table is listing the payload, that was encapsulated, the hydrodynamic diameter measured in cyclohexane $d_{h,CH}$ and in water $d_{h,H2O}$, the solid content and the zeta potential measured after completed purification by dialysis.

Payload	DLS				Solid content / %	Zeta potential / V
	$d_{h,CH}$ / nm	PDI	$d_{h,H2O}$ / nm	PDI		
Cy5 + CellTracker Green	130	0.32	130 (41.2%); 460 nm (58.8%)	-	0.64 ± 0.06	−14.8 ± 0.7
Cy5 + S3I-201	22 (0.8%); 60 (15.4%); 200 (83.8%)	-	30 (2.3%); 170 (97.7%)	-	0.610 ±0.004	−14.9 ± 0.6
Cy5 + Atovaquone	130	0.33	240	0.42	0.58 ± 0.02	−16 ± 1

To monitor cell uptake in HeLa cells FACS measurements were performed in cooperation with the AG Steinbrink at the University Medical Center Mainz (Figure 57). The cells were treated with the HES-HSA nanocapsules listed in Table 4.

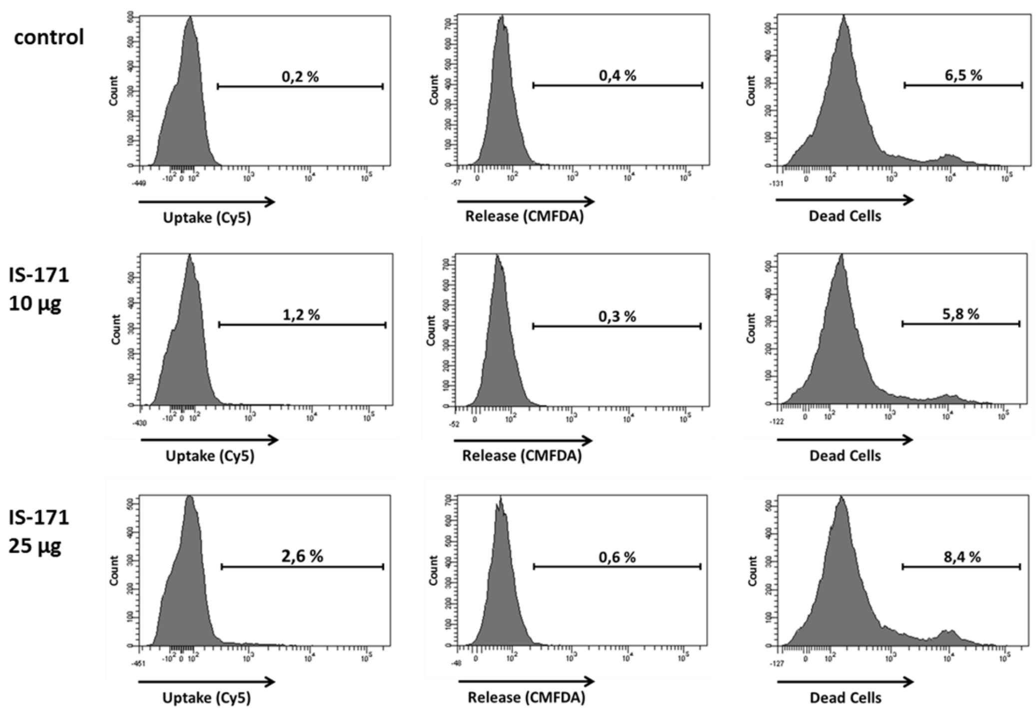

Figure 57: FACS measurements of cells treated with nanocapsules. The counts are plotted against the uptake of Cy5 (left), of CellTracker Green (middle), or against the viability of the nanocapsules (right). The top row is showing the control measurements. The middle row and the lower row represented two amounts of nanocapsule dispersion added to the cells. The cell experiments revealed no toxic effect of the nanocapsules. Neither Cy5 nor CellTracker Green was localized in cells.

The cell uptake of HES-HSA nanocapsules in HeLa cells was, with a maximum of 2.6% rather low compared to previous experiments with HES capsules (cell uptake ~50%, not shown). CellTracker Green starts to exhibit fluorescence upon enzymatic degradation. According to the low amount of nanocapsules located in the cells, only 0.6% of the cells were found to show a signal corresponding to the fluorescence of CellTracker Green. As most of the nanocapsules were not taken up by cells, no enzymatic triggered release was observed. The viability of the cells was unchanged after the treatment with nanocapsule dispersion in comparison to the control sample, indicating no toxicity of the nanocapsule dispersion.

4.4.5. Conclusions

DMSO was shown to slightly promote the uncontrolled release from nanocapsules. As a mixture of DMSO and water was needed to dissolve STAT3 inhibitors and HSA a ratio of 50% DMSO and 50% water (v/v) was chosen for the synthesis of HES-HSA-TDI nanocapsules. Upon enzymatic degradation, more fluorescent dye Cy5 was released when more HSA was incorporated in the nanocapsules shell (from (21 ± 1)% of Cy5 released after 72 h with 5 wt% HSA to (27 ± 1)% for 50 wt% HSA). Therefore, nanocapsules of 50 wt% HSA and 50 wt% HES were chosen to encapsulate STAT3 inhibitors. The content of STAT3 inhibitors in the nanocapsules was evaluated by HPLC and was found to be 37.8% for S3I-201 and ~100% for atovaquone. No cell uptake of the nanocapsules was observed in FACS measurements. The nanocapsules were found to be non-toxic in cell experiments.

A phase separation between HES and HSA might be occurring in the nanocapsules shell. The resulting microstructure in the nanocapsules shell is crucial for the release pathways available upon enzymatic degradation. To allow a specific cell uptake, targeting is needed, *e.g.*, by surface modification of the nanocarriers, as shown for HES nanocapsules with IL-2 linked to their surface.[244]

5. Summary

In the present thesis, we highlighted the diverse benefits of nanocapsules for non-invasive imaging and drug delivery. The issue of unwanted leakage from nanocapsules was addressed by the use of a semi-crystalline polymer as material for the nanocapsules shell. This improved system enabled the synthesis of highly loaded nanocarriers as contrast agents for magnetic resonance imaging (MRI). Aiming at even higher loadings, nanoparticles were designed as contrast agents for computed tomography (CT). Finally, the triggered release from the nanocarriers was addressed by incorporating predetermined breaking points into the nanocapsules shell.

Semi-crystalline nanocapsules were synthesized to enable a higher loading capacity in the nanocapsules. The nanocapsules shell was found to create a space confinement for the crystallization. The crystallization inside the nanocapsule shell differed from the crystallization in bulk in terms of degree of crystallinity and crystallization temperature. The degree of crystallinity was tuned by varying the shell thickness of the nanocapsules and by the molecular structure of the polymer. With increasing degree of crystallinity, the diffusion of a fluorescent dye, used as a model compound, was found to be reduced.

Semi-crystalline nanocapsules were used to encapsulate a commercial MRI contrast agent with remarkably high loading capacities (up to atheoretical contrast agent concentration inside the nanocapsules of ~0.2 mol L^{-1}) and a relaxivity as high as 40 s^{-1} $mmol^{-1}$ L. The nanocapsules were co-localized with the contrast agent and identified in cells by electron microscopy and energy dissipative X-ray spectroscopy (EDX). *In vivo* experiments and *ex vivo* biodistribution revealed liver and spleen as mainly targeted organs. The amount of contrast agent needed for the enhancement in tissue contrast was efficiently reduced by the encapsulation of the contrast agent into semi-crystalline nanocapsules compared to free contrast agent.

For CT measurements, even higher concentrations of contrast agents are required in comparison to MRI experiments. Nanoparticles containing a hydrophilic, commercial CT contrast agent were synthesized. The balance between entrapment efficiency and hydrophilicity was controlled to obtain the maximum iodine concentration in dispersion. Sonication helped to reduce agglomeration of the nanoparticles during the transfer step from cyclohexane to water. The interaction between iopromide containing nanoparticles and plasma was analyzed using DLS and SDS-PAGE.

To enable an enzymatic triggered release of cargos, proteins were incorporated into nanocapsules as predetermined breaking points. To avoid uncontrolled cell uptake, HES was chosen as basic material for the nanocapsules. The release of a dye upon enzymatic degradation was monitored. The more protein was incorporated into the nanocapsule shell, the more fluorescent dye was released during dialysis. STAT3 inhibitors were chosen as a model drug. Because STAT3 inhibitors are slightly soluble in water, DMSO was added to the dispersed phase. DMSO contained in the core of the nanocapsules was found to promote diffusion of the inhibitor outside the nanocapsules. Cell experiments revealed no toxicity and no cell uptake of the nanocapsules.

This thesis gives an insight in how nanocarriers can serve as contrast agents and as nanocarriers for drug delivery. The approach leading to higher encapsulation capacity was accompanied by insights in crystallization in the space confinement of nanocapsules shell. With this method, versatile and non-toxic nanoscale contrast agents were obtained. Furthermore, the nanocapsules can also serve as sensitive probes because the relaxivity of MRI contrast agents is strongly dependent on the water exchange in its environment. The nanocapsules were depicted *via* MRI/CT and detected *via* ICP-OES or EDX. This allows for following the fate of nanocapsules after cell uptake and the assessment of their biodistribution.

6. Zusammenfassung

In dieser Arbeit wurden die vielfältigen Vorteile von Nanokapseln für die biomedizinische Bildgebung und für den Wirkstofftransport hervorgehoben. Das Entweichen aus Nanokapseln wurde durch die Verwendung eines semikristallinen Polymers adressiert. Dieses verbesserte System ermöglichte die Synthese von Nanoträgersystemen mit hohem Fassungsvermögen als Kontrastmittel für Magnetresonanztomographie (MRT). Mit noch höheren Fassungsvermögen wurden Nanopartikel als Kontrastmittel für die Computertomographie (CT) entworfen. Letztendlich wurde die gezielte Freisetzung aus den Nanoträgern durch den Einbau von Sollbruchstellen in die Nanokapselschale ermöglicht.

Zur Erhöhung des Fassungsvermögens wurden semikristalline Nanokapseln hergestellt. Die Kristallisation des Schalen bildenden Polymers ist auf das Innere der Nanokapselschale begrenzt. Diese räumliche Begrenzung hat zur Folge, dass sich die Kristallisation des Polymers in der Nanokapselschale in ihrem Kristallinitätsgrad und in ihrer Kristallisationstemperatur von der Kristallisation in Substanz unterscheidet. Der Kristallinitätsgrad wurde durch Variieren der Schalendicke sowie durch die Molekülstruktur des Polymers modifiziert. Zur Feststellung des Diffusionsverhaltens wurde ein Fluoreszenzfarbstoffs als Modellverbindung verwendet. Mit zunehmenden Kristallinitätsgrad nahm die Diffusion des Fluoreszenzfarbstoffes ab.

Semikristalline Nanokapseln wurden verwendet, um ein kommerzielles MRT-Kontrastmittel zu verkapseln. Die Nanokapseln zeichnen sich durch ein bemerkenswert hohes Fassungsvermögen aus (bis zu einer theoretischen Kontrastmittelkonzentration von~0,2 mol L^{-1} Gd im Inneren der Kapsel) und einer Relaxivität von bis zu 40 s^{-1} $mmol^{-1}$ L. Das Kontrastmittel wurde mittels Elektronenmikroskopie und Energie dissipativer Röntgenspektroskopie (EDX) in den Nanokapseln identifiziert und co-lokalisiert. *In vivo*-Experimente und *ex vivo*-Biodistribution identifizierten Leber und Milz als hauptsächliche Zielorgane der Nanokapseln. Die für die Verbesserung des Bildkontrasts im MRT benötigte Menge an Kontrastmitteln wurde durch dessen Verkapselung in semikristalline Nanokapseln im Vergleich zu freiem Kontrastmittel effizient reduziert.

Für CT werden noch höhere Kontrastmittelmengen benötigt als beim MRT. Es wurden Nanopartikel synthetisiert, die ein hydrophiles, handelsübliches CT-

Kontrastmittel enthalten. Die Einschlusseffizienz und die Hydrophilie der Nanopartikel wurden abgestimmt, um eine maximale Iodkonzentration in der Nanopartikel Suspension zu erhalten. Mittels Ultraschallbehandlung konnte die Bildung von Agglomeraten während des Transfers der Nanopartikel aus Cyclohexan in Wasser reduziert werden. Im Hinblick auf eine mögliche biomedizinische Anwendung wurde die Wechselwirkung zwischen den Iopromid enthaltenden Nanopartikeln und Plasma unter Verwendung von DLS und SDS-PAGE analysiert.

Um eine enzymatische Freisetzung zu ermöglichen wurden Proteine als Sollbruchstellen in die Nanokapselschale eingebaut. Zur Vermeidung einer unkontrollierten Zellaufnahme wurde Hydroxyethylstärke als Ausgangsmaterial für die Nanokapseln gewählt. Die Freisetzung nach enzymatischem Abbau wurde unter Verwendung eines Fluoreszenzfarbstoffs als Modellverbindung überwacht. Je mehr Protein in die Schale der Nanokapseln eingebaut wurde, desto mehr Fluoreszenzfarbstoff wurde während der Dialyse freigesetzt. STAT3-Inhibitoren wurden als Modellbeispiele für Arzneimittel ausgewählt. Da die Wasserlöslichkeit von STAT3-Inhibitoren gering ist, wurde der dispergierten Phase DMSO zugesetzt. Die Auswirkung der Menge an DMSO im Kern der Nanokapseln auf die Diffusion wurde untersucht. DMSO begünstigt die Diffusion durch die Kapselwand. Zellversuche mit HeLa Zellen zeigten keine Toxizität und keine Zellaufnahme der Nanokapseln.

Diese Dissertation gab einen Einblick darüber, wie Nanoträgersysteme als Kontrastmittel und als Nanoträger für den Wirkstofftransport dienen können. Das Vorhaben, die Grenzen des Fassungsvermögens der Nanokapseln zu erweitern, wurde begleitet von Einsichten in die Kristallisation innerhalb der Nanokapselschale. Neben dem Gewinn von neuen, nicht-toxischen, nanoskaligen Kontrastmitteln sowie Nanoträgersystemen für den Wirkstofftransport, können die Nanokapseln zukünftig auch als Sonden eingesetzt werden, um beispielsweise Unterschiede in der Wasserdiffusion anhand der Relaxivität zu detektieren. Dabei können die Nanokapseln mittels MRT oder CT abgebildet und über ICP-OES oder EDX identifiziert werden. Dies eröffnet die Möglichkeit, weitere Erkenntnisse in Bereichen wie z. B. der Zelleaufnahme oder Biodistribution zu gewinnen.

Literature

1. Siegel, R. L.; Miller, K. D.; Jemal, A. Cancer statistics, 2017. *CA Cancer J. Clin.* **2017**, 67, 7-30.
2. Miller, K. D.; Siegel, R. L.; Lin, C. C.; Mariotto, A. B.; Kramer, J. L.; Rowland, J. H.; Stein, K. D.; Alteri, R.; Jemal, A. Cancer treatment and survivorship statistics, 2016. *CA Cancer J. Clin.* **2016**, 66, 271-289.
3. Lee, N.; Choi, S. H.; Hyeon, T. Nano-Sized CT Contrast Agents. *Adv. Mater.* **2013**, 25, 2641-2660.
4. Bui, T.; Stevenson, J.; Hoekman, J.; Zhang, S.; Maravilla, K.; Ho, R. J. Y. Novel Gd Nanoparticles Enhance Vascular Contrast for High-Resolution Magnetic Resonance Imaging. *PLoS ONE* **2010**, 5, e13082.
5. Caravan, P.; Ellison, J. J.; McMurry, T. J.; Lauffer, R. B. Gadolinium(III) Chelates as MRI Contrast Agents: Structure, Dynamics, and Applications. *Chem. Rev.* **1999**, 99, 2293-2352.
6. Xue, H. Y.; Liu, S.; Wong, H. L. Nanotoxicity: a key obstacle to clinical translation of siRNA-based nanomedicine. *Nanomedicine* **2014**, 9, 295-312.
7. Lusic, H.; Grinstaff, M. W. X-Ray Computed Tomography Contrast Agents. *Chem. Rev.* **2013**, 113, 10.1021/cr200358s.
8. Kang, B.; Okwieka, P.; Schöttler, S.; Seifert, O.; Kontermann, R. E.; Pfizenmaier, K.; Musyanovych, A.; Meyer, R.; Diken, M.; Sahin, U.; Mailänder, V.; Wurm, F. R.; Landfester, K. Tailoring the stealth properties of biocompatible polysaccharide nanocontainers. *Biomaterials* **2015**, 49, 125-134.
9. Malzahn, K.; Ebert, S.; Schlegel, I.; Neudert, O.; Wagner, M.; Schütz, G.; Ide, A.; Roohi, F.; Münnemann, K.; Crespy, D.; Landfester, K. Design and Control of Nanoconfinement to Achieve Magnetic Resonance Contrast Agents with High Relaxivity. *Adv. Healthc. Mater.* **2016**, 5, 567-574.
10. Harisinghani, M. G.; Barentsz, J.; Hahn, P. F.; Deserno, W. M.; Tabatabaei, S.; van de Kaa, C. H.; de la Rosette, J.; Weissleder, R. Noninvasive Detection of Clinically Occult Lymph-Node Metastases in Prostate Cancer. *New Engl. J. Med.* **2003**, 348, 2491-2499.
11. Willmann, J. K.; van Bruggen, N.; Dinkelborg, L. M.; Gambhir, S. S. Molecular imaging in drug development. *Nat. Rev. Drug Discov.* **2008**, 7, 591-607.
12. Vert, M.; Doi, Y.; Hellwich, K.-H.; Hess, M.; Hodge, P.; Kubisa, P.; Rinaudo, M.; Schué, F. Terminology for biorelated polymers and applications (IUPAC Recommendations 2012). *Pure Appl. Chem.* **2012**, 84, 377-410.
13. D'Aniello, C.; Guadagno, L.; Gorrasi, G.; Vittoria, V. Influence of the crystallinity on the transport properties of isotactic polypropylene. *Polymer* **2000**, 41, 2515-2519.
14. Pappenheimer, J.; Renkin, E.; Borrero, L. Filtration, diffusion and molecular sieving through peripheral capillary membranes. *Am. J. Physiol.* **1951**, 167, 13-46.
15. Peterlin, A. Dependence of diffusive transport on morphology of crystalline polymers. *J. Macromol. Sci., B* **1975**, 11, 57-87.
16. Renkin, E. M. Filtration, Diffusion, and Molecular Sieving Through Porous Cellulose Membranes. *J. Gen. Physiol.* **1954**, 38, 225-243.
17. Duan, Z.; Thomas, N. L. Water vapour permeability of poly(lactic acid): Crystallinity and the tortuous path model. *J. Appl. Phys.* **2014**, 115, 064903.
18. Michaels, A. S.; Vieth, W. R.; Barrie, J. A. Solution of Gases in Polyethylene Terephthalate. *J. Appl. Phys.* **1963**, 34, 1-12.
19. Michaels, A. S.; Vieth, W. R.; Barrie, J. A. Diffusion of Gases in Polyethylene Terephthalate. *J. Appl. Phys.* **1963**, 34, 13-20.
20. Suzuki, Y.; Steinhart, M.; Kappl, M.; Butt, H.-J.; Floudas, G. Effects of polydispersity,

additives, impurities and surfaces on the crystallization of poly(ethylene oxide)(PEO) confined to nanoporous alumina. *Polymer* **2016**, 99, 273-280.

21. Murray, B. J.; Knopf, D. A.; Bertram, A. K. The formation of cubic ice under conditions relevant to Earth's atmosphere. *Nature* **2005**, 434, 202-205.

22. Tabazadeh, A.; Djikaev, Y. S.; Reiss, H. Surface crystallization of supercooled water in clouds. *Proc. Natl. Acad. Sci. U.S.A.* **2002**, 99, 15873-15878.

23. Johnston, J. C.; Molinero, V. Crystallization, melting, and structure of water nanoparticles at atmospherically relevant temperatures. *J. Am. Chem. Soc.* **2012**, 134, 6650-6659.

24. Suzuki, Y.; Duran, H.; Steinhart, M.; Butt, H.-J.; Floudas, G. Homogeneous crystallization and local dynamics of poly(ethylene oxide) (PEO) confined to nanoporous alumina. *Soft Matter* **2013**, 9, 2621-2628.

25. Zhang, X. X.; Fan, Y. F.; Tao, X. M.; Yick, K. L. Fabrication and properties of microcapsules and nanocapsules containing n-octadecane. *Mater. Chem. Phys.* **2004**, 88, 300-307.

26. Schneider, S.; Gompper, G. Shapes of crystalline domains on spherical fluid vesicles. *Europhys. Lett.* **2005**, 70, 136.

27. Kox, A. J. The discovery of the electron: II. The Zeeman effect. *Eur. J. Phys.* **1997**, 18, 139.

28. Purcell, E. M.; Torrey, H. C.; Pound, R. V. Resonance Absorption by Nuclear Magnetic Moments in a Solid. *Phys. Rev.* **1946**, 69, 37-38.

29. Bloch, F.; Hansen, W. W.; Packard, M. The Nuclear Induction Experiment. *Phys. Rev.* **1946**, 70, 474-485.

30. Bloch, F. Nuclear induction. *Phys. Rev.* **1946**, 70, 460.

31. Meiboom, S.; Gill, D. Modified Spin-Echo Method for Measuring Nuclear Relaxation Times. *Rev. Sci. Instrum.* **1958**, 29, 688-691.

32. Reimer, P.; Parizel, P. M.; Meaney, J. F.; Stichnoth, F. A. *Clinical MR imaging*. Springer: 2010.

33. Ranganathan, R. S.; Raju, N.; Fan, H.; Zhang, X.; Tweedle, M. F.; Desreux, J. F.; Jacques, V. Polymethylated DOTA Ligands. 2. Synthesis of Rigidified Lanthanide Chelates and Studies on the Effect of Alkyl Substitution on Conformational Mobility and Relaxivity. *Inorg. Chem.* **2002**, 41, 6856-6866.

34. Tóth, É.; Helm, L.; Merbach, A. Relaxivity of MRI Contrast Agents. In *Contrast Agents I*, Krause, W., Ed. Springer Berlin Heidelberg: 2002; Vol. 221, pp 61-101.

35. Bloembergen, N.; Purcell, E. M.; Pound, R. V. Relaxation Effects in Nuclear Magnetic Resonance Absorption. *Phys. Rev.* **1948**, 73, 679-712.

36. Solomon, I. Relaxation Processes in a System of Two Spins. *Phys. Rev.* **1955**, 99, 559-565.

37. Bloembergen, N. Proton Relaxation Times in Paramagnetic Solutions. *J. Chem. Phys.* **1957**, 27, 572-573.

38. Bloembergen, N.; Morgan, L. O. Proton Relaxation Times in Paramagnetic Solutions. Effects of Electron Spin Relaxation. *J. Chem. Phys.* **1961**, 34, 842-850.

39. Bernheim, R. A.; Brown, T. H.; Gutowsky, H. S.; Woessner, D. E. Temperature Dependence of Proton Relaxation Times in Aqueous Solutions of Paramagnetic Ions. *J. Chem. Phys.* **1959**, 30, 950-956.

40. Nicolle, G. M.; Tóth, É.; Schmitt-Willich, H.; Radüchel, B.; Merbach, A. E. The Impact of Rigidity and Water Exchange on the Relaxivity of a Dendritic MRI Contrast Agent. *Chem. Eur. J.* **2002**, 8, 1040-1048.

41. Hwang, L. P.; Freed, J. H. Dynamic effects of pair correlation functions on spin relaxation by translational diffusion in liquids. *J. Chem. Phys.* **1975**, 63, 4017-4025.

42. Davis, J. J.; Huang, W.-Y.; Davies, G.-L. Location-tuned relaxivity in Gd-doped

mesoporous silica nanoparticles. *J. Mater. Chem.* **2012**, 22, 22848-22850.
43. Schlegel, I.; Muñoz-Espí, R.; Renz, P.; Lieberwirth, I.; Floudas, G.; Suzuki, Y.; Crespy, D.; Landfester, K. Crystallinity Tunes Permeability of Polymer Nanocapsules. *Macromolecules* **2017**, 50, 4725-4732.
44. Ananta, J. S.; Godin, B.; Sethi, R.; Moriggi, L.; Liu, X.; Serda, R. E.; Krishnamurthy, R.; Muthupillai, R.; Bolskar, R. D.; Helm, L.; Ferrari, M.; Wilson, L. J.; Decuzzi, P. Geometrical confinement of gadolinium-based contrast agents in nanoporous particles enhances T1 contrast. *Nat. Nanotech.* **2010**, 5, 815-821.
45. Moghimi, S. M.; Hunter, A. C.; Murray, J. C. Long-Circulating and Target-Specific Nanoparticles: Theory to Practice. *Pharmacol. Rev.* **2001**, 53, 283-318.
46. Gries, H. Extracellular MRI Contrast Agents Based on Gadolinium. In *Contrast Agents I: Magnetic Resonance Imaging*, Krause, W., Ed. Springer Berlin Heidelberg: Berlin, Heidelberg, 2002; pp 1-24.
47. Vogler, H.; Platzek, J.; Schuhmann-Giampieri, G.; Frenzel, T.; Weinmann, H.-J.; Radüchel, B.; Press, W.-R. Pre-clinical evaluation of gadobutrol: a new, neutral, extracellular contrast agent for magnetic resonance imaging. *Eur. J. Radiol.* **1995**, 21, 1-10.
48. Gao, Z.; Ma, T.; Zhao, E.; Docter, D.; Yang, W.; Stauber, R. H.; Gao, M. Small is Smarter: Nano MRI Contrast Agents – Advantages and Recent Achievements. *Small* **2015**, n/a-n/a.
49. Chen, F.; Bu, W.; Zhang, S.; Liu, X.; Liu, J.; Xing, H.; Xiao, Q.; Zhou, L.; Peng, W.; Wang, L.; Shi, J. Positive and Negative Lattice Shielding Effects Co-existing in Gd (III) Ion Doped Bifunctional Upconversion Nanoprobes. *Adv. Funct. Mater.* **2011**, 21, 4285-4294.
50. Röntgen, W. C. Ueber eine neue Art von Strahlen. *Ann. Phys.* **1898**, 300, 1-11.
51. Kanal, E.; Shellock, F. G.; Talagala, L. Safety considerations in MR imaging. *Radiology* **1990**, 176, 593-606.
52. Hargreaves, B. A.; Worters, P. W.; Pauly, K. B.; Pauly, J. M.; Koch, K. M.; Gold, G. E. Metal-Induced Artifacts in MRI. *Am. J. Roentgenol.* **2011**, 197, 547-555.
53. Yu, S.-B.; Watson, A. D. Metal-Based X-ray Contrast Media. *Chem. Rev.* **1999**, 99, 2353-2378.
54. Esser-Kahn, A. P.; Odom, S. A.; Sottos, N. R.; White, S. R.; Moore, J. S. Triggered Release from Polymer Capsules. *Macromolecules* **2011**, 44, 5539-5553.
55. Casasús, R.; Marcos, M. D.; Martínez-Máñez, R.; Ros-Lis, J. V.; Soto, J.; Villaescusa, L. A.; Amorós, P.; Beltrán, D.; Guillem, C.; Latorre, J. Toward the Development of Ionically Controlled Nanoscopic Molecular Gates. *J. Am. Chem. Soc.* **2004**, 126, 8612-8613.
56. Casasús, R.; Climent, E.; Marcos, M. D.; Martínez-Máñez, R.; Sancenón, F.; Soto, J.; Amorós, P.; Cano, J.; Ruiz, E. Dual Aperture Control on pH- and Anion-Driven Supramolecular Nanoscopic Hybrid Gate-like Ensembles. *J. Am. Chem. Soc.* **2008**, 130, 1903-1917.
57. Angelos, S.; Yang, Y.-W.; Patel, K.; Stoddart, J. F.; Zink, J. I. pH-Responsive Supramolecular Nanovalves Based on Cucurbit[6]uril Pseudorotaxanes. *Angew. Chem.* **2008**, 120, 2254-2258.
58. Park, C.; Oh, K.; Lee, S. C.; Kim, C. Controlled Release of Guest Molecules from Mesoporous Silica Particles Based on a pH-Responsive Polypseudorotaxane Motif. *Angew. Chem. Int. Ed.* **2007**, 46, 1455-1457.
59. Muhammad, F.; Guo, M.; Qi, W.; Sun, F.; Wang, A.; Guo, Y.; Zhu, G. pH-Triggered Controlled Drug Release from Mesoporous Silica Nanoparticles via Intracelluar Dissolution of ZnO Nanolids. *J. Am. Chem. Soc.* **2011**, 133, 8778-8781.
60. Zhang, Q.; Ariga, K.; Okabe, A.; Aida, T. A Condensable Amphiphile with a Cleavable Tail as a “Lizard” Template for the Sol−Gel Synthesis of Functionalized Mesoporous Silica. *J. Am. Chem. Soc.* **2004**, 126, 988-989.
61. Schlossbauer, A.; Dohmen, C.; Schaffert, D.; Wagner, E.; Bein, T. pH-Responsive

Release of Acetal-Linked Melittin from SBA-15 Mesoporous Silica. *Angew. Chem. Int. Ed.* **2011**, 50, 6828-6830.

62. Liu, R.; Zhang, Y.; Zhao, X.; Agarwal, A.; Mueller, L. J.; Feng, P. pH-Responsive Nanogated Ensemble Based on Gold-Capped Mesoporous Silica through an Acid-Labile Acetal Linker. *J. Am. Chem. Soc.* **2010**, 132, 1500-1501.

63. Aznar, E.; Marcos, M. D.; Martínez-Máñez, R.; Sancenón, F.; Soto, J.; Amorós, P.; Guillem, C. pH- and Photo-Switched Release of Guest Molecules from Mesoporous Silica Supports. *J. Am. Chem. Soc.* **2009**, 131, 6833-6843.

64. Riedinger, A.; Guardia, P.; Curcio, A.; Garcia, M. A.; Cingolani, R.; Manna, L.; Pellegrino, T. Subnanometer local temperature probing and remotely controlled drug release based on azo-functionalized iron oxide nanoparticles. *Nano Lett.* **2013**, 13, 2399-2406.

65. McClure, J. H.; Robertson, R. E.; Cuthbertson, A. C. The Decomposition of Benzoyl Peroxide in Benzene. *Can. J. Res.* **1942**, 20b, 103-113.

66. Thomas, C. R.; Ferris, D. P.; Lee, J.-H.; Choi, E.; Cho, M. H.; Kim, E. S.; Stoddart, J. F.; Shin, J.-S.; Cheon, J.; Zink, J. I. Noninvasive Remote-Controlled Release of Drug Molecules in Vitro Using Magnetic Actuation of Mechanized Nanoparticles. *J. Am. Chem. Soc.* **2010**, 132, 10623-10625.

67. Aznar, E.; Mondragón, L.; Ros-Lis, J. V.; Sancenón, F.; Marcos, M. D.; Martínez-Máñez, R.; Soto, J.; Pérez-Payá, E.; Amorós, P. Finely Tuned Temperature-Controlled Cargo Release Using Paraffin-Capped Mesoporous Silica Nanoparticles. *Angew. Chem. Int. Ed.* **2011**, 50, 11172-11175.

68. Zhang, J.; Misra, R. D. K. Magnetic drug-targeting carrier encapsulated with thermosensitive smart polymer: Core–shell nanoparticle carrier and drug release response. *Acta Biomater.* **2007**, 3, 838-850.

69. Ferris, D. P.; Zhao, Y.-L.; Khashab, N. M.; Khatib, H. A.; Stoddart, J. F.; Zink, J. I. Light-Operated Mechanized Nanoparticles. *J. Am. Chem. Soc.* **2009**, 131, 1686-1688.

70. Mal, N. K.; Fujiwara, M.; Tanaka, Y. Photocontrolled reversible release of guest molecules from coumarin-modified mesoporous silica. *Nature* **2003**, 421, 350-353.

71. Fujiwara, M.; Terashima, S.; Endo, Y.; Shiokawa, K.; Ohue, H. Switching catalytic reaction conducted in pore void of mesoporous material by redox gate control. *Chem. Commun.* **2006**, 4635-4637.

72. Lai, C.-Y.; Trewyn, B. G.; Jeftinija, D. M.; Jeftinija, K.; Xu, S.; Jeftinija, S.; Lin, V. S. Y. A Mesoporous Silica Nanosphere-Based Carrier System with Chemically Removable CdS Nanoparticle Caps for Stimuli-Responsive Controlled Release of Neurotransmitters and Drug Molecules. *J. Am. Chem. Soc.* **2003**, 125, 4451-4459.

73. Behzadi, S.; Steinmann, M.; Estupiñán, D.; Landfester, K.; Crespy, D. The pro-active payload strategy significantly increases selective release from mesoporous nanocapsules. *J. Control. Release* **2016**, 242, 119-125.

74. Hernandez, R.; Tseng, H.-R.; Wong, J. W.; Stoddart, J. F.; Zink, J. I. An Operational Supramolecular Nanovalve. *J. Am. Chem. Soc.* **2004**, 126, 3370-3371.

75. Schlossbauer, A.; Kecht, J.; Bein, T. Biotin–Avidin as a Protease-Responsive Cap System for Controlled Guest Release from Colloidal Mesoporous Silica. *Angew. Chem. Int. Ed.* **2009**, 48, 3092-3095.

76. Piradashvili, K.; Fichter, M.; Mohr, K.; Gehring, S.; Wurm, F. R.; Landfester, K. Biodegradable Protein Nanocontainers. *Biomacromolecules* **2015**, 16, 815-821.

77. Agostini, A.; Mondragón, L.; Coll, C.; Aznar, E.; Marcos, M. D.; Martínez-Máñez, R.; Sancenón, F.; Soto, J.; Pérez-Payá, E.; Amorós, P. Dual Enzyme-Triggered Controlled Release on Capped Nanometric Silica Mesoporous Supports. *ChemistryOpen* **2012**, 1, 17-20.

78. Greenfield, S. Plasma spectroscopy comes of age. *Pure Appl. Chem.* **1980**, 52, 2509-2523.

79. Greenfield, S.; Jones, I. L.; Berry, C. High-pressure plasmas as spectroscopic emission sources. *Analyst* **1964**, 89, 713-720.

80. Manning, T. J.; Grow, W. R. Inductively Coupled Plasma - Atomic Emission Spectrometry. *Chem. Educator* **1997**, 2, 1-19.

81. Truitt, D.; Robinson, J. W. Spectroscopic studies of organic compounds introduced into a radiofrequency induced plasma. *Anal. Chim. Acta* **1970**, 51, 61-67.

82. Nölte, J. *ICP Emissionsspektrometrie für Praktiker: Grundlagen, Methodenentwicklung, Anwendungsbeispiele*. John Wiley & Sons: 2012.

83. Axenrod, T.; Ceccarelli, G. *NMR in living systems*. Springer Science & Business Media: 2012; Vol. 164.

84. Breitmaier, E.; Spohn, K.-H.; Berger, S. 13C Spin-Lattice Relaxation Times and the Mobility of Organic Molecules in Solution. *Angew. Chem. Int. Ed. Engl.* **1975**, 14, 144-159.

85. Hahn, E. L. Spin echoes. *Phys. Rev.* **1950**, 80, 580.

86. Mailander, V.; Landfester, K. Interaction of nanoparticles with cells. *Biomacromolecules* **2009**, 10, 2379-2400.

87. Schärtl, W. *Light scattering from polymer solutions and nanoparticle dispersions*. Springer: Berlin, 2007.

88. Einstein, A. *Investigations on the Theory of the Brownian Movement*. Courier Corporation: 1956.

89. Particle Sizing Systems. Nicomp 380 Submicron Particle Sizer. https://www.laboratorynetwork.com/doc/nicomp-380-submicron-particle-sizer-0001 accessed 05 July, 2017.

90. Brar, S. K.; Verma, M. Measurement of nanoparticles by light-scattering techniques. *TrAC, Trends Anal. Chem.* **2011**, 30, 4-17.

91. Brigger, I.; Dubernet, C.; Couvreur, P. Nanoparticles in cancer therapy and diagnosis. *Adv. Drug Del. Rev.* **2002**, 54, 631-651.

92. Crespy, D.; Lv, L. P.; Landfester, K. Redefining the functions of nanocapsule materials. *Nanoscale Horiz.* **2016**, 1, 268-271.

93. Huang, X.; Voit, B. Progress on multi-compartment polymeric capsules. *Polym. Chem.* **2013**, 4, 435-443.

94. Slowing, I. I.; Trewyn, B. G.; Giri, S.; Lin, V. S. Y. Mesoporous Silica Nanoparticles for Drug Delivery and Biosensing Applications. *Adv. Funct. Mater.* **2007**, 17, 1225-1236.

95. Chen, F.; Hong, H.; Shi, S.; Goel, S.; Valdovinos, H. F.; Hernandez, R.; Theuer, C. P.; Barnhart, T. E.; Cai, W. Engineering of Hollow Mesoporous Silica Nanoparticles for Remarkably Enhanced Tumor Active Targeting Efficacy. *Sci. Rep.* **2014**, 4, 5080.

96. Yan, M.; Du, J.; Gu, Z.; Liang, M.; Hu, Y.; Zhang, W.; Priceman, S.; Wu, L.; Zhou, Z. H.; Liu, Z.; Segura, T.; Tang, Y.; Lu, Y. A novel intracellular protein delivery platform based on single-protein nanocapsules. *Nat. Nanotech.* **2010**, 5, 48-53.

97. Itoh, Y.; Matsusaki, M.; Kida, T.; Akashi, M. Enzyme-Responsive Release of Encapsulated Proteins from Biodegradable Hollow Capsules. *Biomacromolecules* **2006**, 7, 2715-2718.

98. He, W.; Parowatkin, M.; Mailänder, V.; Flechtner-Mors, M.; Graf, R.; Best, A.; Koynov, K.; Mohr, K.; Ziener, U.; Landfester, K.; Crespy, D. Nanocarrier for Oral Peptide Delivery Produced by Polyelectrolyte Complexation in Nanoconfinement. *Biomacromolecules* **2015**, 16, 2282-2287.

99. Tang, R.; Kim, C. S.; Solfiell, D. J.; Rana, S.; Mout, R.; Velázquez-Delgado, E. M.; Chompoosor, A.; Jeong, Y.; Yan, B.; Zhu, Z.-J.; Kim, C.; Hardy, J. A.; Rotello, V. M. Direct Delivery of Functional Proteins and Enzymes to the Cytosol Using Nanoparticle-Stabilized Nanocapsules. *ACS Nano* **2013**, 7, 6667-6673.

100. Giacalone, G.; Bochot, A.; Fattal, E.; Hillaireau, H. Drug-Induced Nanocarrier Assembly as a Strategy for the Cellular Delivery of Nucleotides and Nucleotide Analogues.

Biomacromolecules **2013**, 14, 737-742.

101. Kedracki, D.; Maroni, P.; Schlaad, H.; Vebert-Nardin, C. Polymer–Aptamer Hybrid Emulsion Templating Yields Bioresponsive Nanocapsules. *Adv. Funct. Mater.* **2014**, 24, 1133-1139.

102. Chen, Y.; Chen, H.; Zeng, D.; Tian, Y.; Chen, F.; Feng, J.; Shi, J. Core/Shell Structured Hollow Mesoporous Nanocapsules: A Potential Platform for Simultaneous Cell Imaging and Anticancer Drug Delivery. *ACS Nano* **2010**, 4, 6001-6013.

103. Kang, X.; Cheng, Z.; Yang, D.; Ma, P. a.; Shang, M.; Peng, C.; Dai, Y.; Lin, J. Design and Synthesis of Multifunctional Drug Carriers Based on Luminescent Rattle-Type Mesoporous Silica Microspheres with a Thermosensitive Hydrogel as a Controlled Switch. *Adv. Funct. Mater.* **2012**, 22, 1470-1481.

104. Wu, H.; Zhang, S.; Zhang, J.; Liu, G.; Shi, J.; Zhang, L.; Cui, X.; Ruan, M.; He, Q.; Bu, W. A Hollow-Core, Magnetic, and Mesoporous Double-Shell Nanostructure: In Situ Decomposition/Reduction Synthesis, Bioimaging, and Drug-Delivery Properties. *Adv. Funct. Mater.* **2011**, 21, 1850-1862.

105. Chen, Y.; Chen, H.; Sun, Y.; Zheng, Y.; Zeng, D.; Li, F.; Zhang, S.; Wang, X.; Zhang, K.; Ma, M.; He, Q.; Zhang, L.; Shi, J. Multifunctional Mesoporous Composite Nanocapsules for Highly Efficient MRI-Guided High-Intensity Focused Ultrasound Cancer Surgery. *Angew. Chem. Int. Ed.* **2011**, 50, 12505-12509.

106. Zhao, Y.; Lv, L.-P.; Jiang, S.; Landfester, K.; Crespy, D. Advanced stimuli-responsive polymer nanocapsules with enhanced capabilities for payloads delivery. *Polym. Chem.* **2015**, 6, 4197-4205.

107. Kremer, F. *Dynamics in geometrical confinement*. Springer: 2014.

108. Zhang, Q.; Wang, M.; Wooley, K. L. Nanoscopic confinement of semi-crystalline polymers. *Curr. Org. Chem.* **2005**, 9, 1053-1066.

109. Shin, K.; Obukhov, S.; Chen, J.-T.; Huh, J.; Hwang, Y.; Mok, S.; Dobriyal, P.; Thiyagarajan, P.; Russell, T. P. Enhanced mobility of confined polymers. *Nat. Mater.* **2007**, 6, 961-965.

110. Michell, R. M.; Lorenzo, A. T.; Müller, A. J.; Lin, M.-C.; Chen, H.-L.; Blaszczyk-Lezak, I.; Martin, J.; Mijangos, C. The crystallization of confined polymers and block copolymers infiltrated within alumina nanotube templates. *Macromolecules* **2012**, 45, 1517-1528.

111. Duran, H.; Steinhart, M.; Butt, H.-J. r.; Floudas, G. From heterogeneous to homogeneous nucleation of isotactic poly (propylene) confined to nanoporous alumina. *Nano Lett.* **2011**, 11, 1671-1675.

112. Guan, Y.; Liu, G.; Gao, P.; Li, L.; Ding, G.; Wang, D. Manipulating crystal orientation of poly (ethylene oxide) by nanopores. *ACS Macro Lett.* **2013**, 2, 181-184.

113. Taden, A.; Landfester, K. Crystallization of poly (ethylene oxide) confined in miniemulsion droplets. *Macromolecules* **2003**, 36, 4037-4041.

114. Staff, R. H.; Lieberwirth, I.; Landfester, K.; Crespy, D. Preparation and Characterization of Anisotropic Submicron Particles From Semicrystalline Polymers. *Macromol. Chem. Phys.* **2012**, 213, 351-358.

115. Yadav, S. K.; Khilar, K. C.; Suresh, A. K. Release rates from semi-crystalline polymer microcapsules formed by interfacial polycondensation. *J. Membr. Sci.* **1997**, 125, 213-218.

116. Torino, E.; Aruta, R.; Sibillano, T.; Giannini, C.; Netti, P. A. Synthesis of semicrystalline nanocapsular structures obtained by Thermally Induced Phase Separation in nanoconfinement. *Sci. Rep.* **2016**, 6, 32727.

117. Crespy, D.; Stark, M.; Hoffmann-Richter, C.; Ziener, U.; Landfester, K. Polymeric Nanoreactors for Hydrophilic Reagents Synthesized by Interfacial Polycondensation on Miniemulsion Droplets. *Macromolecules* **2007**, 40, 3122-3135.

118. Jagielski, N.; Sharma, S.; Hombach, V.; Mailänder, V.; Rasche, V.; Landfester, K. Nanocapsules Synthesized by Miniemulsion Technique for Application as New Contrast

Agent Materials. *Macromol. Chem. Phys.* **2007**, 208, 2229-2241.

119. Wang, W.; Qi, H.; Zhou, T.; Mei, S.; Han, L.; Higuchi, T.; Jinnai, H.; Li, C. Y. Highly robust crystalsome via directed polymer crystallization at curved liquid/liquid interface. *Nat. Commun.* **2016**, 7, 10599.

120. Zhao, Y.; Landfester, K.; Crespy, D. CO 2 responsive reversible aggregation of nanoparticles and formation of nanocapsules with an aqueous core. *Soft Matter* **2012**, 8, 11687-11696.

121. Fickert, J.; Wohnhaas, C.; Turshatov, A.; Landfester, K.; Crespy, D. Copolymers Structures Tailored for the Preparation of Nanocapsules. *Macromolecules* **2013**, 46, 573-579.

122. Staff, R. H.; Gallei, M.; Landfester, K.; Crespy, D. Hydrophobic Nanocontainers for Stimulus-Selective Release in Aqueous Environments. *Macromolecules* **2014**, 47, 4876-4883.

123. Bauer, K. N.; Tee, H. T.; Lieberwirth, I.; Wurm, F. R. In-Chain Poly(phosphonate)s via Acyclic Diene Metathesis Polycondensation. *Macromolecules* **2016**, 49, 3761-3768.

124. Scherrer, P. Bestimmung der inneren Struktur und der Größe von Kolloidteilchen mittels Röntgenstrahlen. In *Kolloidchemie Ein Lehrbuch*, Springer Berlin Heidelberg: 1912; pp 387-409.

125. Murase, S. K.; Franco, L.; del Valle, L. J.; Puiggalí, J. Synthesis and characterization of poly(ester amides)s with a variable ratio of branched odd diamide units. *J. Appl. Polym. Sci.* **2014**, 131, 40102.

126. Yadav, S. K.; Ron, N.; Chandrasekharam, D.; Khilar, K. C.; Suresh, A. K.; Nadkarni, V. M. Polyureas by interfacial polycondensation: Preparation and properties. *J. Macromol. Sci., B* **1996**, 35, 807-827.

127. PDF-2 database, ICDD card no. #00-005-0628 for cubic NaCl.

128. Mishima, S.; Kaneoka, H.; Nakagawa, T. Characterization and pervaporation of chlorinated hydrocarbon–water mixtures with fluoroalkyl methacrylate-grafted PDMS membrane. *J. Appl. Polym. Sci.* **1999**, 71, 273-287.

129. Zheng, Y.-R.; Tee, H. T.; Wei, Y.; Wu, X.-L.; Mezger, M.; Yan, S.; Landfester, K.; Wagener, K.; Wurm, F. R.; Lieberwirth, I. Morphology and Thermal Properties of Precision Polymers: The Crystallization of Butyl Branched Polyethylene and Polyphosphoesters. *Macromolecules* **2016**, 49, 1321-1330.

130. Ferrari, M. Cancer nanotechnology: opportunities and challenges. *Nat. Rev. Cancer* **2005**, 5, 161-171.

131. Dhanasekaran, S. M.; Barrette, T. R.; Ghosh, D.; Shah, R.; Varambally, S.; Kurachi, K.; Pienta, K. J.; Rubin, M. A.; Chinnaiyan, A. M. Delineation of prognostic biomarkers in prostate cancer. *Nature* **2001**, 412, 822-826.

132. Weissleder, R.; Tung, C.-H.; Mahmood, U.; Bogdanov, A. In vivo imaging of tumors with protease-activated near-infrared fluorescent probes. *Nat. Biotechnol.* **1999**, 17, 375-378.

133. Hingorani, S. R.; Petricoin Iii, E. F.; Maitra, A.; Rajapakse, V.; King, C.; Jacobetz, M. A.; Ross, S.; Conrads, T. P.; Veenstra, T. D.; Hitt, B. A.; Kawaguchi, Y.; Johann, D.; Liotta, L. A.; Crawford, H. C.; Putt, M. E.; Jacks, T.; Wright, C. V. E.; Hruban, R. H.; Lowy, A. M.; Tuveson, D. A. Preinvasive and invasive ductal pancreatic cancer and its early detection in the mouse. *Cancer Cell* **2003**, 4, 437-450.

134. Matson, M. L.; Wilson, L. J. Nanotechnology and MRI contrast enhancement. *Future Med. Chem.* **2010**, 2, 491-502.

135. Lee, J.-H.; Huh, Y.-M.; Jun, Y.-w.; Seo, J.-w.; Jang, J.-t.; Song, H.-T.; Kim, S.; Cho, E.-J.; Yoon, H.-G.; Suh, J.-S.; Cheon, J. Artificially engineered magnetic nanoparticles for ultra-sensitive molecular imaging. *Nat. Med.* **2007**, 13, 95-99.

136. Werner, E. J.; Datta, A.; Jocher, C. J.; Raymond, K. N. High-Relaxivity MRI Contrast

Agents: Where Coordination Chemistry Meets Medical Imaging. *Angew. Chem. Int. Ed.* **2008**, 47, 8568-8580.
137. Angelovski, G. What We Can Really Do with Bioresponsive MRI Contrast Agents. *Angew. Chem. Int. Ed.* **2016**, 55, 7038-7046.
138. Gao, Z.; Ma, T.; Zhao, E.; Docter, D.; Yang, W.; Stauber, R. H.; Gao, M. Small is Smarter: Nano MRI Contrast Agents – Advantages and Recent Achievements. *Small* **2016**, 12, 556-576.
139. Aime, S.; Botta, M.; Fasano, M.; Terreno, E. Prototropic and Water-Exchange Processes in Aqueous Solutions of Gd(III) Chelates. *Acc. Chem. Res.* **1999**, 32, 941-949.
140. Bottrill, M.; Kwok, L.; Long, N. J. Lanthanides in magnetic resonance imaging. *Chem. Soc. Rev.* **2006**, 35, 557-571.
141. Bridot, J.-L.; Faure, A.-C.; Laurent, S.; Rivière, C.; Billotey, C.; Hiba, B.; Janier, M.; Josserand, V.; Coll, J.-L.; Vander Elst, L.; Muller, R.; Roux, S.; Perriat, P.; Tillement, O. Hybrid Gadolinium Oxide Nanoparticles: Multimodal Contrast Agents for in Vivo Imaging. *J. Am. Chem. Soc.* **2007**, 129, 5076-5084.
142. Ahrén, M.; Selegård, L.; Klasson, A.; Söderlind, F.; Abrikossova, N.; Skoglund, C.; Bengtsson, T.; Engström, M.; Käll, P.-O.; Uvdal, K. Synthesis and Characterization of PEGylated Gd2O3 Nanoparticles for MRI Contrast Enhancement. *Langmuir* **2010**, 26, 5753-5762.
143. Tian, G.; Gu, Z.; Liu, X.; Zhou, L.; Yin, W.; Yan, L.; Jin, S.; Ren, W.; Xing, G.; Li, S.; Zhao, Y. Facile Fabrication of Rare-Earth-Doped Gd2O3 Hollow Spheres with Upconversion Luminescence, Magnetic Resonance, and Drug Delivery Properties. *J. Phys. Chem. C* **2011**, 115, 23790-23796.
144. Alric, C.; Taleb, J.; Duc, G. L.; Mandon, C.; Billotey, C.; Meur-Herland, A. L.; Brochard, T.; Vocanson, F.; Janier, M.; Perriat, P.; Roux, S.; Tillement, O. Gadolinium Chelate Coated Gold Nanoparticles As Contrast Agents for Both X-ray Computed Tomography and Magnetic Resonance Imaging. *J. Am. Chem. Soc.* **2008**, 130, 5908-5915.
145. Song, Y.; Xu, X.; MacRenaris, K. W.; Zhang, X.-Q.; Mirkin, C. A.; Meade, T. J. Multimodal Gadolinium-Enriched DNA–Gold Nanoparticle Conjugates for Cellular Imaging. *Angew. Chem. Int. Ed.* **2009**, 48, 9143-9147.
146. Taylor, K. M. L.; Jin, A.; Lin, W. Surfactant-Assisted Synthesis of Nanoscale Gadolinium Metal–Organic Frameworks for Potential Multimodal Imaging. *Angew. Chem. Int. Ed.* **2008**, 47, 7722-7725.
147. Anderson, E. A.; Isaacman, S.; Peabody, D. S.; Wang, E. Y.; Canary, J. W.; Kirshenbaum, K. Viral Nanoparticles Donning a Paramagnetic Coat: Conjugation of MRI Contrast Agents to the MS2 Capsid. *Nano Lett.* **2006**, 6, 1160-1164.
148. Wiener, E.; Brechbiel, M. W.; Brothers, H.; Magin, R. L.; Gansow, O. A.; Tomalia, D. A.; Lauterbur, P. C. Dendrimer-based metal chelates: A new class of magnetic resonance imaging contrast agents. *Magn. Reson. Med.* **1994**, 31, 1-8.
149. Rowe, M. D.; Thamm, D. H.; Kraft, S. L.; Boyes, S. G. Polymer-Modified Gadolinium Metal-Organic Framework Nanoparticles Used as Multifunctional Nanomedicines for the Targeted Imaging and Treatment of Cancer. *Biomacromolecules* **2009**, 10, 983-993.
150. Cheng, Z.; Thorek, D. L. J.; Tsourkas, A. Gadolinium-Conjugated Dendrimer Nanoclusters as a Tumor-Targeted T1 Magnetic Resonance Imaging Contrast Agent. *Angew. Chem. Int. Ed.* **2010**, 49, 346-350.
151. Olson, E. S.; Jiang, T.; Aguilera, T. A.; Nguyen, Q. T.; Ellies, L. G.; Scadeng, M.; Tsien, R. Y. Activatable cell penetrating peptides linked to nanoparticles as dual probes for in vivo fluorescence and MR imaging of proteases. *Proc. Natl. Acad. Sci. U.S.A.* **2010**, 107, 4311-4316.
152. Mikawa, M.; Kato, H.; Okumura, M.; Narazaki, M.; Kanazawa, Y.; Miwa, N.; Shinohara, H. Paramagnetic Water-Soluble Metallofullerenes Having the Highest Relaxivity

for MRI Contrast Agents. *Bioconj. Chem.* **2001**, 12, 510-514.

153. Tóth, É.; Bolskar, R. D.; Borel, A.; González, G.; Helm, L.; Merbach, A. E.; Sitharaman, B.; Wilson, L. J. Water-Soluble Gadofullerenes: Toward High-Relaxivity, pH-Responsive MRI Contrast Agents. *J. Am. Chem. Soc.* **2004**, 127, 799-805.

154. Zairov, R.; Mustafina, A.; Shamsutdinova, N.; Nizameev, I.; Moreira, B.; Sudakova, S.; Podyachev, S.; Fattakhova, A.; Safina, G.; Lundstrom, I.; Gubaidullin, A.; Vomiero, A. High performance magneto-fluorescent nanoparticles assembled from terbium and gadolinium 1,3-diketones. *Sci. Rep.* **2017**, 7, 40486.

155. Mulder, W. J. M.; Strijkers, G. J.; van Tilborg, G. A. F.; Griffioen, A. W.; Nicolay, K. Lipid-based nanoparticles for contrast-enhanced MRI and molecular imaging. *NMR Biomed.* **2006**, 19, 142-164.

156. Rieter, W. J.; Kim, J. S.; Taylor, K. M. L.; An, H.; Lin, W.; Tarrant, T.; Lin, W. Hybrid Silica Nanoparticles for Multimodal Imaging. *Angew. Chem. Int. Ed.* **2007**, 46, 3680-3682.

157. Hsiao, J.-K.; Tsai, C.-P.; Chung, T.-H.; Hung, Y.; Yao, M.; Liu, H.-M.; Mou, C.-Y.; Yang, C.-S.; Chen, Y.-C.; Huang, D.-M. Mesoporous Silica Nanoparticles as a Delivery System of Gadolinium for Effective Human Stem Cell Tracking. *Small* **2008**, 4, 1445-1452.

158. Reynolds, C. H.; Annan, N.; Beshah, K.; Huber, J. H.; Shaber, S. H.; Lenkinski, R. E.; Wortman, J. A. Gadolinium-Loaded Nanoparticles: New Contrast Agents for Magnetic Resonance Imaging. *J. Am. Chem. Soc.* **2000**, 122, 8940-8945.

159. Doiron, A. L.; Homan, K. A.; Emelianov, S.; Brannon-Peppas, L. Poly(Lactic-co-Glycolic) Acid as a Carrier for Imaging Contrast Agents. *Pharm. Res.* **2009**, 26, 674-682.

160. Perez-Baena, I.; Loinaz, I.; Padro, D.; Garcia, I.; Grande, H. J.; Odriozola, I. Single-chain polyacrylic nanoparticles with multiple Gd(iii) centres as potential MRI contrast agents. *J. Mater. Chem.* **2010**, 20, 6916-6922.

161. Koffie, R. M.; Farrar, C. T.; Saidi, L.-J.; William, C. M.; Hyman, B. T.; Spires-Jones, T. L. Nanoparticles enhance brain delivery of blood–brain barrier-impermeable probes for in vivo optical and magnetic resonance imaging. *Proc. Natl. Acad. Sci. U.S.A.* **2011**, 108, 18837-18842.

162. Hu, X.; Liu, G.; Li, Y.; Wang, X.; Liu, S. Cell-Penetrating Hyperbranched Polyprodrug Amphiphiles for Synergistic Reductive Milieu-Triggered Drug Release and Enhanced Magnetic Resonance Signals. *J. Am. Chem. Soc.* **2015**, 137, 362-368.

163. Sharma, S.; Paiphansiri, U.; Hombach, V.; Mailander, V.; Zimmermann, O.; Landfester, K.; Rasche, V. Characterization of MRI contrast agent-loaded polymeric nanocapsules as versatile vehicle for targeted imaging. *Contrast Media Mol. Imaging* **2010**, 5, 59-69.

164. Winzen, S.; Schoettler, S.; Baier, G.; Rosenauer, C.; Mailaender, V.; Landfester, K.; Mohr, K. Complementary analysis of the hard and soft protein corona: sample preparation critically effects corona composition. *Nanoscale* **2015**, 7, 2992-3001.

165. Schöttler, S.; Becker, G.; Winzen, S.; Steinbach, T.; Mohr, K.; Landfester, K.; Mailänder, V.; Wurm, F. R. Protein adsorption is required for stealth effect of poly(ethylene glycol)- and poly(phosphoester)-coated nanocarriers. *Nat. Nanotech.* **2016**, 11, 372-377.

166. Jiang, Y.; Jahagirdar, B. N.; Reinhardt, R. L.; Schwartz, R. E.; Keene, C. D.; Ortiz-Gonzalez, X. R.; Reyes, M.; Lenvik, T.; Lund, T.; Blackstad, M.; Du, J.; Aldrich, S.; Lisberg, A.; Low, W. C.; Largaespada, D. A.; Verfaillie, C. M. Pluripotency of mesenchymal stem cells derived from adult marrow. *Nature* **2002**, 418, 41-49.

167. Banchereau, J.; Steinman, R. M. Dendritic cells and the control of immunity. *Nature* **1998**, 392, 245-252.

168. Hackstein, H.; Thomson, A. W. Dendritic cells: emerging pharmacological targets of immunosuppressive drugs. *Nat. Rev. Immunol.* **2004**, 4, 24-35.

169. Han, H.; Li, S.; Zhu, X.; Jiang, X.; Kong, X. Z. One step preparation of porous polyurea by reaction of toluene diisocyanate with water and its characterization. *RSC Advances* **2014**,

4, 33520-33529.

170. Jadhav, K. T.; Babu, P. V. V. Effect of various parameters on formation of polyurea microcapsules by interfacial polycondensation techniques. *IJSER* **2013**, 4, 1084-1090.

171. Mandelkern, L. Crystallization Kinetics in High Polymers. II. Polymer-Diluent Mixtures. *J. Appl. Phys.* **1955**, 26, 443-451.

172. Paul, D. R.; Barlow, J. W. Crystallization from Miscible Polymer Blends. In *Polymer Alloys II: Blends, Blocks, Grafts, and Interpenetrating Networks*, Klempner, D.; Frisch, K. C., Eds. Springer US: Boston, MA, 1980; pp 239-253.

173. Boon, J.; Azcue, J. M. Crystallization kinetics of polymer–diluent mixtures. Influence of benzophenone on the spherulitic growth rate of isotactic polystyrene. *Journal of Polymer Science Part A-2: Polymer Physics* **1968**, 6, 885-894.

174. Zhang, W.; Peters, J. A.; Mayer, F.; Helm, L.; Djanashvili, K. Prototropic Exchange Governs T1 and T2 Relaxivities of a Potential MRI Contrast Agent Nanozeolite Gd−LTL with a High pH Responsiveness. *J. Phys. Chem. C* **2015**, 119, 5080-5089.

175. Muller, L. K.; Simon, J.; Schottler, S.; Landfester, K.; Mailander, V.; Mohr, K. Pre-coating with protein fractions inhibits nano-carrier aggregation in human blood plasma. *RSC Advances* **2016**, 6, 96495-96509.

176. Schottler, S.; Klein, K.; Landfester, K.; Mailander, V. Protein source and choice of anticoagulant decisively affect nanoparticle protein corona and cellular uptake. *Nanoscale* **2016**, 8, 5526-5536.

177. Ogawara, K.-i.; Furumoto, K.; Nagayama, S.; Minato, K.; Higaki, K.; Kai, T.; Kimura, T. Pre-coating with serum albumin reduces receptor-mediated hepatic disposition of polystyrene nanosphere: implications for rational design of nanoparticles. *J. Control. Release* **2004**, 100, 451-455.

178. Mori, K.; Emoto, M.; Inaba, M. Fetuin-A: A Multifunctional Protein. *Recent Pat. Endocr. Metab. Immune Drug Discov.* **2011**, 5, 124-146.

179. Shilo, M.; Reuveni, T.; Motiei, M.; Popovtzer, R. Nanoparticles as computed tomography contrast agents: current status and future perspectives. *Nanomedicine* **2012**, 7, 257-269.

180. Yeh, B. M.; FitzGerald, P. F.; Edic, P. M.; Lambert, J. W.; Colborn, R. E.; Marino, M. E.; Evans, P. M.; Roberts, J. C.; Wang, Z. J.; Wong, M. J.; Bonitatibus Jr, P. J. Opportunities for new CT contrast agents to maximize the diagnostic potential of emerging spectral CT technologies. *Adv. Drug Del. Rev.* **2016**.

181. He, W.; Ai, K.; Lu, L. Nanoparticulate X-ray CT contrast agents. *Sci. China Chem.* **2015**, 58, 753.

182. Annapragada, A. Advances in nanoparticle imaging technology for vascular pathologies. *Annu. Rev. Med.* **2015**, 66, 177-193.

183. Attia, M. F.; Anton, N.; Chiper, M.; Akasov, R.; Anton, H.; Messaddeq, N.; Fournel, S.; Klymchenko, A. S.; Mély, Y.; Vandamme, T. F. Biodistribution of X-Ray Iodinated Contrast Agent in Nano-Emulsions Is Controlled by the Chemical Nature of the Oily Core. *ACS Nano* **2014**, 8, 10537-10550.

184. Torchilin, V. P.; Frank-Kamenetsky, M. D.; Wolf, G. L. CT visualization of blood pool in rats by using long-circulating, iodine-containing micelles. *Acad. Radiol.* **1999**, 6, 61-65.

185. de Vries, A.; Custers, E.; Lub, J.; van den Bosch, S.; Nicolay, K.; Grüll, H. Block-copolymer-stabilized iodinated emulsions for use as CT contrast agents. *Biomaterials* **2010**, 31, 6537-6544.

186. Zou, Y.; Wei, Y.; Wang, G.; Meng, F.; Gao, M.; Storm, G.; Zhong, Z. Nanopolymersomes with an Ultrahigh Iodine Content for High-Performance X-Ray Computed Tomography Imaging In Vivo. *Adv. Mater.* **2017**.

187. Fu, Y.; Nitecki, D. E.; Maltby, D.; Simon, G. H.; Berejnoi, K.; Raatschen, H.-J.; Yeh, B. M.; Shames, D. M.; Brasch, R. C. Dendritic Iodinated Contrast Agents with PEG-Cores for CT

Imaging: Synthesis and Preliminary Characterization. *Bioconj. Chem.* **2006**, 17, 1043-1056.

188. You, S.; Jung, H.-y.; Lee, C.; Choe, Y. H.; Heo, J. Y.; Gang, G.-T.; Byun, S.-K.; Kim, W. K.; Lee, C.-H.; Kim, D.-E.; Kim, Y. I.; Kim, Y. High-performance dendritic contrast agents for X-ray computed tomography imaging using potent tetraiodobenzene derivatives. *J. Control. Release* **2016**, 226, 258-267.

189. Pan, D.; Williams, T. A.; Senpan, A.; Stacy, A. J.; Scott, M. J.; Gaffney, P. J.; Wickline, S. A.; Lanza, G. M. Detecting Vascular Bio-signatures with a Colloidal, Radio-opaque Polymeric Nanoparticle. *J. Am. Chem. Soc.* **2009**, 131, 15522-15527.

190. Kong, W. H.; Lee, W. J.; Cui, Z. Y.; Bae, K. H.; Park, T. G.; Kim, J. H.; Park, K.; Seo, S. W. Nanoparticulate carrier containing water-insoluble iodinated oil as a multifunctional contrast agent for computed tomography imaging. *Biomaterials* **2007**, 28, 5555-5561.

191. deKrafft, K. E.; Xie, Z.; Cao, G.; Tran, S.; Ma, L.; Zhou, O. Z.; Lin, W. Iodinated Nanoscale Coordination Polymers as Potential Contrast Agents for Computed Tomography. *Angew. Chem. Int. Ed.* **2009**, 48, 9901-9904.

192. Yin, Q.; Yap, F. Y.; Yin, L.; Ma, L.; Zhou, Q.; Dobrucki, L. W.; Fan, T. M.; Gaba, R. C.; Cheng, J. Poly(iohexol) Nanoparticles As Contrast Agents for In Vivo X-ray Computed Tomography Imaging. *J. Am. Chem. Soc.* **2013**, 135, 13620-13623.

193. Hyafil, F.; Cornily, J.-C.; Feig, J. E.; Gordon, R.; Vucic, E.; Amirbekian, V.; Fisher, E. A.; Fuster, V.; Feldman, L. J.; Fayad, Z. A. Noninvasive detection of macrophages using a nanoparticulate contrast agent for computed tomography. *Nat. Med.* **2007**, 13, 636-641.

194. Kao, C.-Y.; Hoffman, E. A.; Beck, K. C.; Bellamkonda, R. V.; Annapragada, A. V. Long-Residence-Time Nano-Scale Liposomal Iohexol for X-ray–Based Blood Pool Imaging. *Acad. Radiol.* **2003**, 10, 475-483.

195. Leander, P.; Höglund, P.; Børseth, A.; Kloster, Y.; Berg, A. A new liposomal liver-specific contrast agent for CT: first human phase-I clinical trial assessing efficacy and safety. *Eur. Radiol.* **2001**, 11, 698-704.

196. nanoPET Pharma GmbH 2016. ExiTron nano. https://www.viscover-online.de/?ActionCall=WebActionDownloadDocument&Params[itemId]=147&Params[documentId]=91 (accessed June 16, 2017).

197. MediLumine Inc. http://www.medilumine.com/wp-content/uploads/2016/07/CofA-V15X05.pdf (accessed 16 June, 2017).

198. Bayer Inc. 2012. ULTRAVIST Product Monograph. https://www.radiologysolutions.bayer.ca/static/media/PDFs/21012015/Ultravist%20PM%20Nov%2028%202014.pdf (accessed June 09, 2017).

199. Delebecq, E.; Pascault, J.-P.; Boutevin, B.; Ganachaud, F. On the Versatility of Urethane/Urea Bonds: Reversibility, Blocked Isocyanate, and Non-isocyanate Polyurethane. *Chem. Rev.* **2013**, 113, 80-118.

200. Wright, P.; Cumming, A. P. C. *Solid Polyurethane Elastomers*. Maclaren: 1969.

201. Hepburn, C. Reaction Rates, Catalysis and Surfactants. In *Polyurethane Elastomers*, Springer Netherlands: Dordrecht, 1992; pp 107-121.

202. Britain, J.; Gemeinhardt, P. Catalysis of the isocyanate-hydroxyl reaction. *J. Appl. Polym. Sci.* **1960**, 4, 207-211.

203. Schellekens, Y.; Van Trimpont, B.; Goelen, P.-J.; Binnemans, K.; Smet, M.; Persoons, M.-A.; De Vos, D. Tin-free catalysts for the production of aliphatic thermoplastic polyurethanes. *Green Chem.* **2014**, 16, 4401-4407.

204. Keith, L. H.; Walters, D. B. *National Toxicology Program's Chemical Solubility Compendium*. Taylor & Francis: 1991.

205. Landfester, K. Polyreactions in Miniemulsions. *Macromol. Rapid Commun.* **2001**, 22, 896-936.

206. CRC handbook of chemistry and physics. Haynes, William M.: **2007**.

207. Nazarzadeh, E.; Sajjadi, S. Viscosity effects in miniemulsification via ultrasound.

AIChE J. **2010**, 56, 2751-2755.

208. Behzadi, S.; Rosenauer, C.; Kappl, M.; Mohr, K.; Landfester, K.; Crespy, D. Osmotic pressure-dependent release profiles of payloads from nanocontainers by co-encapsulation of simple salts. *Nanoscale* **2016**, 8, 12998-13005.

209. Mosesson, M. W.; Siebenlist, K. R.; Meh, D. A. The Structure and Biological Features of Fibrinogen and Fibrin. *Ann. N.Y. Acad. Sci.* **2001**, 936, 11-30.

210. Mohr, K.; Sommer, M.; Baier, G.; Schöttler, S.; Okwieka, P.; Tenzer, S.; Landfester, K.; Mailänder, V.; Schmidt, M.; Meyer, R. G. Aggregation behavior of polystyrene-nanoparticles in human blood serum and its impact on the in vivo distribution in mice. *J. Nanomed. Nanotechnol.* **2014**, 5.

211. Kratz, F. Albumin as a drug carrier: Design of prodrugs, drug conjugates and nanoparticles. *J. Control. Release* **2008**, 132, 171-183.

212. Peters, T. Serum Albumin. *Adv. Protein Chem.* **1985**, 37, 161-245.

213. Lunov, O.; Syrovets, T.; Loos, C.; Beil, J.; Delacher, M.; Tron, K.; Nienhaus, G. U.; Musyanovych, A.; Mailänder, V.; Landfester, K.; Simmet, T. Differential Uptake of Functionalized Polystyrene Nanoparticles by Human Macrophages and a Monocytic Cell Line. *ACS Nano* **2011**, 5, 1657-1669.

214. Wang, T.; Niu, G.; Kortylewski, M.; Burdelya, L.; Shain, K.; Zhang, S.; Bhattacharya, R.; Gabrilovich, D.; Heller, R.; Coppola, D.; Dalton, W.; Jove, R.; Pardoll, D.; Yu, H. Regulation of the innate and adaptive immune responses by Stat-3 signaling in tumor cells. *Nat. Med.* **2004**, 10, 48-54.

215. Furtek, S. L.; Backos, D. S.; Matheson, C. J.; Reigan, P. Strategies and Approaches of Targeting STAT3 for Cancer Treatment. *ACS Chem. Biol.* **2016**, 11, 308-318.

216. Baier, G.; Baumann, D.; Siebert, J. M.; Musyanovych, A.; Mailänder, V.; Landfester, K. Suppressing Unspecific Cell Uptake for Targeted Delivery Using Hydroxyethyl Starch Nanocapsules. *Biomacromolecules* **2012**, 13, 2704-2715.

217. Ye, L.; Zhang, Y.; Yang, B.; Zhou, X.; Li, J.; Qin, Z.; Dong, D.; Cui, Y.; Yao, F. Zwitterionic-Modified Starch-Based Stealth Micelles for Prolonging Circulation Time and Reducing Macrophage Response. *ACS Appl. Mater. Interfaces* **2016**, 8, 4385-4398.

218. Besheer, A.; Hause, G.; Kressler, J.; Mäder, K. Hydrophobically Modified Hydroxyethyl Starch: Synthesis, Characterization, and Aqueous Self-Assembly into Nano-Sized Polymeric Micelles and Vesicles. *Biomacromolecules* **2007**, 8, 359-367.

219. Yue, P.; Turkson, J. Targeting STAT3 in cancer: how successful are we? *Expert Opin. Investig. Drugs* **2009**, 18, 45-56.

220. Cayman Chemical Company. Safety Data Sheet S3I-201 https://www.caymanchem.com/msdss/14336m.pdf (accessed July 20,2017).

221. Gutteridge, W. E.; Hudson, A. T.; Latter, V. S. (The Welcome Foundation Limited). Naphthoquinones for the treatment and prophylaxis of pneumocystis carinii infections. EP0362996 (A2), Apr. 15, 1992.

222. Hudson, A. T. (The Welcome Foundation Limited). Medicaments for the treatment of toxoplasmosis. EP0567162 (A1), Oct. 27, 1993.

223. Kambhampati, S.; Thanigaimalai, N.; Taduri, V. B.; Chitturi, T. R.; Thennati, R. (Sun Pharmaceutical Industries Limited). Cyclodextrin complexes of atovaquone. WO 2009/007996 (A2), Jan. 15, 2009.

224. Baggish, A. L.; Hill, D. R. Antiparasitic Agent Atovaquone. *Antimicrob. Agents Chemother.* **2002**, 46, 1163-1173.

225. Xiang, M. Physiological and Pharmacological Regulation of the STAT3 Pathway in Cancer. 2013.

226. Xiang, M.; Kim, H.; Ho, V. T.; Walker, S. R.; Bar-Natan, M.; Liu, S.; Toniolo, P. A.; Kroll, Y.; Jones, N.; Giaccone, Z. T. Gene expression–based discovery of atovaquone as a STAT3 inhibitor and anticancer agent. *Blood* **2016**, 128, 1845-1853.

227. Navale, S.; Das, S.; Singh, G.; Mathur, R. S. Pharmaceutical composition comprising atovaquone particles. US 2008/0241254 (A1), Oct. 2, 2008.
228. Mooney, B. A.; Keramidas, P. (Alphapharm Pty. Ltd.). Atovaquone with a particle size diameter range (d90) of greater than 3 microns to about 10 microns. US 2011/0206770 (A1), Aug. 25, 2011.
229. Dearn, A. R. (Glaxo Wellcome Inc., Research Triangle Park, N.C.). Atovaquone pharmaceutical compositions. US 006018080 (A), Jan. 25, 2000.
230. Shubar, H. M.; Dunay, I. R.; Lachenmaier, S.; Dathe, M.; Bushrab, F. N.; Mauludin, R.; Müller, R. H.; Fitzner, R.; Borner, K.; Liesenfeld, O. The role of apolipoprotein E in uptake of atovaquone into the brain in murine acute and reactivated toxoplasmosis. *J. Drug Targeting* **2009**, 17, 257-267.
231. Soleimani, A. H.; Garg, S. M.; Paiva, I. M.; Vakili, M. R.; Alshareef, A.; Huang, Y.-H.; Molavi, O.; Lai, R.; Lavasanifar, A. Micellar nano-carriers for the delivery of STAT3 dimerization inhibitors to melanoma. *Drug Deliv. Transl. Res.* **2017**, 1-11.
232. Noga, M.; Edinger, D.; Rödl, W.; Wagner, E.; Winter, G.; Besheer, A. Controlled shielding and deshielding of gene delivery polyplexes using hydroxyethyl starch (HES) and alpha-amylase. *J. Control. Release* **2012**, 159, 92-103.
233. Petersen, S. Niedermolekulare Umsetzungsprodukte aliphatischer Diisocyanate 5. Mitteilung über Polyurethane). *Justus Liebigs Ann. Chem.* **1949**, 562, 205-228.
234. Dyer, E.; Glenn, J. F.; Lendrat, E. G. The Kinetics of the Reactions of Phenyl Isocyanate with Thiols. *J. Org. Chem.* **1961**, 26, 2919-2925.
235. Arnold, R.; Nelson, J.; Verbanc, J. Recent advances in isocyanate chemistry. *Chem. Rev.* **1957**, 57, 47-76.
236. Schlaad, H.; Kukula, H.; Rudloff, J.; Below, I. Synthesis of α,ω-Heterobifunctional Poly(ethylene glycol)s by Metal-Free Anionic Ring-Opening Polymerization. *Macromolecules* **2001**, 34, 4302-4304.
237. GraphPad Software Inc. QuickCalcs *t* test calculator. http://www.graphpad.com/quickcalcs/ttest1/?Format=SD (accessed August 08, 2017).
238. Greely, H. T.; Cho, M. K. The Henrietta Lacks legacy grows. *EMBO reports* **2013**, 14, 849-849.
239. Houen, G. The solubility of proteins in organic solvents. *Acta Chem. Scand.* **1996**, 50, 68-70.
240. sigma-aldrich.com. Albumin from human serum - Product Information. http://www.sigmaaldrich.com/content/dam/sigmaaldrich/docs/Sigma/Product_Information_Sheet/a9511pis.pdf (accessed August 04, 2017).
241. Santa Cruz Biotechnology Inc. Tolylene-2,4-diisocyanate (CAS 584-84-9) https://www.scbt.com/scbt/product/tolylene-2-4-diisocyanate-584-84-9 (accessed August 04, 2017).
242. Gaylord Chemical Company, L. L. C. Dimethyl sulfoxide solubility data. http://www.gaylordchemical.com/wp-content/uploads/2015/07/GC-Literature-102B-ENG-Low.pdf (accessed July 24, 2017).
243. Schwetlick, K. *Organikum*. Wiley: Dresden, 2001; Vol. 21.
244. Frick, S. U.; Domogalla, M. P.; Baier, G.; Wurm, F. R.; Mailänder, V.; Landfester, K.; Steinbrink, K. Interleukin-2 Functionalized Nanocapsules for T Cell-Based Immunotherapy. *ACS Nano* **2016**, 10, 9216-9226.

Appendix

Acknowledgments

Curriculum Vitae

Scientific Contributions

Publications

Schlegel, I.; Muñoz-Espí, R.; Renz, P.; Lieberwirth, I.; Floudas, G.; Suzuki, Y.; Crespy, D.; Landfester, K. Crystallinity Tunes Permeability of Polymer Nanocapsules. *Macromolecules* **2017**, 50, 4725-4732.

Malzahn, K.; Ebert, S.; **Schlegel, I.**; Neudert, O.; Wagner, M.; Schütz, G.; Ide, A.; Roohi, F.; Münnemann, K.; Crespy, D.; Landfester, K. Design and Control of Nanoconfinement to Achieve Magnetic Resonance Contrast Agents with High Relaxivity. *Advanced Healthcare Materials* **2016**, 5, 567-574.

Conference contributions

I. Schlegel, M. Domogalla, K. Steinbrink, R. Muñoz-Espí, D. Crespy, K. Landfester; Accessibility to Nanocapsule Loadings, international symposium "CHEMICAL DESIGN – bioMEDICAL APPLICATIONS" held by the Collaborative Research Center CRC 1066 "Nanodimensional polymeric therapeutics for tumor immunotherapy", September 15–16, 2016, Mainz–Germany [Poster]. **Awarded with a 1st place poster prize sponsored by Wiley VCH.**

I. Schlegel, K. Malzahn, S. Ebert, K. Münnemann, R. Muñoz-Espí, D. Crespy, K. Landfester; Hocheffiziente MRT-Kontrastmittel durch Nanoverkapselung, CI3 Schaufenster, May 21, 2015, Mainz–Germany [Poster].

I. Schlegel, K. Malzahn, S. Ebert, K. Münnemann, R. Muñoz-Espí, D. Crespy, K. Landfester; Hocheffiziente MRT-Kontrastmittel durch Nanoverkapselung, 128. GDNÄ-Versammlung, Johannes Gutenberg-Universität Mainz, September 12–15, 2014, Mainz–Germany [Poster].